Controlling Hypersonic Particle Resonances through Tailored Colloidal Synthesis

Dissertation

zur Erlangung des Grades

„Doktor der Naturwissenschaften"

(Dr. rer. Nat)

im Promotionsfach Chemie

am Fachberiech Chemie, Pharmazie,

Geographie, und Geowissenschaften

der Johannes Gutenberg-Universität Mainz

vorgelegt von

Eunsoo Kang

geb. in Seoul,

Mainz, 2020

1. Berichterstatter : Prof. Dr. ██████████████

2. Berichterstatter : Prof. Dr. ████████████

3. Berichterstatter : Prof. Dr. ██████████████

4. Berichterstatter : Prof. Dr. ████████████████████████████

5. Berichterstatter : Prof. Dr. ████████████████████████

Tag der mündlichen Prüfung : 25. Mai. 2020

Die vorliegende Arbeit wurde im Zeitraum von April 2017 bis März 2020 am Max-Planck-Institut für Polymerforschung in Mainz unter der Anleitung von Herrn Prof. ███████████,
Herrn Prof. ███████, und Herrn Prof. ██████████ angefertigt.

IV

Copyrights and Author Contributions

1. Direct observation of polymer surface mobility via nanoparticle vibrations

- **Chapter 6.1**, published in *Nature Communications*, **2018**, 9, 2918.

Eunsoo Kang, I, as the 3rd author, synthesized polystyrene particles (PS_B-190, PS_B-202, PS_X-257), fabricated closed-packed structure samples for BLS. The vibrational modes of samples from BLS (including temperature dependent test) were collected and analyzed by me. I was also involved in writing the manuscript. I appreciate all co-work from authors who are involved in this work.

2. Ultrathin Shell Layers Dramatically Influence Polymer Nanoparticle Surface Mobility

- **Chapter 6.2**, published in *Macromolecules*, **2018**, 51, 21, 8522. Further permissions related to the material excerpted should be directed to the ACS.

Eunsoo Kang, I, designed the research as the 1st author. I synthesized core particles (PS_A), and core-shell structure particles (PS_A, PS_A-PS, PS_A-PMMA). The experimental data of all samples (PS_A, PS_A-PS, PS_A-PMMA, PS_B, PS_B@PDADMAC, PS_B@PDADMAC@PSS) were collected and analyzed by me. I wrote and reviewed the manuscript. I appreciate all co-work from authors who are involved in this work.

3. Shell Architecture Strongly Influences the Glass Transition, Surface Mobility, and Elasticity of Polymer Core-Shell Nanoparticles

- **Chapter 6.3**, published in *Macromolecules*, **2019**, 52, 14, 5399. Further permissions related to the material excerpted should be directed to the ACS.

Eunsoo Kang, I, designed the research as the 1st author. I synthesized particles with core-shell structure with different shell composition and thickness (PS-PS, PS-$PBMA_7$, PS-$PBMA_{34}$, PS-$PBMA_{58}$, PS-$PMMA_8$, PS-$PMMA_{16}$). I collected experimental data of all samples from BLS and analyzed. I wrote and reviewed the manuscript. I appreciate all co-work from authors who are involved in this work.

When one door closes, another opens.

- Alexander Graham Bell

Preface

For decades, the application spectrum of nano-scaled materials has been widened. But, there is still a demand to exploit new physical behavior of those materials. Nano-scaled materials usually show distinctive properties compared to the bulk state, which is in particular the case for mechanical, thermal and phononic properties, as demonstrated in this work for different types of nano-scaled colloidal structures. In this thesis, the synthesis, the self-assembly of colloids, the characterization, and the particle vibration spectroscopy utilizing Brillouin light scattering (BLS) spectroscopy are described. Control over the hypersonic resonance of polymer colloids requires tailored colloidal synthesis.

Various types of particles with narrow size distribution were synthesized and colloidal structures (i.e., face-centered cubic) on solid substrates (glass or silicon wafer) were prepared by drop-evaporation method or vertical lift deposition. The samples were investigated by BLS spectroscopy to study the colloid mechanical resonances and interparticle interactions. BLS is a high-resolution spectroscopic method that can sensitively detect particle vibrations in the GHz regime through inelastic light scattering in analogy to THz Raman molecular vibration spectroscopy. Access to particle vibrations and interactions allow estimation of colloid elastic moduli, glass transition, and direct observation of the surface mobility, respectively.

The experimental results yielded the following information: First, polystyrene (PS) nanoparticles (NPs) with different chemical compositions (different comonomers) have distinct particle interactions, elastic modulus, and surface softening temperature (T_s). Second, surface tuning of PS NPs were achieved by chemical and physical methods; (i) chemically bonded groups (by two-step surfactant-free polymerization), (ii) physically adsorbed groups (by layer-by-layer adsorption method) led to PS NP systems with thin (8 ~ 18 nm for chemically bonded groups, 1 ~ 2 nm for physically adsorbed groups) shells atop the PS core. The presence of the thin shell modified particle interactions, elastic modulus, T_s, and glass transition temperature ($T_g > T_s$). Third, poly (butyl methacrylate) (PBMA), a low T_g (~ 290 K) polymer compared to the PS core, was introduced on top of the PS core with different PBMA thicknesses. For this core-shell NP structure, the shear modulus decreased with increasing PBMA shell thickness. Interestingly, while the T_g of the PS core was virtually constant, an elevation of the T_g of PBMA shell was found with decreasing PBMA thickness.

Overall the results in this dissertation suggest that nanoparticle modulus and thermomechanical behavior can be tuned independently through tailored particle architectures and compositions. In addition, it is shown that BLS is a non-contact and no destructive sensitive spectroscopy method that can provide elastic modulus and thermal properties of nanoparticles. The results from BLS were complemented with the finite element method (FEM), and modulated differential scanning calorimetry (MDSC).

Table of Contents

List of abbreviations

2D	Two-dimensional
3D	Three-dimensional
APS	Ammonium peroxodisulfate
ATRP	Atom transfer radical polymerization
BLS	Brillouin light scattering
c_{L}, c_{l}	Longitudinal sound velocity
c_t	Transverse sound velocity
DLS	Dynamic light scattering
DOS	Density of vibrational state
DSC	Differential scanning calorimetry
MDSC	Modulated differential scanning calorimetry
DVB	Divinyl benzene
FCC	Face-centered cubic
FEM	Finite element method
FP	Fabry-Perot
FRP	Free-radical polymerization
FT-IR	Fourier-transform infrared spectroscopy
G	Shear modulus
JKR	Johnson-Kendall-Roberts
KPS	Potassium persulfate
LB	Langmuir-Blodgett
LbL	Layer-by-layer
MDSC	Modulated differential scanning calorimetry
NaVBS	Sodium 4-vinylbenzylsulfonate
NMP	Nitroxide mediated polymerization
NP	Nanoparticle
PAH	Poly(allylamine hydrochloride)
PBMA	Poly(n-butyl methacrylate)
PDADMAC	Poly(diallyldimethylammonium chloride)
PDMA	Poly(N,N-dimethylacrylamide)
PDMS	Polydimethylsiloxane
PEI	Poly(ethyleneimine)
PSS	Poly(sodium 4-styrenesulfonate)
PEGA initiator	Polyethyleneglycol-azo initiator
PMMA	Poly(methyl methacrylate)
PS	Polystyrene
PVA	Poly(vinyl alcohol)
PVAc	Poly(vinyl acetate)
PVP	Poly(vinylpyrollidone)
SEM	Scanning electron microscopy
SFEP	Surfactant-free emulsion polymerization
St	styrene
TEMPO	2,2,6,6-tetramethyl-piperidin-1-oxyl radical
TEOS	Tetraethylorthosilicate
T_g	Glass transition temperature
T_s	Surface softening temperature
VLD	Vertical lift deposition

Chapter 1. General Introduction

It is well known that technological breakthrough comes from a deep understanding of material properties. New discoveries of materials and properties always improve technologies for our life. For the past decades, research related to different types and designs of nano-scaled materials has continued because of their distinctive properties that are absent in the bulk phase and a variety applications such as drug delivery, surface coating, photonic and phononic crystals.[1,2] For nano-scaled materials, the physical properties depend not only on chemical composition but also on their dimension. Metallic materials at nanometer length scale show different optical, electrical, and mechanical properties from their corresponding bulk properties.[3] Nano-scaled polymers also have different physical properties.[4] However, their dimension-dependent properties can extend over broad range due to multi length scales inherent to polymers. Therefore, the size-dependent effect of polymer materials is expected to be observed over tens of nm. In addition, nanostructured polymer materials are easy to be prepared with different dimensinonality, as two-dimensional (2D, e.g. thin films) and three-dimensional (3D, e.g. nanoparticles (NPs)) structures.

Keddie *et al.* firstly reported a reduction of the glass transition temperature (T_g) of polystyrene (PS) thin films with tens of nanometers thickness on a silicon substrate using ellipsometry.[5] Since then, many researchers studied and reported T_g deviation of polymer thin films on different substrates or free-standing. Two major effects (i) free surface effect, and (ii) interfacial effect between polymer film and substrate, are considered to significantly impact on T_g variation.[6] To generalize the surface and interfacial effect with different dimensionality, polymer nanoparticles (NPs) have been considered next. Zhang *et al.*[4] found a reduction of T_g with decreasing diameter (< 200 nm) for PS NPs but Feng *et al.*[7] assigned this T_g suppression to the adsorbed surfactant on the PS surface in the aqueous phase. Additionally, Christie *et al.*[8] also supported the surfactant effect on PS NPs surface. The argument for a surface effect on the T_g suppression of polymer NPs relates to the existence of the outermost surface layer which is considered more mobile than the bulk-like core.[4,7,8] However, a commonly used thermal characterization method such as differential scanning calorimetry (DSC) has limitations to resolve different segmental dynamics of the outermost surface layer of polymer NPs due to the low volume fraction of this outer layer compared to the bulk material. Therefore, a new method has to be introduced that is more sensitive to the surface phase to measure the T_g of polymer NPs and provide information related to the outermost surface mobile layer.

Nowadays, inelastic light scattering is being used to develop the particle vibration spectroscopy, the analogue of the molecular vibration technology. Raman scattering and pump probe techniques can be applied but only for the particles with a diameter smaller than 20 nm.[9,10] Brillouin light scattering spectroscopy (BLS) probes several particle vibrations of sub-micrometer particles due to comparably higher sensitivity. The rich BLS spectra (frequencies and intensities) allow a unique

determination of the elastic mechanical properties of mesoscopic NPs. For isolated spherical NPs, the low frequencies of vibration can be calculated by the Lamb model.[11] The vibrational modes are described by (p, n, l), where p stands for torsional (t) and spheroidal (s) modes. The torsional modes have pure shear motions, whereas spheroidal modes have both shear and stretching motions. The other elements, n and l, indicate the radial and angular dependence of the vibrational modes and those have frequencies inversely proportional to the NP size. The schematic simulation results (from finite element method, FEM) of displacement and deformation of spherical nanoparticles (NPs) which are related with particle vibration modes ($n = 1$, and $l = 2, 3, 4, 5, 6, 7$) are illustrated in **Chapter 8.1**. The lowest frequency, ($s,1,2$), of spherical NPs with diameter d, is calculated by the Lamb expression, $f(s,1,2) = A\, C_t\, d^{-1}$ where A is dimensionless and depends on the ratio of transverse C_t to longitudinal C_l sound velocity of the NPs. The ($s,1,2$) mode of independent NP's is a single peak and the frequency can be computed by finite element method (FEM) assuming the NP elasticity. The ($s,1,2$) mode is, however, sensitive to particle-particle interactions exhibiting both blue shift and splitting.[12] The temperature-dependent BLS can be used to measure softening temperature (T_s) and T_g of polymer NPs. The softening temperature is identified by the red shift of the ($s,1,2$) mode due to material softening upon heating, whereas at T_g ($>T_s$) the NP's eigenmodes disappear due to the formation of a contiguous film. Modulated differential scanning calorimetry (MDSC) was used to measure T_g of NPs to support the experimental T_g values from BLS.

The previous studies of polymer NPs have raised two questions (i) if the surface mobile layer exists and (ii) if so, can they make an impact on the thermal-mechanical behavior of polymer NPs.[4,7] In this dissertation, we will give answers to both questions. A variety of tailored colloid synthesis methods, different types of polymer colloids were prepared. PS NPs (d~200 nm) were prepared with different comonomers and a crosslinker by surfactant-free emulsion polymerization to study the chemical composition and particle size effect on elastic modulus and thermal mechanical behavior (T_s and T_g) of NPs in **Chapter 6.1**. To examine the effect of different types of thin surface layers on the properties of PS NPs, layer-by-layer (LbL) adsorption method and two-step surfactant-free emulsion polymerization were used to prepare polymer NPs with various thin shells. The adsorbed thin shell (thickness 1 – 2 nm) and chemically bonded shell (thickness 8 – 18 nm) on PS NPs were investigated in **Chapter 6.2**. Finally, to assess the interface effect between two different materials in spherical geometry, a core-shell structure with high T_g-contrast polymers was adopted. A poly(butyl methacrylate) (PBMA) shell with low T_g and different thickness (7, 34, 58 nm) was formed atop a PS core. Furthermore, a poly(methyl methacrylate) (PMMA) shell with high T_g and different thickness (8, 16 nm) on a PS core was prepared and these two particle architectures were studied by BLS, as described in **Chapter 6.3**. In addition, the geometric effect was also compared with 2D bilayer films from a published paper.

All basic information to complete my Ph.D. research is written from **Chapter 2** to **Chapter 5**. In **Chapter 2**, we discuss the colloid synthesis methods not only for single NPs made with metal,

silica, and polymer but also the NPs with core-shell architecture and different materials. In **Chapter 3**, various colloidal assembly methods such as drop-evaporation, Langmuir-Blodgett trough, vertical lift deposition, and spin coating method are introduced to fabricate well-ordered particle structures (i.e. face-centered cubic (FCC) structure) for BLS characterization. The general characterization methods used for the synthesized and prepared samples are described in **Chapter 4**. The introduction for BLS is provided in **Chapter 5**. In this chapter, we discuss the basic principles of BLS, Tandem Fabry-Perot interferometer, experimental setup, and scattering geometry. Finally, the result and discussion of three pieces of researches mentioned are written in **Chapter 6**.

Chapter 2. Colloidal Synthesis

For over 140 years, colloids have become an important role in the research of chemistry, material science, condensed matter physics, fluid dynamics, and biology. The immense importance of colloids comes from a rich variety of their commercial applications and products such as pharmaceuticals, cosmetics, inks, paints, food, lubrication, paper coating, catalyst, electrophotographic toner, and so on.

Colloids are usually defined as small particles in the range of a few nanometers to one micrometer with a dispersed phase (such as solid, liquid or gas) in the overall continuous phase (such as solid, liquid, or gas). Common examples are milk, smoke, fog, paints, and gels. The various types of colloidal systems are categorized by the phases of dispersed and continuous. Dispersed solid or liquid in a gas phase is termed as "aerosol" (e.g. smoke and fog). Dispersed liquid in liquid phase is defined "emulsion" (e.g. milk and mayonnaise). "Colloidal sol" or "dispersion" for solid particles dispersed in liquid phase (e.g. paint and ink). [13]

Fundamental research on colloids generally needs the monodispersed and uniform colloidal particles in shape, size, and composition. Therefore, cutting-edge synthetic strategies that can produce monodispersed colloids in mass quantity are used for colloidal research.[14] Due to continuous research on synthetic strategies, various types of colloids can be synthesized with narrow size distribution and similar size, shape, and surface charge within 1-2% deviation.[15] Spherically shaped colloids are the most developed example among the monodisperse systems. Because the type of spherical colloids is usually formed to minimize the interfacial energy and easily developed through the nucleation and growth processes. Therefore, various chemical synthesis route to produce spherical colloids from organic and inorganic materials.

2.1. Polymer nanoparticle

Polymer nanoparticles are important to be applied for modern technologies such as drug delivery, impact modifier, photonic and phononic crystals. Generally, polymer nanoparticles synthesized by heterophase polymerization methods such as emulsion, miniemulsion, microemulsion, suspension, micro suspension, and dispersion polymerization. The various heterophase polymerization methods are shown in **Table 2.1**. Heterophase polymerization has two separate phases in a system which have dispersed polymer particle (or starting insoluble monomer droplets) in a liquid medium. Also, an initiator which is soluble in a liquid medium or in a monomer droplet, and a dispersion stabilizer which stabilizes monomer droplets and polymer particles in a liquid medium. The types and quantity of each ingredient generally effect on all physical properties of polymers such as particle size, molecular weight and so on. Heterogenous polymerization

methods can produce polymer particles size rages from about 5 nm to 2 mm or larger[16] and different size distribution.

Table 2.1. Overview of heterophase polymerization methods[17]

Polymerization type	Initiator	Stabilizer	Process	Particle size range
Emulsion	lyophobe lyophil	all kinds or none	batch, semi-batch, continuous, seed	5 nm - 10 μm
Miniemulsion	lyophil, lyophobe	all kinds	batch, semi-batch, continuous	50 - 500 nm
Microemulsion	lyophil, lyophobe	all kinds	batch, semibatch	10 - 100 nm
Dispersion	lyophil	Polymeric	batch	1 - 20 μm
Suspension	lyophobe protective	Polymeric or colloid	mainly batch	10 - 500 μm

Among the heterophase polymerization methods, surfactant-free emulsion polymerization (SFEP) method was chosen to obtain pure polymer nanoparticles with narrow size distribution and without any additional substances. SFEP does not need any extra substance (i.e., additives) such as surfactants or dispersion stabilizers. It only uses monomer, initiator, and liquid medium (in most cases, water). Therefore, only unreacted monomer is needed to be removed after polymerization process as a purification process. Therefore, additional purification process to remove additives is not necessary.

In 1965, SFEP was firstly introduced to synthesize monodispersed polystyrene (PS), poly(methyl methacrylate) (PMMA) and poly(vinyl acetate) (PVA) with potassium persulfate initiator in the absence of additional emulsifier.[18] Polymer nanoparticle prepared by SFEP is stabilized in aqueous medium only by the surface bound chemical groups (usually sulfate groups supplied from persulfate initiator) which offer high charge density to give electrostatic repulsive force between nanoparticles.[19] The repulsive force between particles prevents particle coagulation in an aqueous medium. Well-known initiators for SFEP are : potassium peroxodisulfate (KPS), 2,2'-azobis(2-amidinopro-pane)dihydrochloride, or polyethyleneglycol-azo initiators (PEGA types).[20,21] For KPS, sulfate ions are provided by the initiation process (**Equation 2.1**), and it generate radicals where monomer can propagate to polymer in an aqueous medium (**Equation 2.2 and 2.3**).

$$S_2O_8^{2-} \rightarrow 2\ SO_4^-\cdot \qquad\qquad (2.1)$$

$$SO_4^-\cdot + M \rightarrow SO_4^-M\cdot \qquad\qquad (2.2)$$

$$SO_4^-M\cdot + M_n \rightarrow SO_4^-M_{n+1}\cdot \qquad\qquad (2.3)$$

After a nucleation, the growth of the particles in SFEP, two major different mechanisms are postulated. (i) Polymerization at the surface of monomer swollen polymer particles (**Figure 2.1a**)[22,23] and (ii) heterocoagulation of new unstable monomer swollen particles from the aqueous medium with the core particle (shown in **Figure 2.1b**).[24]
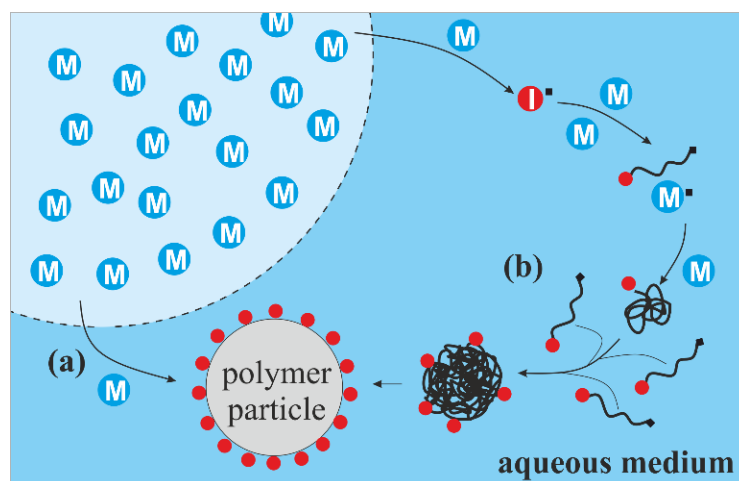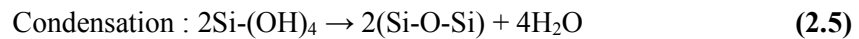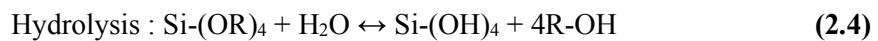

Figure. 2.1. A schematic illustration of the surfactant free emulsion polymerization. **(a)** polymerization at the surface monomer swollen polymer particles, **(b)** heterocoagulation of new unstable monomer swollen particles from the aqueous medium with the core particle.

For styrene, one of the monomers with low water solubility, it grows in aqueous medium to oligomeric radicals with sulfate end groups, which form micelles as in emulsion polymerization.[25] On the other hand, for methacrylate, a monomer with higher water solubility, polymer particles are formed by heterocoagulation of growing chains with 60 – 80 repeating units.[26] Consecutive polymerization processes for both case occurs in monomer swollen particles.[27] The produced polymers by SFEP have two major differences from emulsion polymerization ; (i) the lower particle number density. The polymer particle number without a surfactant is 100 times less than with surfactant. (ii) The lower molecular weight of the polymer by SFEP is a factor of 10 lower.[28] These major differences come from growth kinetics change based on the adsorbed surfactant layer on the particle surface which affects monomer solubility in particle, interfacial tension, or surface solubility.

2.2. Silica nanoparticles

For different chemical composition from polymer nanoparticles, silica particles were prepared and analyzed by Brillouin light scattering spectroscopy. Silica nanoparticles are important material

in various research fields, because of their various industrial applications, such as catalyst, medicine, pigments, electronic, and, thermal insulators.[29] An extremely useful method to prepare monodispersed silica particles was introduced in 1968 by Stöber et al.[30] A dilute tetraethylorthosilicate (TEOS) solution was hydrolyzed in ethanol with ammonia as a catalyst at high pH and it formed silica particles with narrow size distribution and sphere shape. The diameter of the particles can be controlled from 50 nm to 2 μm. The final particle size is determined by the type of silicon alkoxide and alcohol. By changing alcohol chain length of solvent from one to longer, particle size gets bigger. The shortest chain length alcohol, methanol, provides the smallest silica particles size. As chain length of alcohol increases, silica particles get bigger and size distribution of the particle gets wider. Recent researches postulated two mechanisms for silica particle formation, (i) hydrolysis for silanol groups from silicon alkoxide (**Equation 2.4**) and (ii) condensation for siloxane bridges (**Equation 2.5**)

$$\text{Hydrolysis} : Si\text{-}(OR)_4 + H_2O \leftrightarrow Si\text{-}(OH)_4 + 4R\text{-}OH \tag{2.4}$$

$$\text{Condensation} : 2Si\text{-}(OH)_4 \rightarrow 2(Si\text{-}O\text{-}Si) + 4H_2O \tag{2.5}$$

The condensation reaction depending on the reaction environment, it may form a three-dimensional gel network or single monodisperse particles.[31] With TEOS, the final particle size is determined within 3 - 10 hrs after the reaction starts. The particle size gets bigger as water and ammonia concentration increase. On the other hand, when TEOS concentration increases, the particle size decreases and size distribution increases. Tan el al.,[32] studied the relationship between reaction temperature and silica particle size. They found that the reaction in short-chain alcohol (ethanol or n-propanol) at -20 ºC can produce silica particle in a wide range of 200 nm – 2 μm. Bogush and Zukoski[33] found that the existence of electrolyte increases the particle size. NaCl concentration changes from 0 to 10^{-4} M, produces silica nanoparticles in the size of 340 nm to 710 nm. However, wide size distribution or new particles formation is a big obstacle when big SiO_2 nanoparticles are synthesized. To make narrow size distribution of big silica particles ($d >= 800$ nm), seeded growth technique was introduced and described.[34] In this technique, when the supersaturation of silica particles by Stöber method reaches the critical level, primary nuclei of silica particles are suddenly generated and aggregate to form stable particles. The primary nuclei are mostly used for the particle growth for the first stable particles. Therefore, the formation of the secondary stable particle is suppressed. The advantage of this technique is that more monodisperse particle can be prepared, and the disadvantage is the size of the silica particle cannot be larger than 1 μm.

2.3. Silver nanoparticles

Metal nanoparticles are well-known and well-developed materials for their fundamental knowledge and enormous applications. Various different types of metal nanoparticles are applied for catalysts, electronic materials, surface coating, sensing materials, plasmonic, photonic, and phononic materials.[3] With cutting-edge technique, metal nanoparticles size can be synthesized less than one nanometer. Metallic nanoparticles can be made by two major methods: (i) mechanical crush of metallic aggregates (physical top-down method) or (ii) nucleation and growth from metallic ions (chemical bottom-up method). The mechanical crush method yields nanoparticles with uncontrolled size and very broad size distribution. Therefore, chemical bottom-up method is a favored way to make metal nanoparticles in controlled size and narrow size distribution. Most usual and convenient way is using reduction reaction of transition metal salts.[35]

Among metal materials, silver has the highest thermal and electrical conductivity. Indeed, silver ions and silver-based composites has antimicrobial effect which is toxic to harmful microorganisms for human. With various benefits, silver nanoparticles (Ag NPs) have been attracted in academia and industries. However, the synthesis method for Ag NPs is limited, not easy to give a deliberate control on size and size distribution. Various methods have been developed to prepare Ag NPs : (i) a chemical reduction method using silver ions in aqueous solution,[36] (ii) a thermal decomposition method,[37] (iii) a photo-reduction method,[38] and (iv) a radiation reduction method.[39]

Among the methods to synthesize Ag NPs, the chemical reduction method is the most commonly used way to synthesize well-controlled Ag NPs. Recently, many papers have exploited the formation mechanism of Ag NPs including nucleation and growth mechanism.[40–42] The mechanisms of Ag NPs formation is schematically illustrated in **Figure. 2.2**.

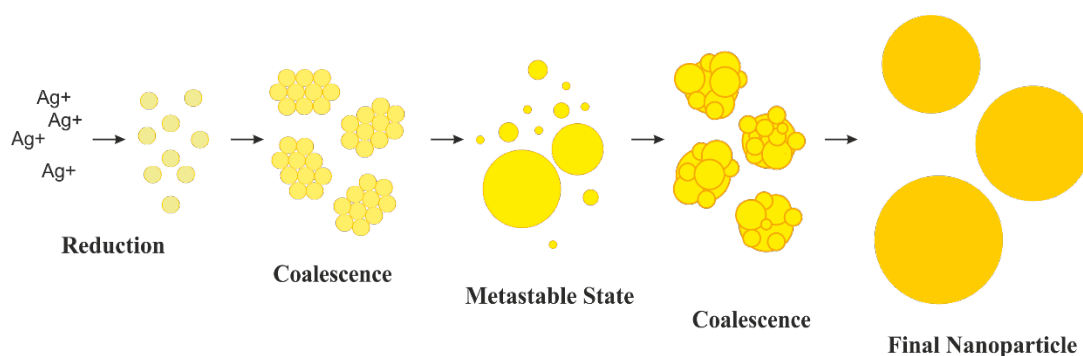**Figure 2.2.** A schematic illustration of Ag NPs formation mechanism via chemical reduction method. (redrawn according to Ref. [40])

In the chemical reduction method for Ag NPs, various parameters such as initial silver salt concentrations, reducing agent types and concentration, types and concentration of stabilizers are the keys to the control nucleation and growth process, determining particle morphology, size, and

size distribution. For example, Ag NPs synthesis with $AgNO_3$ only with reducing agent, $NaBH_4$, at room temperature generally produces around 10 nm size particles.[43] When Ag NPs were prepared with a stabilizer such as poly(vinylpyrollidone) (PVP), poly(vinyl alcohol) (PVA), Ag NPs size can be over 10 nm size. Because the stabilizers give dispersion stability to Ag NPs in an aqueous phase and protect the Ag NPs from agglomeration. However, the reaction rate of Ag NPs synthesis can be slower with steric stabilizer such as PVP or PVA.[44,45] Steric stabilizer covers the particle and interrupts further particle growth and aggregation.[46] A traditional way to control particle size and size distribution is a two-stepped reduction method.[47] In the first step, 'seeds' are formed by using a strong reduction of silver ions. As a second step, particles grow steadily by the reduction of Ag ions with a weak reducing agent. With this method, the Ag NPs size range between 20 and 170 nm can be prepared. But, this method cannot offer good reproducibility. To overcome the drawbacks mentioned above, a new technique which using citrate reduction of silver ions in aqueous medium has been used. In this method, citrate plays a double role as a reducing agent and a stabilizer.[46] Because of the weak interaction between sodium citrate and the metal surface, this method provides quick Ag NPs generation. However, the citrate ion cannot provide controlled silver ion reduction rate for monodispersed big Ag NPs because of its multirole as a weak reducing agent and a strong stabilizer, which results uncontrolled nucleation, growth of Ag NPs. Recently, a new method using citration reduction with tannic acid has been introduced to control growth kinetics. It showed good size and size distribution.[48,49]

2.4. Particles with core-shell architecture

Particles with core-shell architecture are composed of a special structure of nanocomposite materials. They have concentric core particles with a single material and are coated by another material. Particles with core-shell architecture are very practical materials with modified and improved properties than nanoparticles with a single composition of core or shell in the same size. Therefore, for specific applications, particles with core-shell architecture are favored over single material nanoparticles. Their properties can be modified and optimized by changing the composition of core or shell materials, or ratio of core to shell.[50] The purpose of shell coating on the core particles are tremendously diversified, such increases of the functionality, particle stability and dispersibility, surface modification, and control of the core material release, and so on. For core-shell nanoparticles, core particle reactivity can be reduced or thermal conductivity changed because of the shell coating. Whereas, overall particle stability and core particle dispersibility increase. Numerous methods to prepare shell coating on core particles with a number of different materials have been developed and established. Most of them use controlled adsorption or reaction

(e.g. layer-by-layer method, two-step polymerization, and sol-gel condensation) which can form a controlled coating layer on the surface of core particles.

2.4.1. Two-step emulsion polymerization

In emulsion polymerization, the formation of polymer particles is highly affected by the particle growth rate. Therefore, the controlled particle growth rate is the key to synthesize core-shell structured polymer-polymer particles. The growth rate should be kept low to suppress the nucleation of new particles. The growth rate of a polymer can be kept low by (i) reduction of monomer swelling ratio of polymer particles or (ii) starvation of monomer feed to polymer particles.[51] A reduced monomer swelling ratio of particles can be achieved by cross-linker. The cross-linker forms a polymer network between polymer chains inside the polymer particles so that the monomer-swelling ratio of polymer particles decreases. The latter strategy (ii) can be obtained when polymer particles are under a monomer starvation condition with a semi-batch polymerization. In traditional one-step batch process, the particle growth rate is determined thermodynamically by monomer diffusion rate from monomer droplet to polymer particle. Therefore, the rate of polymer growth cannot be controlled. Meanwhile, for the semi-batch polymerization process, monomer feed rate to system is under control to keep starvation condition of monomer. The low monomer feed rate effects on the particle growth rate. Therefore, a semi-batch process is usually used for submicron-sized polymer particles and core-shell particles.

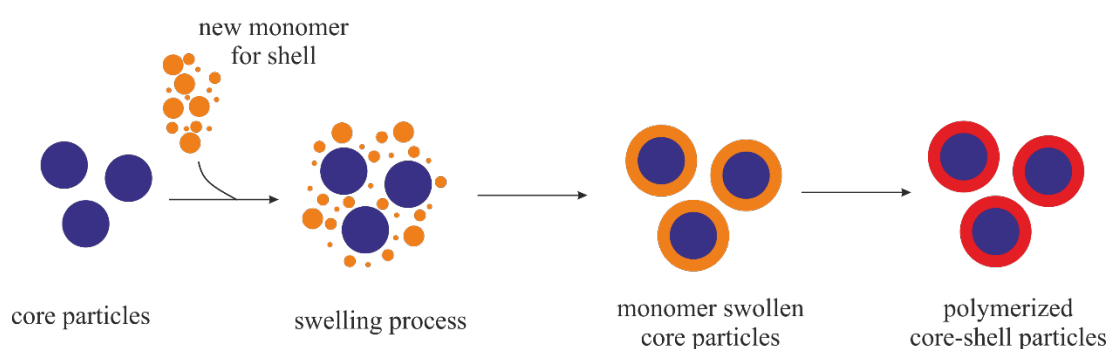**Figure 2.3.** A scheme of 2nd step mechanism of two-step emulsion polymerization for the shell formation on core polymer particles. The figures were adapted from the original references [52].

2.4.2. Layer-by-layer deposition method

Layer-by-layer (LbL) method was introduced as a polymer self-assembly process using electrostatic interactions which can construct multilayered materials.[53] The basic principle for this

technique was demonstrated, how alternating multilayer assemblies of positive and negative polyelectrolytes form on an electrically charged substrate. In this method, an ionic attractive force between the opposite charges play an important role to induce physisorption between the oppositely charged layers. For example, when the anionic polyelectrolyte forms a layer on a positive charged substrate, it brings more than equal charge so that reversal charge (negative) on the outer most layer. Consequently, this allows (i) self-limited adsorption for a single layer comes from equally charged molecules repulsion and (ii) good adsorption of oppositely charged layer on top of the first one in a next step. The repetition in cyclic fashion of the adsorption steps build up multilayer structure.[54] The procedure of multilayer build-up is schematically shown in **Figure 2.4a**. One of the advantages of polyelectrolyte is good adhesion between the oppositely charged physisorbed layers. The formed layer covers all over the surface of the underlying layer or substrate. Therefore, the newly created layer by polyelectrolyte shows its physical property rather than the underlying surface.

In LbL experimental process (shown in **Figure 2.4b**), a positive charged solid substrate is immersed in a solution with a negative charged polyelectrolytes. The anionic polyelectrolyte layer is formed on the surface via electrostatic attraction force. After the immersion, rinse the excessive negative polyelectrolyte with distilled water. This step also stabilizes weakly adsorbed polyelectrolyte layer.[55] Then, the substrate is immersed in a solution with cationic polyelectrolyte. By consecutive and cyclic immersion processes, multilayer material can be easily prepared.[53] The range of typical adsorption time for each layer from several to 30 mins. Each polyelectrolyte layer thickness is approximately estimated around 1-2 nm.[56] Therefore, the total thickness of multilayers can be controlled by the number of adsorbed polyelectrolyte layers.
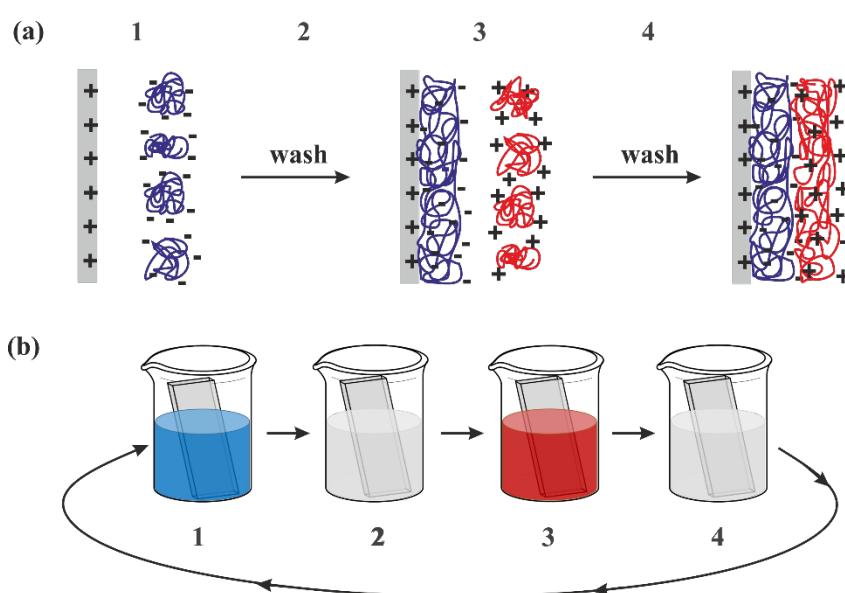

Figure 2.4. Schematic illustrations of LbL methods: **(a)** the physisorption of alternative electrolyte layers on a positive charged substrate, **(b)** the experimental process of the LbL method. The figures were adapted from the original references [54,57].

The ionic strength in polyelectrolyte solution is one of the important factors which determines the layer growing mechanism. The different ionic strength leads the change of charge compensation for the polyelectrolyte layer formation. With high salt (e.g., NaCl) concentration, the thickness and surface roughness of the layer are much larger.[58] The commonly used polyelectrolytes are poly(diallyldimethylammonium chloride) (PDADMAC), poly(ethyleneimine) (PEI), poly(allylamine hydrochloride) (PAH) for cationic and poly(styrene sulfonate) (PSS) for anionic electrolytes.

The application of this technique also has been expanded to particles for core-shell structure.[59] The multilayer coatings on sub-micrometer sized particles is an expansion of the LbL method from 2D film geometry to form 3D structure.[60] The LbL method is a useful method to prepare a core-shell structure because the shell composition and thickness can be easily tailored.

Chapter 3. Colloidal Assemblies

Colloidal assemblies have attracted because of their unique properties can be applied for surface patterning, nano-lithography, plasmonics,[61] photonics,[62] and phononics.[63] Many methods for achieving a face-centered cubic (fcc) structure of colloidal spheres have been developed including drop evaporation method, Langmuir-Blodgett trough, vertical lifting deposition, and spin coating method. The mechanism of formation of colloidal crystal has been explained by aggregation of colloidal particles. For all techniques, the evaporation rate of the dispersion medium is the key which leads self-assembly of colloidal particles through capillary force. Therefore, the optimum values for the evaporation rate are crucial for obtaining high quality crystal structure. Too much high or low evaporation rate causes stacking fault or cracks. The evaporation rate of the solvent can be determined by temperature, humidity, and types of dispersion medium. Temperature is an important factor which affect the evaporation rate of the solvent and self-assembly process both. High temperature causes poorly ordered structure and low temperature needs to much time to get the crystal structure.[64] A high humidity system is preferred than low to obtain high quality crystal. Because higher humidity increases the capillary forces between particles.[65]

3.1. Drop evaporation

Drop evaporation method dries drops of colloidal suspension and solution to remove a volatile solvent gradually on a solid surface. When suspension forms a droplet on a substrate, only the Brownian motion of the particle exists in the droplet. As a droplet thickness decreases by solvent evaporation, a thin water film starts to form on the substrate. Specifically, when the film thickness reaches comparable thickness with the particle size in the suspension, nucleation starts.[66] Then, the crystal grows from the nucleus continuously by particle flow along the water influx (in **Figure 3.1**). Many nucleation spots exist in the first stage, but they merge together and form one large domain. The important factors for crystal formation are (i) water influx to the nucleus and (ii) water film
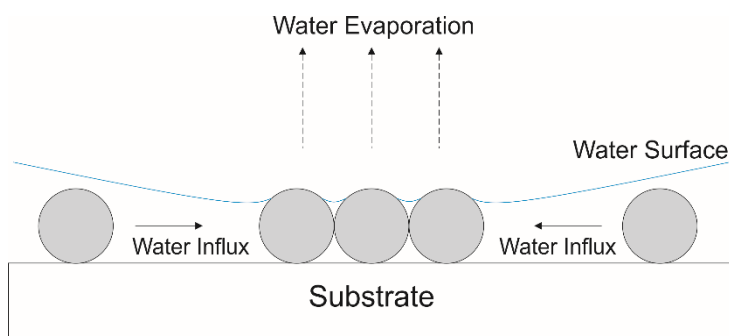

Figure 3.1. A scheme of nucleation and growth of particle film from colloidal suspension on a solid substrate. (redrawn according to Ref.[67])

thickness.[67] Water influx to the nucleus is determined by the water evaporation rate. Slow evaporation reduces water influx and particle transportation speed to the crystal nucleus so that the crystal growth reduces.[68]

The attractive forces from the lateral capillary forces between particles cause crystal growth and keep the structure firmly. The attractive force between particles in water medium is schematically shown in **Figure 3.2**. Using a liquid film on a solid substrate induces a stronger force for particle assembling when it is compared the attractive force between particles at the air-water interface. When the particles get closer, the menisci around the particles becomes symmetric or asymmetric which cause attractive and repulsive forces between the particles. The attractive or repulsive depends on the concave or convex of the overlapping menisci on the particle surface. The interparticle force is described in **Equation 3.1**.[69,70]

$$f = -2\pi\sigma Q_1 Q_2 q K_1(qL) \tag{3.1}$$

Here, σ is surface (interface) tension, $Q_i = \gamma_i \sin\theta_i$ ($i = 1,2$) is capillary charge of a particle. γ_i and θ_i are the radius of the contact line and the slope angle at the contact line of the respective particle (shown in **Figure 3.2**). q is the capillary constant ($q = \rho g/2r$), L is the distance between the particles. K_1 is the modified Bessel function of first order.
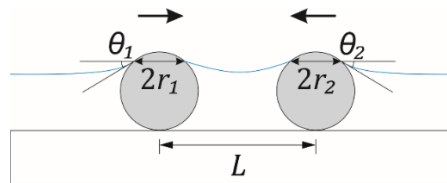

Figure 3.2. A schematic illustration of the particle attractive force during crystal growth

The force from **Equation 3.1** changes its signs (for attractive or repulsive force) depending on two angles θ_1 and θ_2. The same particles always attract each other. When particles which show $\theta_1 \cdot \theta_2 > 0$, interparticle forces are attractive, but different particles with $\theta_1 \cdot \theta_2 < 0$ for a special case, have repulsive force each other. The attractive and repulsive forces in this system are considered as lateral immersion and floatation capillary force, respectively to distinguish it as strong forces including capillary bridge force and existing in a liquid film. Approximately lateral floatation capillary force and immersion capillary force are proportional to the power of six and two of particle radius, respectively. Therefore, for small particles with submicron scale, the immersion capillary force overwhelms the floatation capillary force and contributes to the array formation of the particles.

3.2. Langmuir-Blodgett technique

The beginning of amphiphilic monolayer assembly on the water surface was Babylonian times.[71] A pioneering work understanding and exploiting the perfectly organizational capability of the air-water interface was done by Pockels and Langmuir.[72,73] A giant leap for this research was offered by the work of Blodgett.[74] He showed that well-organized amphiphilic monolayer (Langmuir monolayer) from the air-water interface can be transferred onto solid surfaces by layer-by-layer. This technique brought a highly ordered lamellar structure of amphiphilic layers and is called the Langmuir-Blodgett technique. The application of this method has been widened to a relatively new area for monolayer or multilayer of nanoparticles at the air-water interface.[17]

The behavior of spherical polymer particles at the air-water interface was quantified. The required energy for the particles withdraw from the interface and for the movement of the particles into the bulk water were expressed.[75]

$$E_{OUT} = \pi R^2 \gamma_{LA}(1 + cos\theta)^2 \tag{3.2}$$

$$E_{IN} = \pi R^2 \gamma_{LA}(1 - cos\theta)^2 \tag{3.3}$$

The R is the particle radius. γ_{LA} is the interfacial tension of liquid to air interface. θ is the obtuse angle between air-liquid interface and the plane on the particle surface. From the equations above (**Equation 3.2 and 3.3**), the relationship between the energy for withdraw and sink the particles can be obtained.

$$E_{OUT}/ E_{IN} = cot^4(\theta/2) \tag{3.4}$$

The ratio is quite small for all realistic θ value and thus the energy to move out from the water is less than the energy required to move a particle to the inside of the bulk water. This is the basic theory why the sphere layers are only fabricated on a substrate in upwards.[76]
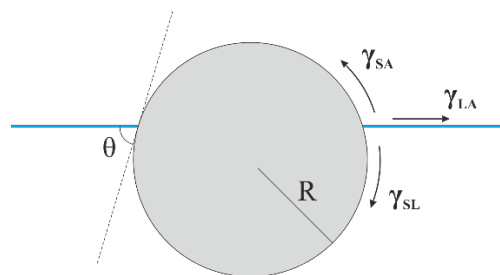

Figure 3.3. A schematic of forces at the air-water-solid phases (Redrawn according to Ref. [76])

The Langmuir-Blodgett (LB) trough is an apparatus which allows to fabricate monolayer or multilayer on a solid substrate of polymeric spheres. The substrate dipping device moves the substrate in upward and downward through air-water interface, automated Teflon movable barriers

moves from side to center to maintain the controlled surface.[77] A scheme of the LB trough apparatus is shown in **Figure 3.4**.
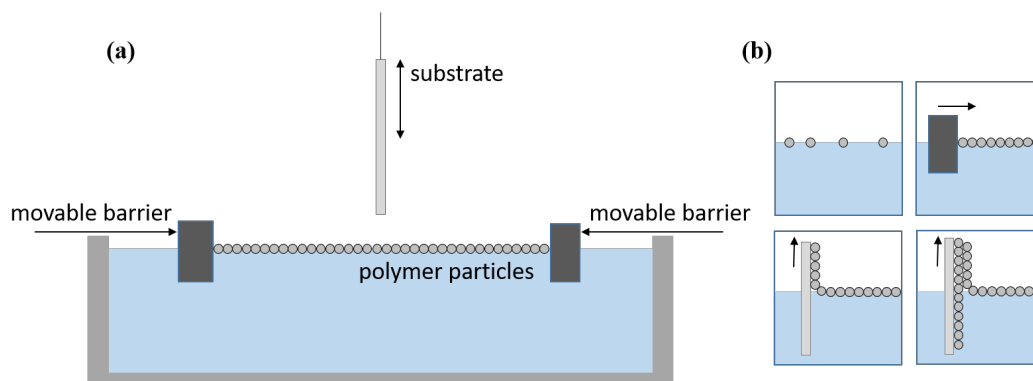

Figure 3.4. A scheme of Langmuir-Blodgett technique: **(a)** set up with liquid filled reservoir, movable barriers, a vertically movable substrate, and polymer particles. **(b)** A process of Langmuir-Blodgett technique.

For the LB technique, hydrophobicity of a colloid surface is mainly considered as an important factor. To control the hydrophobicity of the surface, two methods are usually used ; (i) surface functionalization of colloids, (ii) addition of surfactant or salt. Both methods are applicable as well. In the early stage of LB technique, it provides good technique to fabricate monolayer of colloids. Therefore, monolayer of hydrophobic particles (such as PS and silica particles) fabricated by LB technique was studied to figure out the relationship between interparticle forces and the monolayer structure. Later, LB technique also provided thickness controlled and well-organized 3D structured particle multilayers with surface-functionalized silica particles by repeating single layer depositions on a solid substrate.[78]

The addition of surfactant or salt is another method for well-structured multilayers of particles. Szekeres et al. studied effect of surfactants and the dispersion medium on the particle ordering by LB technique. Spherical silica particles with different sizes (357, 450, and 550 nm in diameter) were used to build up the 2-D and 3-D structures. The balance between hydrophobicity and hydrophilicity via surfactant adsorption on the particle surface should be controlled to fabricate the perfectly close-packed structure of particles on a glass substrate.[79] At air-water interface, salt concentration in water phase largely affects the structure of particle monolayer. At low salt concentration, interparticle repulsion forms a fairly ordered structure of the particle monolayer on water surface. While, at high concentration of electrolyte, 2D clusters of the particles form.[80]

3.3. Vertical lift deposition

Among the many methods to fabricate a well-ordered structure for colloidal particles, vertical lift deposition (VLD) method (also called dip coating method) is the most attractive method to fabricate highly-ordered colloidal multilayer because of its easiness and simplicity.[81] In addition, VLD provides a way to control the layer thickness.

In the VLD method, a substrate dips vertically in a colloids suspension and then lifts it up continuously from the suspension to form ordered layers of colloids. A schematic diagram of this method is illustrated in **Figure 3.5**. When a substrate with hydrophilic surface is placed into the suspension, a hydrophilic film is formed from the suspension along the substrate. Particle convection to the three phase (air-water-solid) contact line by the overall flow and capillary force between the particles lead particles to the ordered structure. The solvent evaporation rate and substrate lift speed are the keys to determine the structure of the particle arrays.
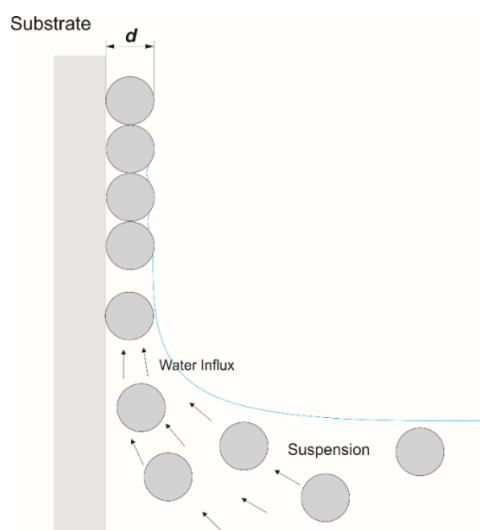
Figure 3.5. A schematic representation of particle convection to form ordered structure when a substrate is removed vertically from the surface of the colloidal suspension. The figures were adapted from the original references [82].

The evaporation rate of solvent is controlled by types of dispersion medium, temperature, and humidity. However, the evaporation rate only determines particle flux to the contact line in the suspension. When the substrate lifting speed is over the high velocity limit, the flux cannot catch up the substrate speed so that the disordered structure can be formed on the moving substrate. Therefore, the lifting speed should be suppressed under the limit velocity to avoid the formation of a disordered structure.

Landau and Levich[83] originally introduced an expression which can estimate a film thickness h of uniform wetting layer by VLD method at constant velocity V from a Newtonian fluid of viscosity μ,

$$h = 0.946 \, l_C \, N_C{}^{2/3}, \tag{3.5}$$

where, $l_C = (\gamma \, / \, \rho g)^{1/2}$ designates the capillary length for the fluid (γ is the surface tension, ρ is the fluid density, and g is gravity acceleration). $N_C = \mu V / \gamma$ is the capillary number. When the film forms with the thickness h smaller than particle diameter D (h < D), particles are drawn to the contact line by the convection flow but cannot move to other particles which is in the crystal film because of size.[84] During drying process, the volume fraction of occupied particle in a wet film increases from the initial value, $\emptyset_i$ to a limit value close to the maximum volume fraction of particle packing, $\emptyset_l$. The deposited particle film thickness, h_P, is expressed by:

$$h_P = 0.946 \, \frac{\emptyset_i}{\emptyset_l} \, l_C \, N_C{}^{2/3}. \tag{3.6}$$

With **Equation 3.5 and 3.6**, the minimum lifting speed of the substrate can be predicted, and the thickness of the deposited particle film can be estimated because it is proportional to $V^{2/3}$.[85]

The VLD method bases on the particle displacement from colloidal suspension to the crystal growing site, which is induced by the liquid influx. Therefore, it has limitation to fabricate film thickness thicker than 1000 nm or thinner than 20 nm layers from the suspension with highly diluted or highly viscous.[86]

3.4. Spin coating method

Spin coating method is an inexpensive technique for fabricate regular nanoparticle array in a large area. Therefore, it has been recently emerged and widely used to make multilayer colloidal films. This technique also found a new route for a fundamental research of shear-induced crystallization.[87] Despite the dynamics of spin coating is widely under investigation for simple one-component fluids such as polymer solutions, the formation mechanism of colloidal crystal film by spin coating has not been clearly explained.

Spin coating process of colloids has four stages (i) deposition, (ii) spin-up and spin-off, (iii) evaporation of dispersion medium, and (iv) the formation of layers (shown in **Figure 3.6**). In the first stage, the dropped particle dispersion on a stationary substrate forms a puddle due to surface tension of the dispersion. After the substrate starts to rotate, excessive dispersion spun out from the substrate. Then, as aqueous phase of the dispersion evaporates, the nanoparticles start to assemble itself. Finally, colloid crystal film with monolayer or multilayer are formed. There are a variety of factors affect the structure of spin coated colloidal crystal which can be described in particle dispersion property and spin coating condition. The properties of dispersion are particle size, size distribution, volatility and viscosity of dispersion medium, dispersant, and the particle

concentration. Spin coating conditions such as rotation and acceleration rates of a substrate influence the dispersion spread and evaporation of aqueous medium.[88,89]
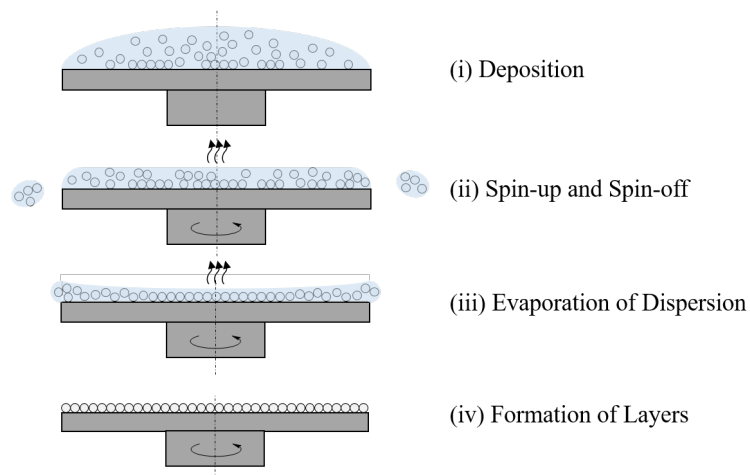

Figure 3.6. A scheme of the spin coating process of colloids. The adapted figure is from original reference [88].

The spin coating method is remarkably simple to conduct. However, it is not simple to identify the important parameters which rule film formation during the spin coating process. Therefore, simplification of approximate model for spin coating is required. The factors such as effect of evaporation, the presence of a gas phase, the specific character of dispersion, and non-Newtonian behavior are neglected. As a simple model, spin coating of polymer solution with volatile solvent can be considered. The thickness change comes from solvent evaporation including correction, E, is expressed below.

$$\frac{\mathrm{d}L}{\mathrm{d}t} = -(1-c)\frac{2\omega^2 h^3}{3v} - E \qquad (3.7)$$

$\mathrm{d}L/\mathrm{d}t$ is in terms of solvent volume change per unit area (m/s), c is the solid concentration in solution (v/v), $\omega = 2\pi f$ (where f is rotation rate), h is the thickness, $v = \eta / \rho$ (where η is the viscosity and ρ is the density of the solvent). Due to the impossibility to measure or estimate the actual value E, E is considered as constant with time. If E is allowed to change during the process, the only small change in final thickness happens.[90] This model has an assumption that spin coating is made up of two different stages ; (i) initial step of flow domination, (ii) second and final step of solvent evaporation domination. Later, this model was developed considering solvent evaporation for both steps. Also, the diffusion and advection of the solvent in the vapor and liquid phase while rotates during the process can affect the evaporation rate and cause different thickness profiles of the deposited film.[91] Therefore, the thickness fringe was observed.[87] At the initial stage, the fluid height is higher at the center of the rotational substrate, but it tends to spread evenly to form a flat plane.

Chapter 4. Colloidal Characterization

4.1. Scanning electron microscopy

Scanning electron microscopy (SEM) is the most widely used and a standard characterization method to acquire topographical information of nanostructured materials. When it is compared to an optical microscope, electron microscopy uses accelerated electrons as the imaging process source. The small wavelength λ of accelerated electrons allows the microscopy to provide high resolution down to the nanometer scale. The equation of maximum resolution (which means the minimum distinguishable distance between two individual points, d) is given by Abbé criterion,

$$d = \frac{\lambda}{2 \cdot NA} = \frac{\lambda}{2 \cdot \eta \sin \alpha} \qquad \textbf{(4.1)}$$

where, λ is the wavelength of accelerated electrons and NA is the numerical aperture of the objective lens and same to $\eta \sin \alpha$, η is the refractive index of the imaging medium and α is half of the objective angular aperture.

Polymer nanomaterials are more difficult to get images than metals in SEM characterization. Because polymer materials are made primarily up with carbon and hydrogen atoms. The low atomic number and low density of polymer materials cause poor electron scattering which results in low contrast. When SEM is measured, the electrons from electron gun accumulate charge and heat in the sample on electrically insulating polymer materials. The strong local accumulation of charge and heat degrade lead to polymer chain decomposition or/and crosslinking. Therefore, low voltage SEM (0.5 – 5.0 keV) technique was introduced and applied for the morphology characterization of polymer materials. Low voltage SEM reduces charging bad effects and improves contrast.
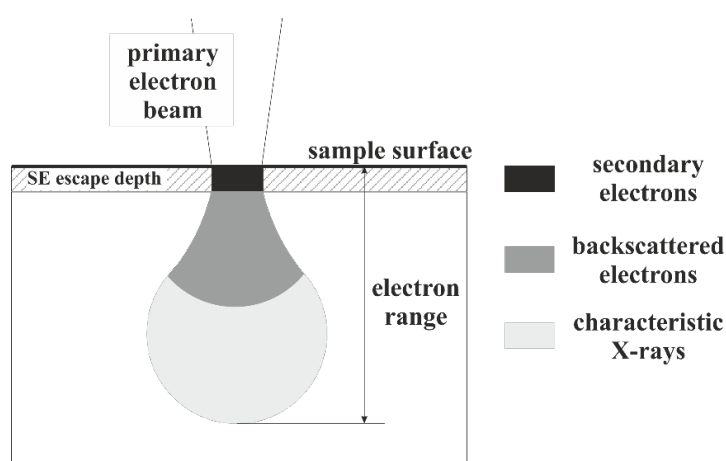

Figure 4.1. A schematic illustration of SEM induced beam-sample interaction volume. (Redrawn according to Ref. [92])

SEM beam and sample interaction volume schematically illustrated in **Figure 4.1**. When primary electrons from the electron gun irradiates the sample surface, a teardrop-shaped interaction volume is induced. The size and shape of interaction volume comes from beam-sample interaction, and it depends on incident beam energy and chemical composition of the sample.[93] The secondary electrons (E < 50 eV) are ejected from the sample atom by primary beam-sample interaction. The ejected electron stays close to the generated place because of their low energy, this allows electron microscopy to use for the imaging process. In case of polymer materials, the secondary electrons escape from the depth of 20 nm from the sample surface independent on the incident beam energy. Therefore, it is important to use low accelerating voltage to reduce the interaction volume less than 20 nm escape depth.[92] Detection of secondary electrons provides the topographical information of the sample surface. Backscattered electrons have higher energy than secondary electrons, they come from elastic scattering when primary electrons hit the sample atom. The intensity of backscattered electrons is sensitively dependent on the atomic number of the sample, so it can be used to visualize
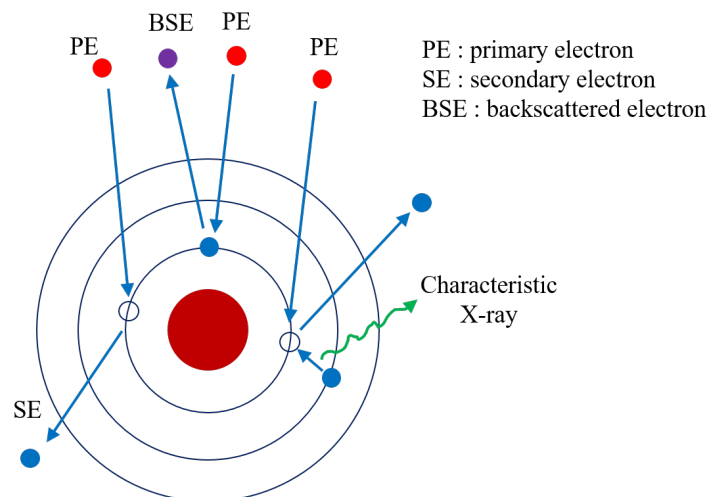
Figure 4.2. A scheme of secondary and backscattered electrons and x-ray generation from the sample atom by primary electron from SEM

contrast based on material difference. In addition to this, detection of x-ray is also available with SEM. When the incident primary electron excites an electron in an inner shell, eliminating it from the shell and creating an electron hole in that position. Another electron in outer shell fills the hole. While the electron in the higher energy state (outer shell) moves to the lower energy state (inner shell), it releases the X-ray as much as the difference between the higher and lower energy state. Therefore, energy dispersive x-ray spectroscopy can measure elemental composition of the specimen.[94] The schematic illustration of secondary and backscattered electrons and x-ray generation from the sample atom is shown in **Figure 4.2**.

4.2. Dynamic light scattering

Dynamic light scattering (DLS) is the most common, widely used characterization technique for size, size distribution, and shapes of nanoparticle in liquid phase. DLS directly measures hydrodynamic quantities such as translational and/or rotational diffusion coefficient, which are related to sizes and shapes. The particles in a liquid medium constantly follow Brownian motion. Therefore, the scattered light intensity fluctuates because of the particle random movement. The fluctuation of the scattered light intensity occurs when a particle moves a significant light wavelength.[95] To analyze the particle motion by light scattering quantitatively, autocorrelation function is a useful tool to be applied to express the fluctuation of the scattered light intensity. The normalized light scattering intensity autocorrelation function, *C(t)*, is expressed below.

$$C(t) \equiv \frac{\{I(t)\, I(0)\}}{\{I(0)\, I(0)\}} = [1 + \alpha[g(q,t)]^2] \qquad \textbf{(4.2)}$$

$$g(q,t) = \exp(-q^2 D t) \qquad \textbf{(4.3)}$$

Here, α is a constant (coherent factor) depending on the experimental setup. Practical α is below 1. For monodispersed particle in liquid phase, the function of *g(q,t)* is a single exponential decay which is dependent on translational self-diffusion coefficient *D*, and scattering wave vector **q**.[96] Scattering wave vector can be obtained from $\mathbf{q} = \mathbf{k_s} - \mathbf{k_i}$ ($\mathbf{k_s}$ and $\mathbf{k_i}$ indicate scattered light wave vector and incident light wave vector, respectively.) The magnitude of scattering wave vector is dependent on the wavelength (λ) of light and scattering angle θ,

$$q = (4\pi/\lambda)\, \sin(\theta/2) \qquad \textbf{(4.4)}$$

The translational self-diffusion coefficient (*D*) for the spherical particles (with radius *R*) in a dilute dispersion is defined by Stokes-Einstein equation.

$$R = k_B T / 6\pi\eta D \qquad \textbf{(4.5)}$$

Here, k_B is the Boltzmann's constant, *T* is in the absolute temperature, η is the viscosity of the liquid medium. Therefore, the radius of dispersed particles can be obtained by DLS technique.[97] In most general cases, the particles are not perfectly spherical. Therefore, the radius obtained from the translational self-diffusion coefficient and Stokes-Einstein equation is termed the hydrodynamic radius. The hydrodynamic radius is different from the actual radius of the particle. The particle shape determines the difference between the hydrodynamic radius and the actual dimension of the particles.

DLS also provides information related to particle size distribution. Nanoparticles have size distribution instead of having one single size. Thus, the particles have different translational self-

diffusion coefficient. A single particle with a self-diffusion coefficient (denoted by *i*) contributes its exponential equation to the whole system,

$$g(t) = \sum_i A_i \exp{(-\Gamma_i t)} \tag{4.6}$$

where $\Gamma_i = q^2 D_i$ is the decay time and A_i is a factor proportional to the ratio of the scattered intensity contributed by particles (*i* denoted particles) with the same dimension. Therefore, the time correlation function is a sum of each exponential. To analyze the equation above, powerful mathematical tool, inverse Laplace transform is used to obtain the distribution function of relaxation times. The continuous summation of **Equation 4.6** is taken.

$$g(t) = \int_0^\infty A(\Gamma)\, exp{(-\Gamma t)}\, d\Gamma \tag{4.7}$$

Here, $A(\Gamma)$ is the distribution function of the decay rate (Γ), $A(\Gamma)\, d\Gamma$ is the fraction of correlation function which decays with relaxation time between Γ and $\Gamma + d\Gamma$. Laplace inversion provides $A(\Gamma)$ value and thus, the distribution of particle sizes can be obtained.[98]

4.3. Fourier-transform infrared spectroscopy

Infrared spectroscopy is a widely used tool for the polymer characterization and provides information on three important features of structure (i) chemical composition, (ii) structure conformation and configuration, and (iii) intermolecular interactions or interatomic forces related to valence bond. The advantages of Fourier transform infrared spectroscopy (FT-IR) are an increase in the signal-to-noise ratio, higher energy efficiency, rapid scanning rate, and large data processing capability.

FT-IR uses Michelson interferometer **(**See in **Figure 4.3)** as an important instrument to improve the sensitivity of spectroscopy, and it is a technique that examines all transmitted energy. It is made up of two mirrors (one is stationary and another is movable, at 90° fixed angle each other) and a beam splitter. The beam splitter divides the source beam into two beams evenly. Reflected one from the splitter travels to the stationary mirror, and the other is transmitted to the movable mirror.

When the reflected and transmitted beam reaches each mirror, they reflect once again to the beam splitter. At the beam splitter, they recombine and interfere. The recombined beam interfere each other constructively and destructively, depending on the path difference and wavelength of the beam. When the stationary and movable mirror has the same distance from the beam splitter, there is no difference on paths. When the path differences equal to integral number of beam wavelength, nλ, the constructive interference of beams can occur. On the other hand, if the movable mirror changes is position and the path length is displaced from the integral number, destructive
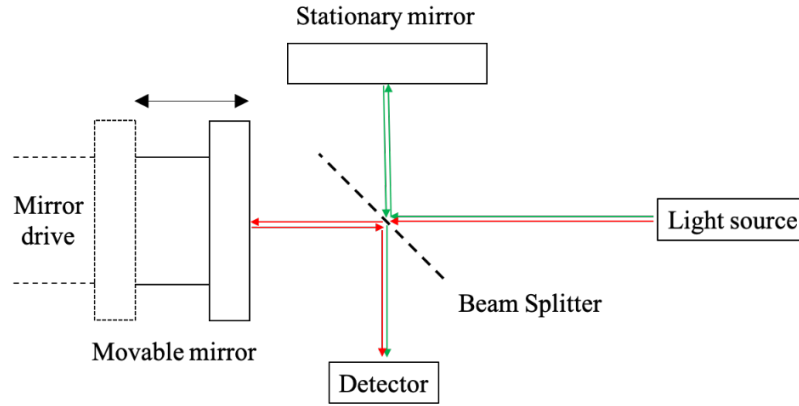
Figure 4.3. Diagram of Michelson interferometer

interference happens and the resulting intensity at the detector dramatically decreases. The relationship between mirror displacement and resulting intensity is obtained by the equation below.

$$I(x) = 2RTI(v)(1 + cos\, 2\pi\, vx), \tag{4.8}$$

where *R, T* is the reflectance and transmission of the splitter, respectively. *I(v)* is the incident intensity which is called interferogram at frequency *v*. *x* is the path difference varied by moving the mirror. Usually, transmittance and reflectance are 0.5 each, thus, the equation is written below,

$$I(x) = 0.5\, I(v)(1 + cos\, 2\pi\, vx) \tag{4.9}$$

$I(x)$ is composed of constant $0.5\, I(v)$ and modulating $0.5\, I(v) \cdot cos\, 2\pi\, vx$ parts which is called interferogram. In case of continuous polychromic sources $I(v)$, interferogram is the integral of whole individual interferogram from each frequency,

$$I'(x) = \ 0.5 \int_{-\infty}^{+\infty} I(v) \cdot\ cos\, 2\pi vx\ dv \tag{4.10}$$

The detected amplitude of the interferogram is amplified based on source intensity or/and instrument properties. Therefore, it can be expressed,

$$I'(x) = \int_{-\infty}^{+\infty} B(v) \cdot\ cos\, 2\pi vx\ dv, \tag{4.11}$$

where $B(v)$ is the initial intensity of the source at frequency v, also considered as instrument characteristics. From the Fourier transform,

$$B(v) = \int_{-\infty}^{+\infty} I'(x) \cdot\ cos\, 2\pi vx\ dx \tag{4.12}$$

is obtained. For the data acquisition, it involves signal averaging and accumulation of the interferogram. Therefore, monochromatic source interferogram is measured with the main interferogram together. In case of different interferogram, it can be acquired at exact same position by taking the zero value from the reference interferogram.[99, 100]

As stated, an interferogram is obtained by adding a large number of sinusoidal waves together. Each of added sinusoidal waves has its own information such as given infrared peak wavenumber and amplitude of the peak intensity at that wavenumber. The infrared spectrum is calculated from the summed sinusoidal signals in the interferogram by Fourier transform.

When Fourier transform is performed for an interferogram, a single beam spectrum is obtained. The spectrum is a plot of the detected signal as a function of wavenumber. A measured spectrum without a sample is called a background spectrum. The background spectrum comes from the contributions of the instrument and environment to the infrared spectrum. The infrared spectrum of the sample looks similar to the background spectrum. Therefore, the sample spectrum should be compared with the background spectrum to remove the contributions of instrument and environment and results in a transmittance spectrum.

$$\%T = I \,/\, I_0 \tag{4.13}$$

where $\%T$ is transmittance. I and I_0 indicates the measured intensity with/without sample, respectively. In addition to this, the absorbance spectrum can be calculated from the transmittance equation,

$$A = - log\ T. \tag{4.14}$$

Here, A is the absorbance. The final spectrum obtained from **Equation 4.14**, has only information only about the sample. For qualitative analysis of a sample, absorbance and transmission both can be used. In contrast, for quantitative analysis, only absorbance can be used.[101]

4.4. Modulated Differential scanning calorimetry

Differential scanning calorimetry (DSC) is an invaluable physical and physico-chemical method of thermal analysis for polymer science. DSC provides thermal characteristic information of polymer materials such as glass transition, melting, and degree of crystallinity. DSC is based on heating (or cooling) a reference and a sample with the same rate, which keeps both temperatures the same and measure and the heat flux is measured for the same temperature of the sample and the reference.[102]

As shown in **Figure 4.4**, DSC has two chambers for a reference and a sample. Each sample is heated by a single heating source, and the sensitive transmitter measures the temperature of both

sides. The temperature difference between T_S and T_R is measured by a function of heating or temperature change, and it is related to the change of enthalpy H, heat capacity C, and thermal resistance R of the sample.[103]
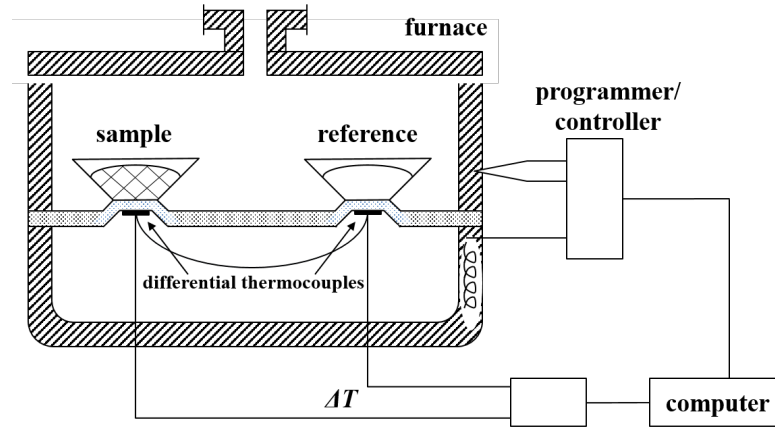

Figure 4.4. A scheme of experimental heat-flux DSC setup. (Redrawn according to Ref.[103])

The heat adsorption of the sample per unit time dH/dt is expressed by,

$$\frac{dH}{dt} = -\frac{dq}{dt} + (C_S - C_R)\frac{dT}{dt} - RC_S\frac{d^2q}{dt^2},\qquad(4.15)$$

where dq/dt is the measured heat reflux as DSC curves (marked **I** in **Figure 4.5**), $(C_S\text{-}C_R)\,dT/dt$ is a term for the gap between the baseline and zero line (marked **II** in **Figure 4.5**). C_S and C_R are the heat capacities of the sample and the reference, respectively. dT/dt is the change rate of the heater temperature. The final term, $RC_S\,d^2q/dt^2$ is the slope of the curve at any temperature (marked **RC** and **III** in **Figure 4.5**). The total heal flux of calculated by DSC plot is equal to the total enthalpy change of the sample. The **Equation 4.15** on a DSC curve is illustrated in **Figure 4.5**.[104]

Modulated differential scanning calorimetry (MDSC) is one of the extended applications of DSC, which usually uses modulated linear or isothermal heating and cooling. The result of MDSC is analyzed mathematically to obtain valuable meaning from the calorimetric response to the underlying temperature profile. The temperature program modulates the instrument heating or cooling behavior by small perturbation, but the trend of heating or cooling seems a conventional constant temperature increase with time. The simplest expression for the temperature increase is shown below,

$$T = T_o + bt + A\sin(\omega t),\qquad(4.16)$$

where T_0 is the initial temperature, b is the underlying heating (or cooling) rate, A and ω are the
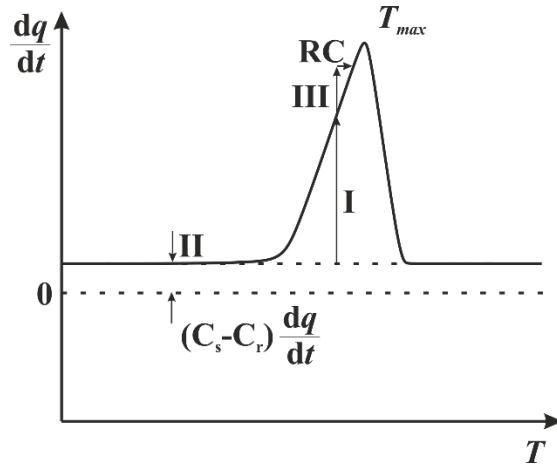
Figure 4.5. A representative of **Equation 4.15** on DSC curve. (Redrawn from Ref. [104])

amplitude and frequency of the temperature fluctuation. The adsorption energy of the sample, dH/dt, can be expressed,

$$\frac{\mathrm{d}H}{\mathrm{d}t} = C(b + A\omega\ \cos(\omega t)) + B\ \sin(\omega t) + f'(t,T),\qquad\qquad\textbf{(4.17)}$$

where C is the thermodynamic heat capacity, $f'(t,T)$ is the average kinetic function when sine modulation effect is eliminated. B is the kinetic response amplitude related to sine modulation. $(b + A\omega\ \cos(\omega t))$ is quantity of measured dT/dt. From **Equation 4.17**, heat flow contains cyclic term which is effected by A, B, and ω.[105]

MDSC offers good temperature resolution of slow heating rate and the higher output data based on linear, cyclic heating, and the faster oscillations and it gives all the thermal analysis information which can be obtained from conventional DSC as well. MDSC is more appropriate thermal analysis method for polymer materials.

Chapter 5. Brillouin Light Scattering Spectroscopy

Mechanical properties of colloids were characterized by Brillouin Light Scattering (BLS) spectroscopy. BLS has been widely used for the research of vibrational properties of particles in submicron scale. BLS spectroscopy is a non-destructive and non-contact technique utilizing inelastic scattering of monochromatic light by thermally populated GHz phonons. The scattering wave vector **q** is defined as $\pm$**q** = **k$_s$** - **k$_i$**, where **k$_s$, k$_i$** are wave vectors of scattered and incident light, respectively.

5.1. Principles of BLS

To understand the principles of BLS, it would be easy to consider constructive interference between multiply reflected light by sound waves. **Figure 5.1** illustrated an acoustic plane waves with a wavelength Λ propagating in opposite directions. The sound wave modulates the medium density periodically, thus the refractive index *n* and the dielectric constant.
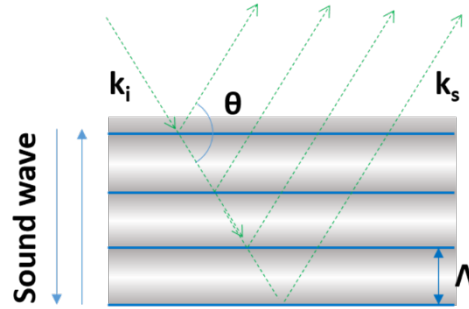
Figure 5.1. A scheme of a constructive interference of incident and reflection light, and a plane wave propagates with wave number of Λ.

The incident light scatters multiple times by the periodic in-phase front of the sound wave and forms constructive interference expressed by the Bragg's condition,

$$\lambda = 2n\Lambda \sin(\theta/2), \tag{5.1}$$

where, λ is the wavelength of the incident light, *n* is the refractive index of the sample medium, Λ is the wavelength of soundwave and θ is the angle between incident and scattered beam.

The scattering wave vector **q** is defined as the difference of incident light wave vector (**k$_i$**) and scattered light wave vector (**k$_s$**), ($\pm$**q** = **k$_s$** - **k$_i$**). The magnitude of scattering wave vector **q** can be obtained from the formula:

$$q^2 = |\mathbf{q}|^2 = k_i^2 + k_s^2 - 2k_i k_s = 2k_i^2(1 - \cos\theta) = 4k_i^2 \sin^2\frac{\theta}{2}. \tag{5.2}$$

With the $k_s = k_i = 2\pi n/\lambda$,

$$q = 2k_i \sin\frac{\theta}{2} = \frac{4\pi n}{\lambda}\sin\frac{\theta}{2} \tag{5.3}$$

From **Equations 5.2 and 5.3** we obtain:

$$q = \frac{4\pi n}{\lambda}\sin\frac{\theta}{2} = \frac{2\pi}{\Lambda} \tag{5.4}$$

This means that the scattering wave vector **q** is equal to the sound wave vector **k** ($k = 2\pi / \Lambda$). By simply changing θ, specific **q** can be chosen.

Because of inelastic scattering of photons, the angular frequency of incident photon (ω_i) is changed (frequency shift) to scattered photon frequency (ω_s). In addition, during inelastic scattering process, phonons can be created (Stokes process) or annihilated (anti-Stokes process). Therefore, the angular frequency shift of scattered photons is equal to angular frequency of the phonons.

$$\omega_{phonon} = |\omega| = \omega_s - \omega_i, \tag{5.5}$$

which is connected to acoustic wave phase velocity c, and the phonon wavelength Λ.

$$\omega_{phonon} = \omega = \frac{2\pi c}{\Lambda} \tag{5.6}$$

The phonon frequency can be calculated from the **Equation 5.6** as $f = \omega/2\pi$,

$$f_s = f_i \pm \frac{cq}{2\pi} = f_i \pm \frac{c}{2\pi}\frac{4\pi n}{\lambda}\sin\frac{\theta}{2}. \tag{5.7}$$

Here, plus and minus correspond to the anti-Stokes and Stokes process, respectively. Therefore, BLS gives the results with symmetric doublet centered at the elastic frequency (Rayleigh scattering) at frequencies $f = \pm cq/2\pi$.

5.2. Tandem Fabry-Perot interferometer

The multipass tandem Fabry-Perot (FP) interferometer was introduced in 1980 to provide the highest contrast, resolution, and free spectral range for BLS. This system has two interferometers (FP1 and FP2) in series having slightly different mirror space. The transmission plots of interferometer FP1, FP2, and tandem as a function of wavelength are shown in **Figure 5.2**.

The transmitted wavelength of each FB follows the equations:

$$\lambda_1 = 2d_1/P_1 \quad \text{for FP1} \quad \text{and} \quad \lambda_2 = 2d_2/P_2 \quad \text{for FP2}, \tag{5.8}$$

where d is the mirror spacing of each FP and P is an integer. These equations (**Equation 5.8**) imply that the transmitted wavelength through both FP interferometers will be,

$$\frac{d_1}{d_2} = \frac{P_1}{P_2}. \tag{5.9}$$

To observe transmitted wavelength through two FP interferometer with high resolution, the ratio of mirror spacing in FP1 and FP2 should remain constant and same to P_1/P_2:

$$\frac{\Delta d_1}{\Delta d_2} = \frac{d_1}{d_2} = \frac{P_1}{P_2}. \tag{5.10}$$

Therefore, the ambiguous mirror spacing ratio of FP1 to FP2 is an obstacle to the practical use of the tandem FP interferometer. The obstacle was overcome by introducing a novel design of the
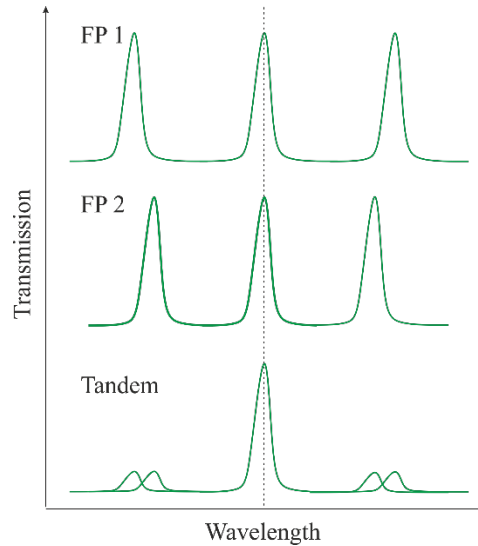
Figure 5.2. Transmission curves from Fabry-Perot interferometer 1 and 2, suppressed higher order transmission from Tandem Fabry-Perot interferometer.

scanning stages as illustrated in **Figure 5.3.** The first interferometer FP1 is installed in the direction of the movement of a translational stage. One mirror of FP1 is mounted at an angular orientation device which allows a small movement for transmission adjustment and the other lies on the translation stage. The second interferometer FP2 is installed with an axis at the angle θ to the direction of translation stage movement. One mirror sits on the translational stage, the other is mounted at the angular orientation device.

While the translation stage move from left to right to change the mirror spacing of FP1 and FP2, the mirror spacing ratio of FP1 to FP2 (d_1, d_2) is simultaneously adjusted as d_1 and $d_1 \cos \theta \, (= d_2)$.
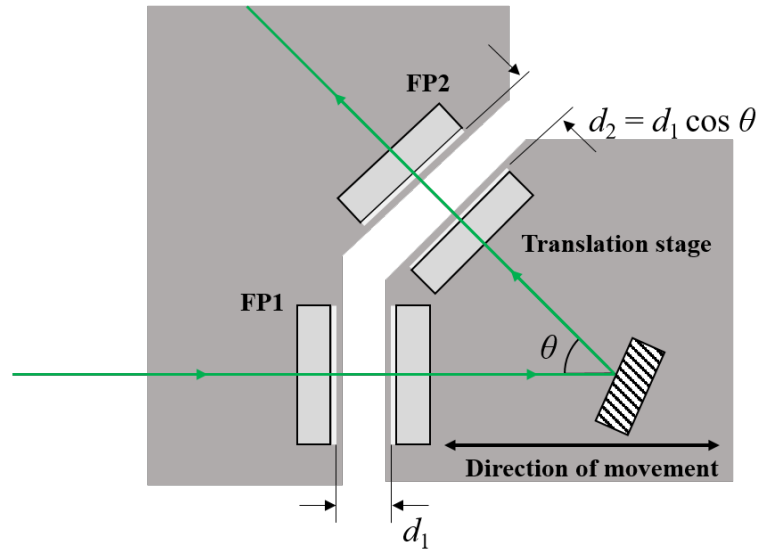
Figure. 5.3. The translation stage which allows simultaneous synchronization of mirror spacing ratio of FP1 to FP2.

5.3. Experimental setup

The experimental setup for BLS is shown in **Figure 5.4**. It is made up of single mode laser ($\lambda = 532$ nm) which is mounted on a rotatable goniometer, a sample holder equipped with a heater and a temperature indicator, and a six-pass tandem Fabry-Perot interferometer. The scattering angle θ which determines the scattering wave vector **q** can be changed from 0° to 160°. The sample holder equipped with electric heater, water cooler and temperature indicator allows the temperature-dependent experiment from 278K to 453 K. This function is important to study on thermal characterization of materials such as glass transition temperature of the polymer samples.

Figure 5.4. A scheme of the experimental BLS setup. The figure is from the original reference [106].

As illustrated in **Figure 5.5**, the sample holder is a cylinder type structure made out of metal. The flat slit in the middle of the cylinder, allows all beams (incident, transmitted, scattered, and reflected) to go through the sample. For te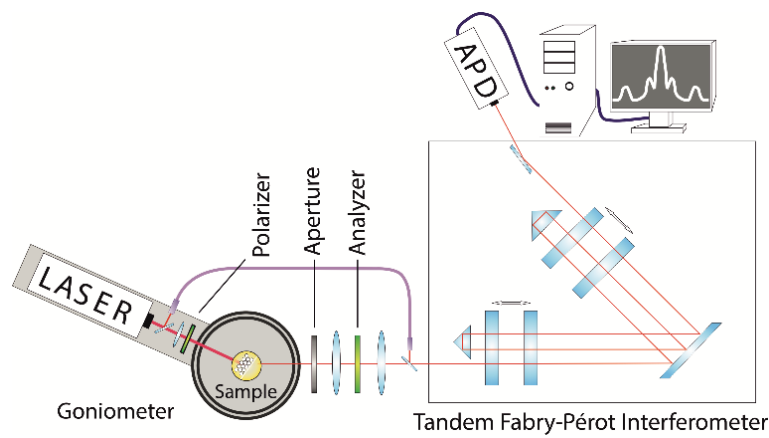mperature resolved experiments, an additional cylinder-shape quartz wall inserted inside of the metallic body to make a room for the sample as a closed system for temperature control. The outside of the quartz wall perfectly fits the inside of the metal body. A special adapter allows the sample to be brought to the proper height for the measurement. The whole sample holder is mounted on a movable stage which can be adjusted position in X and Y-axis on a stable table where BLS is installed. An electric heater and a Pt100 temperature indicator are installed inside of the metal body to control the heating condition. A water cooler is connected to the metal body offer cooling condition for the sample. An additional Pt100 temperature sensor is put inside the sample room close to the sample to check the real sample temperature. The temperature is stabilized within ± 0.2 K and controlled from 278 K to 453K with the water cooler and the heater.
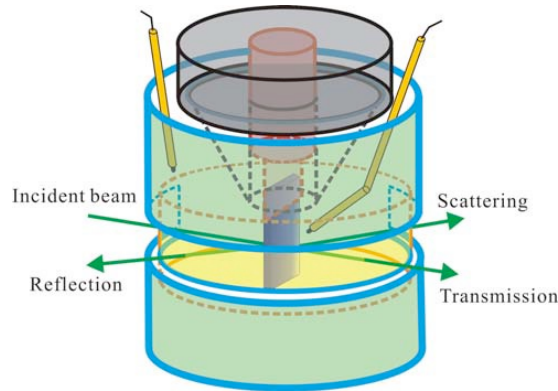
Figure 5.5. The temperature controllable sample holder for BLS. The figure is from the original reference [107].

5.4. Scattering geometries

Most experiments reported in the thesis were performed for colloidal films on a flat substrate. There are three different BLS geometries suitable for such samples: transmission, reflection, and backscattering geometry (see **Figure 5.6**). As transmission geometry illustrated in **Figure 5.6a**, The incident light go through the film, the scattered light is on the opposite side of the incident light. The magnitude of the scattering wave vector **q** in the transmission geometry is given by the formula:

$$q = \frac{4\pi n}{\lambda} \sin\left[\frac{1}{2}\left(\sin^{-1}\left(\frac{1}{n}\sin(\theta - \alpha)\right) + \sin^{-1}\left(\frac{1}{n}\sin\alpha\right)\right)\right], \tag{5.11}$$

where θ is the angle between the transmission and scattering light and α indicates the angle of the incident beam. n indicates the refractive index of the sample. λ is the wavelength of the incident light. The scattering wave vector is parallel to the film so that the equation simplifies to:

$$q_{parallel} = q_\parallel = \frac{2\pi}{\lambda} (\sin\alpha + \sin(\theta - \alpha)). \qquad (5.12)$$

Further, for $\theta = 2\alpha$, it transforms to:

$$q_\parallel = \frac{4\pi}{\lambda} \sin\frac{\theta}{2}. \qquad (5.13)$$

The above formula is useful and applicable for almost all experiments performed in the thesis. Also, it facilitates the wave vector **q** calculation without refractive index consideration. Therefore, all materials that allow light to go through can be characterized by this geometry.

In the case of the reflection geometry, the magnitude of **q** is defined as:

$$q = \frac{4\pi n}{\lambda} \cos\left[\frac{1}{2}\left(\sin^{-1}\left(\frac{1}{n}\sin(\theta - \alpha)\right) + \sin^{-1}\left(\frac{1}{n}\sin\alpha\right)\right)\right]. \qquad (5.14)$$

For special reflection case of $\alpha = \frac{180^o - \theta}{2}$, the wave vector **q** is the same to its component perpendicular to the film in **Figure 5.6b**. With this geometry, the refractive index of the sample should be considered for wave vector **q** calculation.

Transmission and reflection geometries for a given angle cannot be characterized selectively. Therefore, it should be carefully considered that which geometry is good for the experimental goal. The reflection geometry is usually used for the study on phonon propagation along the normal of film.

For backscattering geometry (**Figure 5.6c**), the scattering angle is 180° ($\theta = 180°$) to incident laser and scattering wave vector **q** lies in the same direction as **k$_s$**. Therefore, the magnitude of the wave vector in this geometry is given by:

$$q = \frac{4\pi n}{\lambda}. \qquad (5.15)$$

The **Equation 5.15** means the scattering vector, **q**, in the backscattering geometry is independent of the angle in the case of elastically isotropic samples.[108]

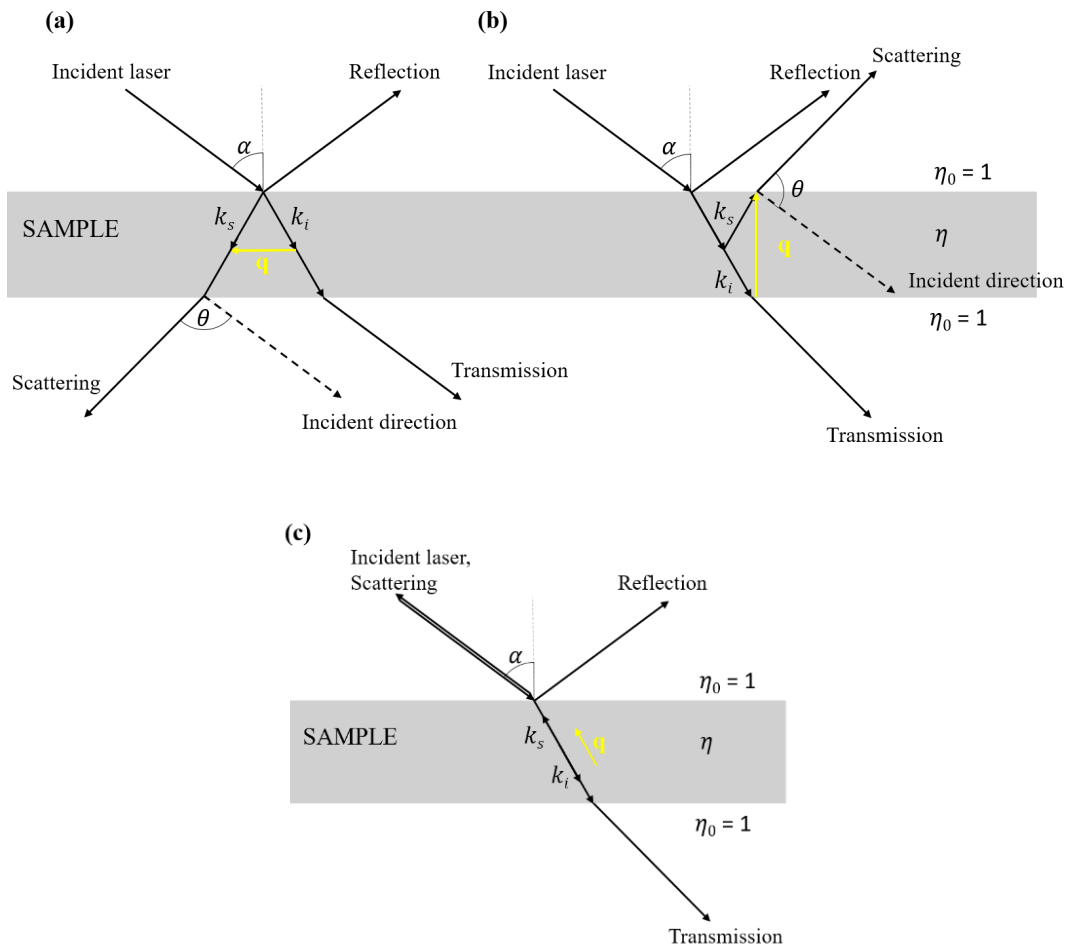**Figure 5.6**. Scattering geometries of BLS for a sample film **(a)** transmission geometry, **(b)** reflection geometry, and **(c)** backscattering geometry.

Chapter 6. Results and Discussion

6.1. Direct observation of polymer surface mobility via nanoparticle vibrations

Measuring polymer surface dynamics remains a formidable challenge of critical importance to applications ranging from pressure sensitive adhesives to nanopatterning, where interfacial mobility is key to performance. Here, we introduce a unique metrology of Brillouin light spectroscopy to reveal polymer surface mobility *via* nanoparticle vibrations using polystyrene as a model system. By measuring the temperature-dependent vibrational modes of polystyrene nanoparticles, we identify the glass transition temperature (T_g) and calculate the elastic modulus of individual nanoparticles as a function of particle size and chemistry. Evidence of surface mobility is inferred from the first observation of a softening temperature T_s, where the temperature-dependence of the fundamental vibrational frequency of the nanoparticles reverses slope below T_g. Beyond the fundamental vibrational modes given by the shape and elasticity of the nanoparticles, a new mode, termed the "interaction induced mode", was found to be related to the active particle-particle adhesion and dependent on the thermal behavior of individual nanoparticles.

6.1.1. Introduction

Polymer nanoparticles (NPs) are useful materials with applications in drug delivery, [1,109,110] surface coating [2,111] and assembly of photonic[112–114] and phononic materials.[115,116] Optimizing NPs for these applications requires an understanding of their physical properties, including the glass transition temperature (T_g) and elastic modulus. However, values of such properties may differ at the nanoscale from the bulk. Prior studies of confined polymers have revealed that thin films exhibit T_g values that are different from the bulk, and that this phenomenon was dependent on interfacial effects, i.e., the surrounding environment. Keddie *et al.* reported a T_g reduction of polystyrene (PS) thin films supported on silicon substrates with decreasing film thickness *via* ellipsometry.[5,117,118] In contrast, they reported a T_g increase for poly(methyl methacrylate) (PMMA) thin films when supported on the same substrate with decreasing film thickness. Since theses original investigations, the influence of confinement and interfacial effects on T_g of polymer thin films have been confirmed by varioius methods including fluorescence spectroscopy,[119] dielectric relaxation spectroscopy (DRS),[120] dynamic mechanical analysis (DMA),[121] and Brillouin light scattering (BLS).[122,123] Of particular importance, there is now growing evidence for the existence of a mobile layer at the surface of thin films , which plays a crucial role in the observed deviations in T_g with confinement.[6,119,124–127]

Motivated by the increased use of polymer nanoparticles in technology and the scientific pursuit of uncovering a generality of confinement effects on T_g, irrespective of sample geometry, there has been recent interest in using nanoparticles as model systems.[128,129] Ediger and coworkers,[130] reported a broadening of T_g and a suppression in heat capacity change, ΔC_p, at the glass transition with decreasing diameter for PS NPs stabilized with surfactants when suspended in an aqueous environment. Priestley and coworkers,[4] reported a reduction in T_g of PS NPs with decreasing diameter. In their investigation, the nanoparticles where stabilized without the use of surfactants. Later, Zhu and coworkers[7] confirmed that the suppression in T_g of PS NPs with decreasing diameter was dependent on the presence (or lack) of surfactants (and surfactant type) at the nanoparticle interface. These findings, corroborated by Christie *et al.*,[8] supported the notion that interfacial effects strongly influenced the glassy dynamics of confined polymers, including for PS NPs.

The leading argument for the observed confinement effects on the T_g of PS NPs is associated with the existence a polymer surface layer that is more mobile than the bulk-like core.[4,7,130] Current techniques, e.g., differential scanning calorimetry, are limited to measuring T_g of samples containing millions of NPs and cannot resolve the T_g of a single NP. Moreover, because of the difficulty in characterizing the T_g individual polymer NPs, and its segmental dynamics, the mobility at the surface of NPs has yet to be demonstrated. Hence, there remains a challenge to develop a technique that is capable of measuring the T_g of individual polymer NPs and to provide direct evidence of surface mobility for these confined systems.

Penciu *et al.*[131] and Kuok *et al.*[132] first applied BLS to measure the eigenfrequencies of giant micelles and silica NPs of submicrometer size. For NPs with a diamater less than 100 nm, Raman scattering and pump probe techniques could be applied, however, fewer modes were resolved.[133–137] Recently, particle vibration spectroscopy by means of BLS has been advanced to measure particle eigenfrequencies with different architectures to determine the mechanical properties of polymer NPs.[138–140] For homogeneous spherical particles of diameter *d*, the lowest frequency BLS active mode is the (s,1,2) spheroidal (s) vibration. Its frequency is given by the Lamb expression:

$$f(\text{s},1,2) = Ac_t d^{-1} \tag{6.1.1}$$

where A is a dimensionless quantity that depends on the ratio between the transverse c_t and longitudinal c_l sound velocities in the particle.[11,140,141] The first attempt was to use **Equation 6.1.1**, together with a model for the calculation of the Brillouin intensity, for assigning the observed peaks to the modes of an isolated NP.[140,142,143] Later, it was recognized that particle-particle interactions in clusters of NPs could influence the eigenfrequencies of individual NPs and lead to a low frequency broad band, which was attributed to the propagation of longitudinal waves.[144,145]

Here, in an effort to advance the current state-of-the-art, we demonstrate that BLS yields information on the elastic properties of individual NPs while also accounting for the presence of interparticle interactions, which leads to a blue shift and splitting of the (s,1,2) mode. With the aid of a simple finite element method (FEM) model of a crystal of interacting spheres, it is possible to consider the separate contributions of these two effects. Based on this approach, we used BLS to measure the T_g of PS NPs and to specify the mobile layer driven NP interactions. The experiments allowed us to observe the vibrational modes of cluster of polymer NPs whose frequencies changed depending on the interactions among the NPs. [136,137,145–147] The T_g of the PS NPs was measured by the temperature-dependence of the vibrational modes. The enhanced mobility of polymeric chains on the surface layer caused as sudden increase in interparticle adhesion identified by a blue shift of the fundamental mode (s,1,2) and the low frequency interaction induced (s,1,1) broad band. Consequently, we demonstrate that measuring the temperature-dependence of the eigenfrequencies is a new powerful tool for studying the glass transition behavior of PS under three-dimensional confinement and provides strong evidence for the presence of mobile surface layer mobility for PS NPs. The method can be extended to any polymer-based NP with submicrometer size.

6.1.2. Results

Particle Vibration Spectrum

Figure 6.1.1a shows the room temperature BLS spectra of clusters of PS NPs with three different diameters, d = 141, 202, and 707 nm referred to as PS$_A$-141, PS$_B$-202, and PS$_A$-707, respectively. The subscript A and B indicate different emulsion polymerization conditions (A and B stand for sodium 4-vinylbenzyl sulfonate and acrylic acid chemistry; see details in Methods). The BLS spectra are plotted as scattered light intensity I against the scaled frequency $f \cdot d$, where f refers to the frequency. This presentation accounts for the $f \sim d^{-1}$ dependence of the eigenfrequencies of an isolated NP and further provides an adequate comparison of the shapes of (s,n,l) bands, where the label denotes the radial (*n*) and angular (*l*) dependence of the displacement for the spheroidal modes (s). For PS$_A$-707, the (s,1,2) mode is a single peak represented by a Lorentzian line shape. For the smaller NPs, PS$_A$ and PS$_B$, the (s,1,2) peaks clearly deviate from a single line shape which can be phenomenologically reproduced by two Lorentzian curves. The peak positions are different in all spectra, indicating that the mechanical properties of the materials and/or the effect of the interactions among particles are different.

Figure 6.1.1b shows the scaled frequencies ($f \cdot d$) of the experimental (s,1,2) peaks taken at the intensity maximum. Also included in **Figure 6.1.1b** are results of PS NPs taken from previously reported data.[145,148] The data are grouped into three $f \cdot d$ regions. Sample PS$_B$-202, PS$_B$-190 and

literature PS NPs all fall in the intermediate region, $f(s,1,2) \cdot d = 1030 \pm 30$ GHz $\cdot$ nm (or m/s). If we insert these values into **Equation 6.1.1** for homogeneous spheres,[148] the transverse sound velocity within these PS NPs is calculated to be $c_t = 1220 \pm 35$ m/s, which agrees with the corresponding, $c_t = 1210 \pm 20$ m/s value of the bulk PS.[140] In the case of PS_A-707 for which the (s,1,2) peak is well represented by a single Lorentzian, $f(s,1,2) \cdot d = 900 \pm 10$ m/s, and hence $c_t = 1070$ m/s. Notably this value is about 10% lower than the $c_t = 1180 \pm 15$ m/s measured in the corresponding contiguous film prepared by annealing the PS_A-707 NPs at 400K. Therefore, the shear modulus $G = \rho c_t^2$ (ρ refers to the mass density, 1050 kg/m^3 for PS) of the PS_A-707 NP is ~ 20 % lower than that of the bulk.
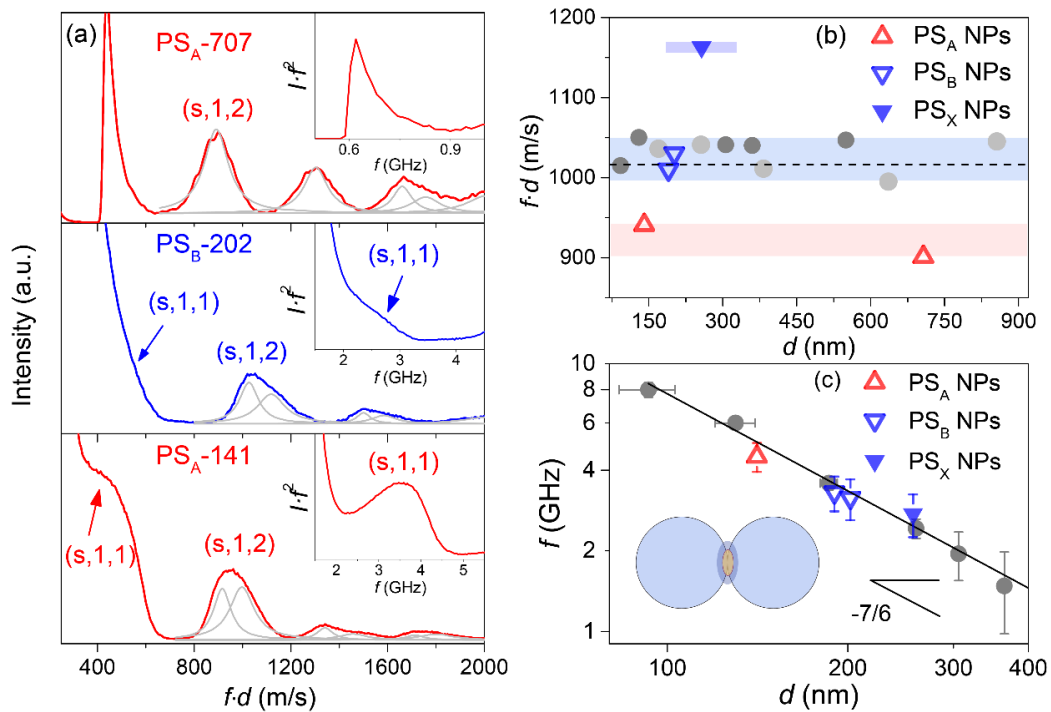
Figure 6.1.1. (a) Brillouin light scattering (BLS) spectra *(I vs. $f \cdot d$)* for three PS spherical particles with diameter, $d = 141$, 202, and 707 nm. The interaction induced mode (s,1,1) (arrows) and the fundamental mode (s,1,2) are indicated in the plot. The gray solid lines denote the representation of the peak with either single or double Lorentzian lines. Inset: Reduced spectra $I \cdot f^2$ vs. f **(b)** $f(s,1,2) \cdot d$ vs. d and **(c)** $f(s,1,1)$ vs. d for PS_A (red open triangles) and PS_B (blue open inverse triangles) nanoparticles obtained from the cutoff frequency at 20 % of the maximum intensity. Blue filed inverse circles in **(b)** and **(c)** denote the crosslinked PS_X NPs with $d = 257$ nm. The dashed line in **(b)** denotes the scaled frequency based on bulk PS elastic moduli. Closed gray and black circles in **(b)** and **(c)** are exported from references. [145,149] Blue and red filled are in **(b)** indicate distinctive scaled $f(s,1,2)$ groups of PS_A and PS_B, respectively. In **(c)**, linear gray line in indicates the scaling law $f(s,1,1) \propto d^{-7/6}$ derived by Johnson-Kendall-Roberts model. Inset schematically illustrates an interparticle adhesion activating the (s,1,1) mode.[12]

For the PS_A-141, the frequency at the peak maximum leads to $f(s,1,2) \cdot d = 960 \pm 15$ m/s, which is slightly higher than the scaled frequency of PS_A-707. For both PS_A particles, however, $f(s,1,2) \cdot d$ clearly falls below the value for all other PS NP's shown in **Figure 6.1.1b**. For the latter, c_t compares well with the bulk PS value also assumed by the contiguous films of all PS NPs. We attributed the reduced elastic modulus of both PS_A-141 and PS_A-707 colloidal film to the different emulsion polymerization procedures; PS_B-190 and PS_B-202 were synthesized using a acrylic acid comonomer (PS_B), whereas PS_A-141 and PS_A-707 were synthesized in the presence of sodium 4-vinylbenzyl sulfonate (PS_A) (see Methods section). The scaled frequency of the two PS_B NPs (inverse blue triangles in **Figure 6.1.1b**) is comparable to those of previously reported PS NPs because of the same chemical composition.[145,148] Importantly, this elasticity disparity implies spatial confinement induced effects which are erased in the corresponding bulk films. This association to physical confinement is further supported by an additional NP, PS_X-257 formed with crosslinked (subscript X) polymer networks. The scaled f(s,1,2) value marked at $f(s,1,2) \cdot d = 1,200$ m/s in **Figure 6.1.1b**, reflects larger elastic modulus than the corresponding contiguous bulk film.

In **Figure 6.1.1a**, nanocolloid films composed of smaller particles, PS_A-141 and PS_B-202 (and PS_X-257 which will be discussed later), show two major spectral differences compared to bigger PS_A-707: first, there is the appearance of the frequency peak below f(s,1,2), better visible in the inset of **Figure 6.1.1a**, and second peaks split (gray solid lines in **Figure 6.1.1a**. Both effects are due to the adhesion among neighboring NPs. **Figure 6.1.1c** reports the f(s,1,1) of the low frequency interaction induced (s,1,1) mode for all PS NPs investigated. The reported f(s,1,1) are those of the high frequency cutoff in a $I \cdot f^2$ plot at 20% of the peak intensity owing to the nature of this interaction-induced mode.[145] These two differences are relates to the sound propagation of longitudinal phonons in a cluster of NPs; hence, it will not be present if the interactions among the particles are switched-off. Its mode pattern corresponds to the pure translation of the sphere, i.e., the (s,1,1) mode with zero frequency in the free sphere.[144] All exchanged wave vectors $\boldsymbol{q}$, with their magnitude $0 < q < q_{bs}$ (with the bs meaning back-scattering) contribute to this peak, which resembles the density of vibrational states (DOS) of the longitudinal branch (s,1,1,l). The reduced intensity $I \cdot f^2$ relates only to $\rho(f) \cdot C(f,\boldsymbol{q})$, where $\rho(f)$ is the DOS and $C(f,\boldsymbol{q})$ is the coupling coefficient that accounts for the BLS activity *via* the elimination of the thermal contribution $\frac{n(\omega,T)+1}{\omega} \sim \frac{1}{\omega^2}$ for $k_B T \gg \hbar\omega$ (where $n(\omega,T)$ is the Bose-Einstein factor) and $\omega = 2\pi f$. In addition, $I \cdot f^2$ allows a better resolution of the peak from the elastic scattering (Rayleigh line). The (s,1,1) mode was observed for the first time by Mattarelli *et al.*[145] for PS, and later reported for silica[136] and semiconductor[137] NPs. Longitudinal acoustic phonons of an *fcc* crystal of spherical particles have a cutoff frequency, $f(s,1,1) \sim \sqrt{K_{eff}/M}$ governed by the effective constant K_{eff} of spring between neighboring NPs of mass M. According to the Johnson-Kendall-Roberts (JKR) model,[150] the scaling relation, $f(s,1,1) \propto d^{-7/6}$ (see Methods), well reproduces the experimental

40

f(s,1,1) for the present and reported PS NPs,[145] as shown in **Figure 6.1.1c**. In the case of PS_A-707, the (s,1,1) mode is not resolved because of its low frequency (extrapolation of the scaling in **Figure 6.1.1c**. Hence, the peak is obscured by the central Rayleigh peak (inset to **Figure 6.1.1a**).

A comparison of the data in **Figure 6.1.1b** and **Figure 6.1.1c** shows that the frequencies of the (s,1,1) and (s,1,2) vibrations have different dependence on the strength of the interaction among the NPs and on the rigidity of the NPs. The latter has an important effect on the frequencies of the (s,1,2) mode, which discriminates three groups for the PS_A, PS_B, and PS_X. The size of the NPs, which determines the strength of the interaction, plays a minor role. On the contrary, the frequencies of the (s,1,1) modes are governed by the strength of the interaction, $K_{eff} \propto d^{2/3}$. The fact that the NP vibration dynamics strongly depend on the particle mechanics, whereas the sound propagation in the colloidal film strongly depends on the strength of the interaction among the NPs, suggests a method for disentangling the consequences on the frequency shift of the (s,1,2) mode of the isolated NPs. Softening of the PS NPs, with respect to bulk PS, will cause a red shift of the vibrational frequencies, while the presence of interactions will produce a blue shift of all frequencies compared to that of isolated NPs. The shift is accompanied by a broadening, since the interaction transforms the discrete spectrum of a free particle into phonon bands with finite dispersion.

These two effects are simulated by a simple model based on a FEM calculation of a fcc crystal of nearly spherical particles. The particles were obtained by cutting spheres to have a circle of radius a_0, as contact area among them. The strength of the interaction could be affected by changing a_0, as proposed by Saviot et al.[151] for the study of dimers. The interaction energy is proportional to the area and to the surface (adhesion) energy and produces a nearly constant attractive pressure on the contact area. At the equilibrium, these attractive forces are compensated by the repulsion due to the elastic deformation (See detail in chapter 4.1.5. Supporting information). **Figure 6.1.2a** shows the dispersion curves along the [100] direction of the lowest frequency phonons calculated for PS NP with d=141 nm using $a_0 = 14$ nm, $c_l = 2350$ m/s, and $c_t = 1210$ m/s. We focused on the longitudinal (s,1,1,l) and the five branches originating in the (s,1,2) mode possessing significant BLS activity (red solid lines in **Figure 6.1.2a**). The longitudinal and transverse sound velocities in the NP colloidal crystal are estimated from the low q linear dispersion regime of the (s,1,1) mode and are expectedly much lower ($c_l^{fcc} = 1270$ m/s and $c_t^{fcc} = 810$ m/s) than in PS NPs.[137,138]. For non-interacting NPs, f(s,1,1) is zero (lower arrow on the right axis of **Figure 6.1.2a**. The five (s,1,2) branches (two degenerated) extend in a frequency region between about 7.4 to 9.1 GHz. All these frequencies are higher than f(s,1,2) = 7.23 GHz (upper arrow on the right axis of **Figure 6.1.2a**), calculated for the free PS sphere using the same bulk c_l and c_t values. This occurs for all phonon bands since any constraint to the free motions occurring at the interface between the particles increases the vibrational frequencies.
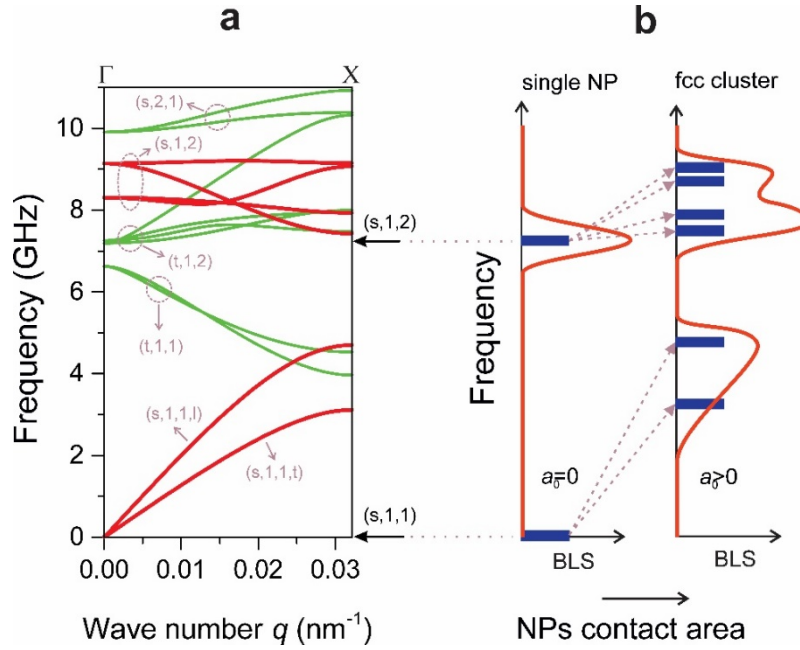
Figure 6.1.2. (color online) Particles interaction induced phonon dispersion, blue-shift and splitting of the modes. **(a)** Calculated phonon dispersion (Γ-X) of a fcc cluster made of cut spheres with diameter $d = 141$ nm and contact area of radius $a_0 = 14$ nm, constituted by homogeneous polystyrene material ($c_l = 2350$ m/s and $c_t = 1210$ m/s). The Brillouin active branches deriving from the (s,1,1) and (s,1,2) of the single sphere are marked with red solid lines. The weakly and non-active branches deriving from (s,2,1) and the torsional modes, respectively, are indicated with green solid lines. The arrows on the right axis indicate the frequencies of the Brillouin active modes of the single particle. **(b)** Schematic diagram of Brillouin spectra for single particle (a_0=0) and fcc cluster (a_0>0), based on the dispersion in **(a)**.[12]

Figure 6.1.2b illustrates the impact of interactions among NPs on the BLS active modes. For an isolated sphere ($a_0 = 0$) only a single Brillouin peak corresponding to the (s,1,2) Lamb mode (**Equation 6.1.1**) is present. Switching-on the interaction (a_0>0) results in two spectral features: i) appearance of the interaction induced peak (s,1,1) which resembles DOS of propagating longitudinal phonons, and ii) blue-shift and splitting of the peak originating in the (s,1,2) mode. For the latter, the BLS spectrum suggests two Lorentzian peaks as shown with two experimental (s,1,2) shapes of **Figure 6.1.1a**. According to the BLS spectra, which can be calculated by the previous method[142] if the mode displacement field is available by FEM calculations (see detail in chapter 4.1.5), these two split peaks allows a rough estimation of the Lamb frequency, f_L, of a free sphere using $f_L = 2f_1 - f_2$, where f_1 and f_2 are the maximum frequencies of the two Lorentzians used to fit the experimental spectrum (rationalization of this relation is available in **Chapter 6.1.5.**), and therefore, c_t in the individual NPs is calculated from **Equation 6.1.1**. For PS$_A$-141 and PS$_A$-707, $c_t = 840$ m/s, whereas for PS$_B$-190 and PS$_B$-202, $c_t = 930$ m/s, which means that the effective c_t does not depend on the particle size, but on the particle chemistry. The result of the calculation will be further discussed in the Discussion section to verify the nanoconfinement effect.

Temperature-dependent particle vibrational modes

Well below T_g, temperature can have a minor impact in the frequency of the internal (s,1,2) mode, since the thermal expansion coefficient is very small (for PS is about 7×10^{-5} K^{-1}).[152] Thus, the observed red shift of the f(s,1,2) mode reflects the decrease of c_t(T).[149,153] Approaching the glass transition temperature of the NPs, their T_g is marked by the softening of c_t and subsequent formation of a polymer film activated by chain mobility. Based on the preceding section, the interaction induced (s,1,1) mode associated with K_{eff} and M should be insensitive to temperature variation since the frozen segmental dynamics in the glassy state preclude change of interactions. Thus, an analysis of the temperature dependence of the (s,1,1) and (s,1,2) modes will allow not only to monitor and understand the thermal behavior of these polymer NPs, but also to identify thermal transitions. For simplicity, we first examine PS$_A$-707 for which the (s,1,1) is not resolved.
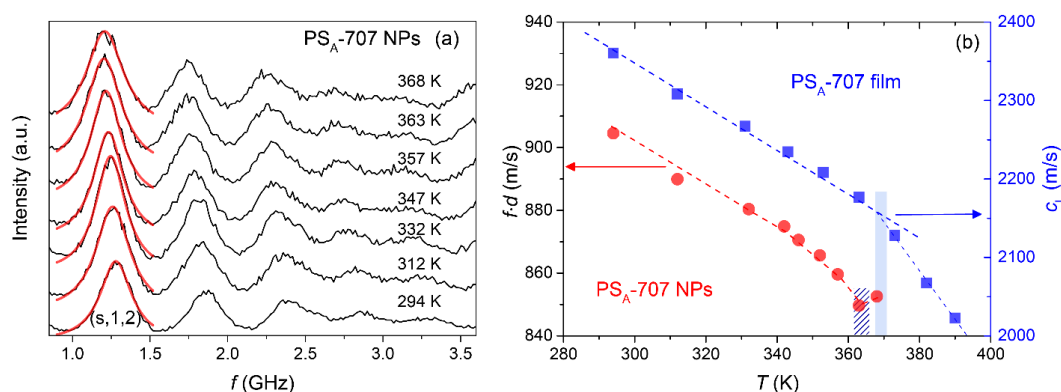

Figure 6.1.3. (a) Brillouin light scattering (BLS) spectra (black line) of PS$_A$-707 at different temperature up to the formation of a contiguous PS film with (s,1,2) mode peak fitted by a Lorentzian curve (red line). **(b)** The temperature dependent f(s,1,2). Red and blue circles represent the scaled frequency $f(s,1,2) \cdot d$ for NPs (left y-axis) and the longitudinal sound velocity (c_l) of annealed bulk film (right y-axis), respectively. The hatched and filled areas in **(b)** indicate the softening T_s and glass transition T_g temperatures, respectively.[12]

Figure 6.1.3a shows eigenfrequencies of PS$_A$-707 at different temperatures. The frequencies of the (s,1,2) modes are obtained from the location of the single peak (red solid line) at maximum intensity and are shown as a function of temperature in **Figure 6.1.3b**. As the temperature is increased from 293 to 370 K, f(s,1,2) monotonically decreases reflecting the slowdown of c_t(T) $\propto$ $f(s,1,2) \cdot d$ (red in **Figure 6.1.3b**, left axis). Noticeably, this red shift is reversed into a blue shift at about 363 K, which is here called the softening temperature T_s, and the eigenmodes vanish altogether at a higher temperature, $T_g \approx 372$ K. The disappearance of particle vibrational modes does not occur in either PS particles with a rigid silica shell or annealed bulk polymer films due to the rigidity of their structures.[149,154] In this respect, the disappearance of the vibrational modes

in PS_A-707 at T ≈ 370 K (**Figure 6.1.3b**) is attributed to the structural deformation which occurs at their T_g; polymer flow induced by the activation chain dynamics (above T_g) prevents the emergence of eigenmodes due to formation of contiguous PS films. Therefore, a temperature where eigenmodes disappear can be defined as T_g of NPs. In **Figure 6.1.3b**, the T_g of the contiguous film estimated from the change of the slope, dc_l/dT, of the longitudinal sound velocity with temperature (blue filled squares) occurs at a very similar temperature with the NPs, T ≈ 369 K (blue filled area). The origin of the blue shift of $f(s,1,2)$ and the thermal transition at T_s will be discussed below.

For the smaller particles, the $f(s,1,1)$ mode is resolved from the central Rayleigh line ($f = 0$ Hz), as shown in BLS spectra of PS_A-141 NPs in **Figure 6.1.4a**. For a better resolution of the interaction-induced (s,1,1) mode, the data of **Figure 6.1.4a** were scaled by multiplying the measured intensity by the square of frequency, $I \cdot f^2$; see **Figure 6.1.4b**. Several key features about the thermomechanical behavior and the adhesive interaction of PS NPs are revealed from **Figure 6.1.4a** and b: i) both the (s,1,1) and (s,1,2) modes exhibit an unexpected direction in frequency shifts; ii) the peaks of both modes broadens and split into doublets as temperature increases; and, iii) vibrational modes vanish at sufficiently high temperature as in the case of PS_A-707.
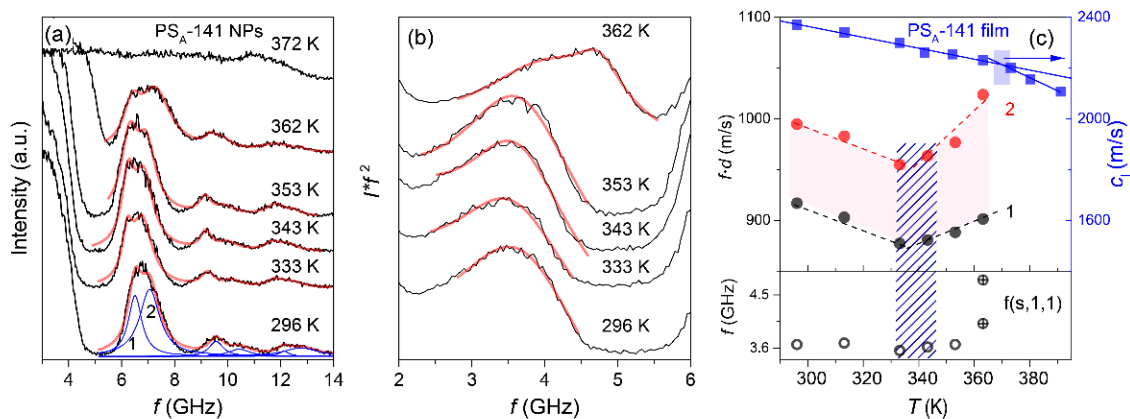

Figure 6.1.4. Estimation of particle T_g. Brillouin light scattering (BLS) spectra of PS_A-141 particles at different temperatures in two presentations: frequency f vs. **(a)** intensity, I and **(b)** $I \cdot f^2$ (power spectra). Blue lines in **(a)** refer to Lorentzian lines of (s,1,2) mode. **(c)** Temperature dependence of the frequency, $f(s,1,1)$ of the interaction-induced mode (low panel, opened circle) obtained at the maximum intensity and the scaled frequencies ($f \cdot d$) of the split fundamental (s,1,2) mode (upper panel, filled black and red circles) of PS_A-141 nanoparticles. Two crossed open circles in the low panel indicate two Lorentzian curve fit of a split $f(s,1,1)$ doublet. The frequency of the longitudinal mode recorded at $q = 0.0146$ nm^{-1} for the contiguous PS film obtained from the PS_A-141 particles annealed at 393 K is also shown in **(c)** (upper panel, blue solid square). For PS film measurement, the annealed PS film is heated from room temperature (296 K) to 393 K. The hatched and filled areas in **(c)** indicate the softening T_s and glass transition T_g temperatures, respectively.[12]

Interestingly, the shifts of the vibrational (s,1,2) mode are not unidirectional, showing the T_s of PS_A-141 similarly with bigger PS_A-707 particles. This behavior is demonstrated in **Figure 6.1.4c**,

where the upper graph contains the frequencies of the (s,1,2) mode peak doublets in red and black and the lower plot depicts the frequency of (s,1,1) mode. The junction of the red- and blue-shifted regimes denotes a softening transition in the particle structure occurring below the T_g at about $T_s = 340$ K. Given the phonon dispersion calculation described above, this inversion, as well as the increase in f(s,1,1) at T_s, requires a significant increase in the contact area. Therefore, the blue shift of the interaction-induced (s,1,1) mode above T_s indicates an increase in particle adhesion In the blue shift of (s,1,2) mode, the blue shif represents an increase in the contact area among particles resulting in the reinforcement of interparticle adhesion force.

When particle interactions are increased, the vibrational modes are predicted to split (**Figure 6.1.2**), which is evident in **Figure 6.1.4a** and **Figure 6.1.4b** for the f(s,1,2) and the f(s,1,1) modes, respectively. As interparticle adhesion increases to the point that particles form a cohesive film, individual vibrational modes are abstracted and peaks vanish, which occurs at 372 K in **Figure 6.1.4a**. This temperature is the T_g for the NPs, and it closely mirrors that of annealed bulk PS for which the longitudinal sound velocity determined by BLS is plotted in **Figure 6.1.4c** (see blue points).

Despite the chemical similarity to PS_A-141, PS_A-707 has an overt softening temperature very close to T_g (**see Figure 6.1.3b**). Since the contact area is not linearly scaled by particle diameter ($a_0 \propto d^{2/3}$), PS_A-707 does not show a significant increase in the contact area for $T_s < T_g$ (to compensate the $f(s,1,2) \propto d^{-1}$ dependence). In contrast, PS_A-141 shows the (s,1,1) mode and its blue-shift as temperature increases. Therefore, to overcome the red shift trend below the T_s, PS_A-707 requires a higher temperature to enhance the adhesion of the particles. Conclusively, T_s of PS_A-707 is observed at higher temperature than for PS_A-141. Because the mobile layer thickness is expected to be approximately independent of particle size, it constitutes a smaller portion of larger particles and contributes less to their mechanical properties of the overall colloidal film. Note, that annealed bulk PS films lacks a softening transition associated with a mobile surface layer.

PS_A-141 NPs are annealed below their glass transition temperature to confirm the existence of the mobile surface layer. If present, the surface layer induces irreversible aging when NPs are annealed between their T_s and T_g, but not in those annealed below T_s. The results of both experiments are plotted in **Figure 6.1.5**. Annealing is performed at 353 K, between T_s and T_g, in **Figure 6.1.5a and b**, but at 326 K, below T_s, in **Figure 6.1.5c and d**. In **Figure 6.1.5a and b**, the f(s,1,1) and f(s,1,2) modes, respectively, are plotted for particles heated from 298 to 353 K in black symbols. The same softening temperature from **Figure 6.1.4** is present at 340 K, noted by the transition from a red to blue frequency shift. The particles are then annealed at 353 K for18 h, and post annealing modes are plotted in blue. The increase in the f(s,1,2) mode while annealing PS NPs at 353 K indicates increased particle adhesions resulted from the increase in contact area, which is

absent in bulk PS.[149] This discrepancy between bulk polymer behavior and the colloidal polymer films suggests aging of the mobile surface layer.

The behavior of the $f(s,1,1)$ mode under thermal annealing is also interesting: it increases in frequency above T_s, but also bifurcates after annealing. Both indicate the increase in particle-particle adhesion, which can be attributed to the fact that the mobile layer is softened so this increases a contact area abruptly at T_s. Finally, a new softening temperature of 360 K emerges during heating from 353 to 367 K due to the stiffening of the particles while PS NPs are annealed. These behavioral transitions that occur below the T_g, existence of a softening temperature, splitting of the $f(s,1,1)$ mode, and time-dependent vibrational modes, are unique to NPs and verify the presence of a mobile surface layer.[155,156]
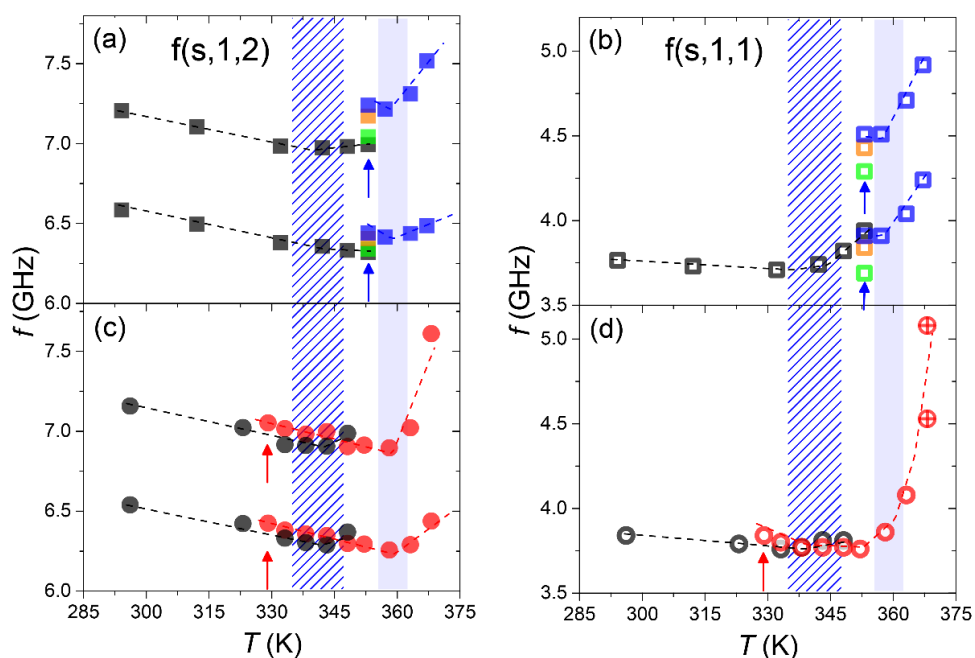

Figure 6.1.5. Annealing effects of PS$_A$-141. The frequencies of the (s,1,2) (**a** and **c**) and interaction induced (s,1,1) (**b** and **d**) modes obtained at the maximum intensity as a function of temperature. Black symbols indicate eigenfrequencies at the initial heating, and blue and red symbols are recorded from the second heating after particle annealing at 353 K (above T_s, blue arrow), **(a)** and **(b)**, and at 326 K (above T_s, blue arrow), **(c)** and **(d)**, respectively. A gap between two Lorentzian fits of $f(s,1,2)$ doublets is marked with black, blue, and red filled areas, referring to the initial heating, second heating after annealed above T_s, and after annealed below T_s, respectively. Annealing below T_s causes peak-splitting of $f(s,1,1)$ mode at 373 K (two crossed open red circles in **(d)**). Annealing above T_s results in a doublet of $f(s,1,1)$ at 353 K, and the hardening of both (s,1,2) and (s,1,1) modes is indicated by green (1 h), orange (9 h) and blue (18 h annealing) squares. In **(b)** and **(d)**, dashed and filled areas indicate the position of T_s before and after the annealing process, respectively.[12]

The results of **Figure 6.1.5a** and **b** are corroborated by those presented in **Figure 6.1.5c** and **d**, where particles are annealed below their T_s at 326 K. Initially, particles are heated from 298 to 353

K as before, then slowly cooled to 329 K and annealed for 10 h. After annealing, the $f(s,1,1)$ and $f(s,1,2)$ modes show small increases in frequency due to increased particle aging from being heated temporarily above T_s at the initial heating. Next, particles are heated from 329 to 367 K which reveals the same increase in softening temperature to 360 K, as in the high-temperature annealing scenario, because of the stiffened surface layer. However, the $f(s,1,1)$ mode does not bifurcate until heated to 373 K, demonstrating weaker adhesion among NPs. This can be attributed to incomplete softening of the surface layer during the first temperature scan and the thermal annealing. When particles are thermally heated longer to be completely transitioned at the second scan, the softened mobile layer increases the contact area, as well as the adhesion force, and this point is observed by the $f(s,1,1)$ doublet at T=373 K. Despite the structural changes observed in the particles during annealing, the T_g is consistently measured at 373 K. The results of **Figure 6.1.5** confirm the presence of a mobile surface layer and its significant influence on the interparticle adhesion among polymer NPs.
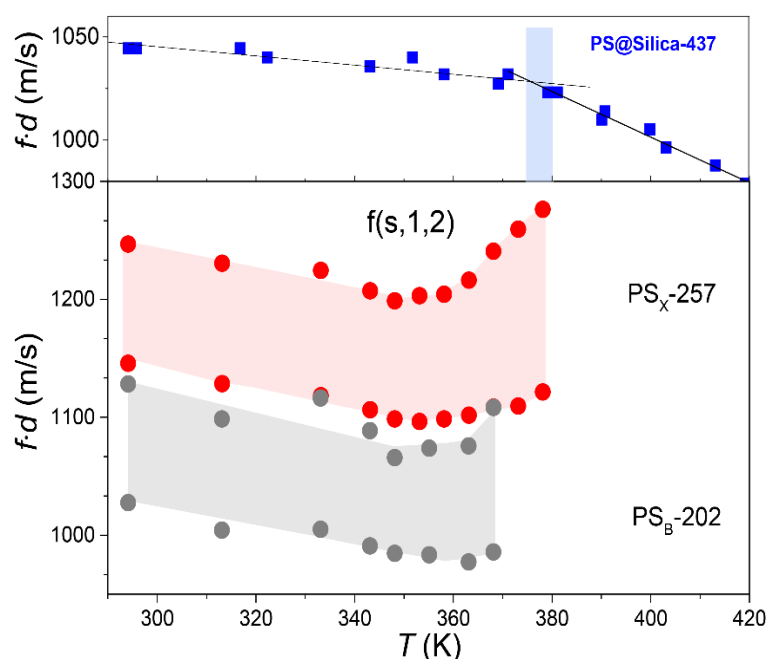
Figure 6.1.6. The influence of chemistry on the colloid vibration. The temperature dependence of $f(s,1,2) \cdot d$ of PS/silica core/shell (PSS-437) particle (blue, top) with diameter $d = 473$ nm, that is previously reported data,[154] PS_X-257 (red), and PS_B-202 (gray). Blue filled area indicates the glass transition temperature of PSS-437 nanoparticles. Red and gray areas highlight the gap between two Lorentzian peaks of (s,1,2) mode of PS_X-257 and PS_B-202, respectively.[12]

The effect of surface mobile layer can be augmented by chemically modifying NPs to enhance the elasticity and its contrast between the bulk-like core and mobile shell, respectively. Two particles were synthesized with this property, PS_B-202 and PS_X-257. PS_B-202 is a 202 nm PS particle copolymerized with acrylic acid, which increases the elastic modulus over bare PS particles. Previously, an increase in an elastic modulus of a PS_B-202 colloidal cluster had been shown with a

larger scaled frequency $f(s, 1,2) \cdot d$ than that of PS_A-141 in **Figure 6.1.1c**. PS_X-257 is chemically similar to PS_B-202, but polymerized in the presence of a crosslinker at low concentration (5.0 wt. % divinyl benzene). As the particles grow, the crosslinker depletes, yielding particles with a crosslinked core and shell of free polymer chains.[157] The increased elastic modulus afforded by crosslinking is evident in the high-frequency of scaled $f(s, 1,2) \cdot d$ mode presented in **Figure 6.1.6** over various temperatures; the BLS spectra of the three PS NPs particles (PS_B-190, PS_B-202, and PS_X-257) are shown in **Figure S6.1.2** and **S6.1.3**. **Figure 6.1.6** shows that both PS_B-202 and PS_X-257 have softening temperatures around 353 K, higher than the 340 K of PS_A-141, which confirms their greater elastic modulus even in their surface mobile layer and the smaller surface to volume ratio. As a result of the crosslinking, the T_g of PS_X-257 is higher than for PS_B-202 as indicated by the different temperatures at which contiguous films are formed in **Figure 6.1.6** (lower panel). The latter displays the same T_g, obtained from temperature dependent sound velocity in the bulk films (**Figure S6.1.4**), with the T_g of the corresponding NPs.

The effect of the surface layer mobility on particle mechanics becomes apparent when a rigid surface layer is added to PS NPs, shown in **Figure 6.1.6** (blue closed squares). PSS-473 NPs are cross-linked polystyrene particles confined by a thin (14 nm) hard silica shell with diameter $d = 473$ nm. The silica shell significantly retards the mobility of the surface polymer layer, which eliminates the softening temperature in turn.[4] Moreover, because silica does not undergo a glass transition, the T_g marks only the transition of the polymer core from glassy to liquid rather than the loss of vibrational modes as in all PS NPs. The glass transition behavior of PSS-473 NPs resembles that of bulk polymer, as presented in **Figure 6.1.4c**, but is about 10 K greater due to its crosslinked nature.[158] Consistently, higher T_g was displayed by the PS_X-257 NP demonstrating that hard confinement suppresses the surface mobility. The thermal behaviors of annealed PS films follow that of the hard nanoconfined NPs,[154] which reflects the disappearance of surface layer in NPs and their effects.

6.1.3. Discussion

The particle vibration spectroscopy used here probes the mechanical properties of polymer NPs, varying in size and surface characteristics, including their glass transition behavior and mechanical adhesion forces among NPs in a colloidal cluster. The temperature dependence of the vibrational modes yields information about the thermal relaxation of the NPs probed through the reinforcement of the interparticle mechanical adhesion induced by the presence of a surface mobile layer. FEM calculations of the phonon bands in the colloidal cluster disentangled the effects of interaction from the free NP mechanics. Three novel findings emerge from this study; i) robustness of T_g to the

sample geometry (**Figure 6.1.3, 6.1.4,** and **6.1.6**), ii) discovery of softening transition below T_g (**Figure 6.1.4** and **6.1.6**), and iii) confinement effect on the elastic (shear) modulus (**Figure 6.1.1b**).

To corroborate the first finding, we also measured T_g by modulated differential scanning calorimetry (MDSC). The results are shown in **Figure 6.1.7a**. For the examined samples, the T_g measured by BLS (filled area in **Figure 6.1.7a**) is about 7-10 K lower than that of MDSC (hatched
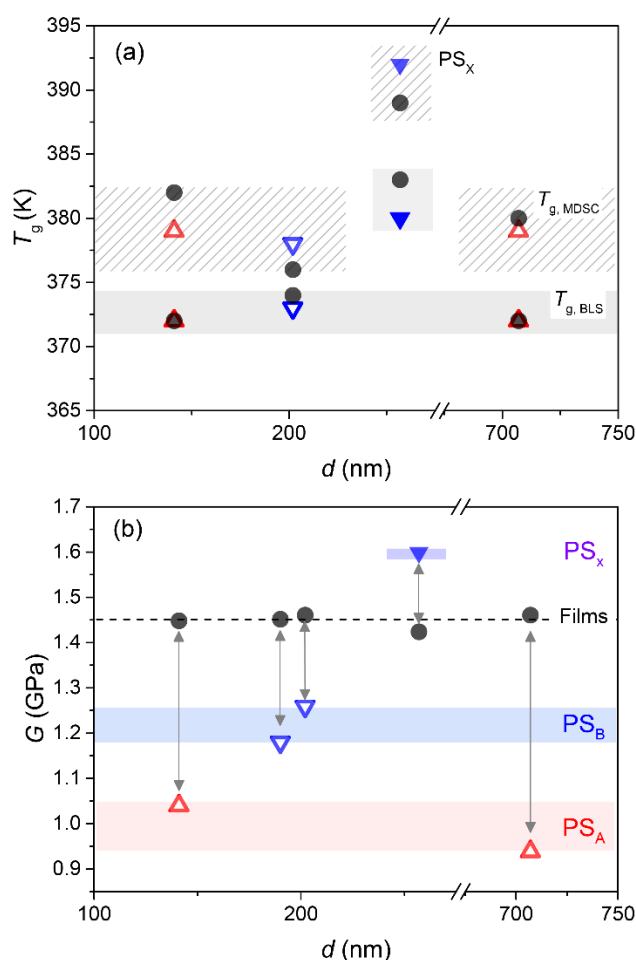

Figure 6.1.7. The glass transition temperature T_g and shear modulus G of NPs and the corresponding annealed films. **(a)** T_g both for nanoparticle powder state and for annealed bulk state (black solid circles) obtained by modulated differential scanning calorimetry (MDSC) thermograms (**Figure S6.1.6** in **Chapter 6.1.5**, supplementary information) and Brillouin light scattering (BLS) indicated by the dashed and filled areas, respectively. The crosslinked PS_X-257 NP (solid back circle) and corresponding annealed film (blue triangle) assume higher T_g values measured by the two techniques (MDSC, dashed and BLS, filled area). **(b)** Shear modulus (G) of the different NPs (blue circles) and the corresponding annealed films (red circles). The black dotted line indicates the average value of G in the annealed bulk films. Arrows indicate nanoconfinement effect of NPs compared to their corresponding films. Blue and red areas refer to the softening of PS_A and PS_B type NPs, respectively. The purple area above indicates the hardening of crosslinked PS_X NPs.[12]

area in **Figure 6.1.7a**). This constant disparity in T_g as measured by BLS and MDSC is attributed to two effects: (i) the difference underlying physical mechanisms of each approach, whereby MDSC relies on the polymer segmental relaxation and BLS is based on the softening of the elastic modulus[153] and (ii) the quasi-isothermal vs. cooling ramp measurements of BLS and MDSC, respectively.[159] Given the typical inconsistency between the two methods,[149] the robustness of T_g is verified, even if a significant T_g reduction is not captured. For PS_A NPs, the addition of sodium 4-vinylbenzylsulfonate during synthesis can have an influence on T_g, which is resulted from the different environmental factors. In case of PS_B NPs, furthermore, the absence of the T_g reduction can relate to the high concentration of acrylic acid, which could effectively behave as ionic surfactant.[160] Consequently, the additives alter the interfacial environment of the NPs as previously reported.[7,8] For instance, Feng *et al.*[7] illustrated a suppression and invariant in T_g with confinement for PS nanoparticles without and with surfactants, respectively. Finally we note that several studies have shown that the magnitude of depression in T_g of confined PS is dependent on cooling rate, with higher rates cooling leading to a near complete elimination of size effects on T_g.[161] In this study, the rates of cooling/heating are well within range in which confinement strongly influences T_g. Hence, the absence of depression in T_g of our nanoparticles cannot be related to rate effects in the measurement of T_g.

The second observation of the softening temperature provides strong evidence for the existence of a surface mobile layer atop the NP (qualitative calculation of the relation between contact area and $f(s,1,2)$ blue-shift above T_s is available in **Chapter 6.1.5**. Supplementary Information). However, in view of the absence of a depression in T_g with decreasing NP diameter, this finding appears counterintuitive and can suggest either decoupling between surface dynamics and T_g with confinement[129] or the need of a sufficiently thick mobile surface to impact the T_g. The former possibility assumes that mobility is less affected by interfacial effects compared to T_g. The presence of sodium-4-vinylbenzylsoulfonate (PS_A) or acrylic acid (PS_B) in the surface layer effectively eliminates the T_g confinement effect and promotes particle–particle adhesion with the presence of mobile surface layer. The temperature-dependent eigenfrequencies of core/shell NPs shown in **Figure 6.1.5** confirm that the surface mobility is due not to a radial density gradient, but to a gradient in dynamics, and the effect of surface mobility on the softening temperature will be further investigated by modifying the surface layer of the NP in a core/shell topology.

Concerning to the third finding, **Figure 6.1.7b** displays the elastic shear modulus for all examined NPs and the corresponding annealed films at ambient conditions. A comparison of the shear modulus for the two geometries (NP's vs. films) clearly reveals a large difference between the two. For both PS_A and PS_B, the nanoparticle analog exhibits a much lower modulus in comparison to the annealed bulk films of each polymer. We suggest that this difference in modulus between NPs and annealed bulk films is a direct manifestation of the significant difference in the

surface to volume ratio and surface mobility. This effect is consistent with reports of a dispersion in elastic modulus of thin PS films floated atop a liquid substrate.[162] The difference in the modulus between NPs of PS_A and PS_B is due to the different chemistries between PS_A and PS_B. We also note that for each PS_A and PS_B NPs, in which only two different diameters were investigated, no clear trend in T_g with decreasing NP diameter was observed; thought caution should be taken as only two NP diameters were available for investigation.

Finally, in the case of uncrosslinked (PS_B-202) and crosslinked (PS_X-257), the observed difference (~25%) in the G values becomes negligible in the corresponding PS films. Mechanical hardening occurs only for the crosslinked NPs, whereas all uncrosslinked NPs are softer. The elasticity of the surface layer (uncrosslinked or crosslinked) can impact the NPs' $f(s,1,2) \cdot d$ (blue or red shift in **Figure 6.1.1b**) depending on its shear modulus and thickness. During film formation (above T_g), structural rearrangement of the surface layer leads to contiguous films with all displaying bulk elasticity (**Figure 6.1.7b**).

6.1.4. Methods

Polystyrene Nanoparticle Synthesis and Characterization

PS NPs were synthesized according to the procedure developed previously.[163,164] Briefly, PS_A particles were synthesized by using surfactant-free emulsion polymerization in the presence of methanol and sodium 4-vinylbenzylsulfonate (NaVBS, Sigma-Aldrich) to control both the particle size and polydispersity. In 250 mL glass flask, a mixture of 130 mL of high-purity water (Milli-pore Direct-Q, resistivity ≥ 18.2 M$\Omega \cdot$ cm) and 40 mL of methanol (Fisher Scientific) was added under nitrogen condition. Next, 0.2 g of NaVBS (Sigma-Aldrich) was added. The solution was heated to 65 °C for 30 min, after which 25 mL of styrene monomer (0.5 wt. %) containing 0.5 wt. % potassium persulfate (Sigma-Aldrich) was added. The mixture was allowed to polymerize in excess of 8 h. PS_B NPs are synthesized with acrylic acid (AA, Sigma-Aldrich). A 230 mL of water was added into a glass flash equipped with a reflux condenser and the flask was heated to 80 °C under argon gas while stirring at 1200 rpm. After a stable temperature was reached, 3.2 g styrene and 0.2 g AA dissolved in 10 mL of water were added in sequence after 10 min equilibration time. The polymerization was initiated by adding 0.2 g of ammonium persulfate (APS, Sigma-Aldrich) dissolved in 10 mL of water. The stirring rate was kept at 700 rpm and the reaction was continued for 24 h. After the synthesis was complete, particles were washed three times by centrifuging and replacing supernatant water, and the particles were finally suspended in ultra-pure water. The crosslinked PS_X particles were synthesized, as PS_B NPs are prepared, in the presence of 0.16 g divinylbenzene (DVB, Sigma-Aldrich). Particle shape and size distribution were measured with

scanning electron microscopy (JEOL JSM-7400F) with an accelerating voltage of 3.0 kV. Samples were coated with gold.

Preparation of the Colloidal Film

Glass substrates were cleaned in a sulfuric acid (Fisher Scientific) with 1 wt % of NOCHROMIX (Sigma-Aldrich) mixture for 8 h, then rinsed with water and dried under nitrogen gas. Before sample preparation, the glass substrates were cleaned under oxygen plasma. Colloidal films were prepared by drying a particle suspension between two glass substrates. A 200 μm spacer was placed between a glass slide ($25\,\mathrm{mm} \times 75\,\mathrm{mm} \times 1\,\mathrm{mm}$) and a coverslip ($22\,\mathrm{mm} \times 22\,\mathrm{mm}$) with a 2 mm gap as a sample loading channel. Samples were injected into the channel and the medium was allowed to dry at room temperature.

Modulated Differential Scanning Calorimetry

Modulated differential scanning calorimetry (MDSC) experiments were performed with polystyrene particles in suspension, as a dried colloidal powder, or an annealed bulk polymer state. Polymer particles were washed at least five times with water before preparing a sample. Suspensions used for MDSC consisted of 1 vol. % colloid. Dried powders were prepared by evaporating the aqueous medium under vacuum at room temperature. The annealed bulk polymer was prepared by annealing dried polymer NPs at 423 K for 24 h under vacuum. MDSC measurements were made with a Discovery DSC (TA Instruments) to measure the glass transition temperature and all experiments were performed with a 4 °C/min heating rate and 30 s period of heat-only condition.

Brillouin light scattering

Brillouin light scattering (BLS) is a powerful and nondestructive technique useful for probing the thermal density fluctuations of a material by measuring the inelastic scattered light caused by thermally-activated phonons. The scattering wave vector, $\pm\mathbf{q} = \mathbf{k}_s - \mathbf{k}_i$, is defined as the difference between scattered light $\mathbf{k}_s$ and incident light $\mathbf{k}_i$. In the transparent media, such as a polystyrene film, BLS spectra consist of a single doublet with a Doppler frequency shift with magnitude $f_{l,t} = \pm\frac{c_{l,t}q}{2\pi}$ at a given q, where c_l or c_t is the longitudinal or transverse wave velocity in the media, respectively. The wave vector q is independent on the refractive index in the transmission geometry and has a magnitude $q = \frac{4\pi}{\lambda}\sin\frac{\theta}{2}$, where λ is the wavelength of incident light (λ=532 nm) and is the scattering angle. In the turbid media, such as dry polystyrene particles, q is ill-defined because of the strong multiple light scattering. Consequently, the BLS spectrum reveals the

resonance modes of the colloidal particles that uniquely defined by the geometric and elastic characteristics of the particle cluster. In temperature-controlled BLS experiments, temperature was monitored with platinum resistance temperature detectors and controlled within ± 0.5 K of the set-point value with a custom temperature controller. Samples were isothermally equilibrated at each temperature for at least 20 min before recording a spectrum.

Theoretical model: phonons in a crystal of interacting spherical particles

For a free particle of spherical shape, the low frequency vibrations can be calculated in a continuous model as done by Lamb.[11] The modes are classified in torsional and spheroidal and described by (*p, n, l, m*). Torsional modes (*p = t*) have pure shear motions, whereas spheroidal modes (*p = s*) involve both shear and stretching. The *n, l,* and *m* indices label the radial and angular dependence of the vibrational modes in spherical symmetry, in analogy to the atomic orbitals.

When the particles are deposited on a substrate, a more or less ordered cluster is formed, depending on the used technique. By depositing colloidal particles with narrow and sharp size distribution, large fcc crystals can be obtained. In the contact region, the spheres are deformed by attractive forces, even in the absence of external forces. According to the JFK model, for a small interaction, two spheres with diameter d have a circular contact area of radius a_0 in case of no external force: $a_0 = \left(\frac{3\pi d^2 W_a}{8K}\right)^{1/3} \propto d^{2/3}$, where W_a is the interaction energy per unit area of two flat parallel surfaces at a given distance and K is the bulk elastic modulus. The interaction between two spheres can be described by a spring constant normal to the contact surface given by

$$k_n = B W_a^{\frac{1}{3}} \left(\frac{d}{4}\right)^{\frac{2}{3}} K^{\frac{2}{3}} \propto d^{\frac{2}{3}} \tag{6.1.2}$$

The quantity B depends on the model assumed for the distribution of the strains in the contact volume. Compressive strains are present in the central region, while tensile strains are present in the external region of the contact circle. Within the Johnson-Kendall-Roberts model,

$$B = \frac{9}{10}\left(\frac{3\pi}{2}\right)^{\frac{1}{3}} \cong 1.5 \tag{6.1.3}$$

In this approximation of small interaction, the vibrations of the cluster are a system of rigid spheres connected by springs. The system becomes a network of quasi-spheres, each one having a contact area of radius a_0 with the twelve surrounding spheres in the fcc crystal, as shown in **Figure S6.1.8**.

The sound propagates through the spheres maintaining nearly rigid structures with strains appearing only in a small region at the contacts. In an ideal fcc crystal, the maximum vibrational frequency, for waves propagating along the [100] directions, is

$$\omega(\mathrm{k_x}) = 2\sqrt{2K_{\mathrm{eff}}/M} \qquad (6.1.4)$$

where M is the mass of the sphere. The scaling laws with the particle size, i.e. $K_{\mathrm{eff}} \propto k_{\mathrm{n}} \propto d^{2/3}$ and $M \propto d^3$, produce another scaling relation for the frequency, $\omega(\mathrm{k_x}) \propto d^{-7/6}$. In this regime, the longitudinal sound velocity of the system scales as $c_{\mathrm{l}} \propto d\sqrt{(K_{\mathrm{eff}}/M)} \propto d^{-1/6}$.

This motion can be described starting from the zero-frequency pure translation (s,1,1) mode as described in **Figure 6.1.2**. There is another phonon band that derives from a zero–frequency mode of the free sphere: the (t,1,1) band in which the free sphere rotates freely and the spheres liberate in the cluster. This band has an important frequency dispersion. All other *(p,n,l,m)* modes form bands that, for small interaction among spheres, have small frequency shift and width change with respect to the relative discrete *(p,n,l,m)* mode of the free sphere, and the mode patterns within the spheres are nearly the same with small strains at the contact and phase changes that are governed by the **q** vector.

The situation is very similar to that of a molecular crystal, where the sound propagation is determined by the interaction among molecules and optical phonon bands appear for each of the internal mode of the molecule. The symmetry is lowered from spherical to cubic at $q = 0$. The $2l+1$ degenerate vibrations of the sphere split. For example, the $l = 2$ mode is split in a doubled and a triplet, the $l = 3$ in two triplets and a singlet. At $q \neq 0$, in general, no more degenerate modes are present and the $2l+1$ components have all different frequencies. In an experiment at a defined **q**-value, a q-dependent spectrum of sharp lines will be present. In opaque samples, where multiple scattering occurs, all phonons contribute and the shapes of the *(n,l)* bands will resemble the shapes of the density of vibrational states of the crystal.

6.1.5. Supplementary information

The study reveals the presence of a surface mobile layer from the temperature dependence of both interaction (s,1,1) mode and the inherent (s,1,2) mode, which additionally is split due to the interactions. From the qualitative calculations, we can conclude that the observed frequency blue-shift above Ts results from the increase of the contact area radius, a_0, of several nanometers. However, it is difficult to make any quantitative statement how this increase relates to the thickness of mobile layer.

Figure S6.1.1 shows results of FEM calculations for fcc cluster of PS nanoparticles. This figure focuses only on the split and blue shift of the (s,1,2) (calculated at q = 0 nm^{-1}) mode shown in a normalized presentation, f(s,1,2)·d vs a_0/d (normalized contact are radius). For any particle diameter, d, the increase of the particle-particle contact results in: (i) mode splitting and (ii) blue-shift. Nevertheless, the magnitude of these two effects depends on the particle size as we illustrate for d = 141 nm (PS-141) and d = 707 nm (PS707). Following the JKR relation, $a_0 \propto d^{2/3}$ we take a_0 = 14 nm for PS-141 and a_0 = 41 nm for PS-707. (The numbers are arbitrary but provide the qualitative explanation.) Since $a_0/d \propto d^{-1/3}$, both (i) and (ii) interaction effects are larger for the smaller particle. This difference is even more apparent in the BLS original spectra (where the reduced frequency has to be divided by the particle diameter). Therefore, the mode splitting and the blue shift is less discernible for particles of bigger diameters and the temperature at which the mobile layer starts playing a role may change with surface to volume ratio of the particle. However, as the interactions give birth of (s,1,1) mode, T_s is directly discernible in the temperature dependence of the f(s,1,1).
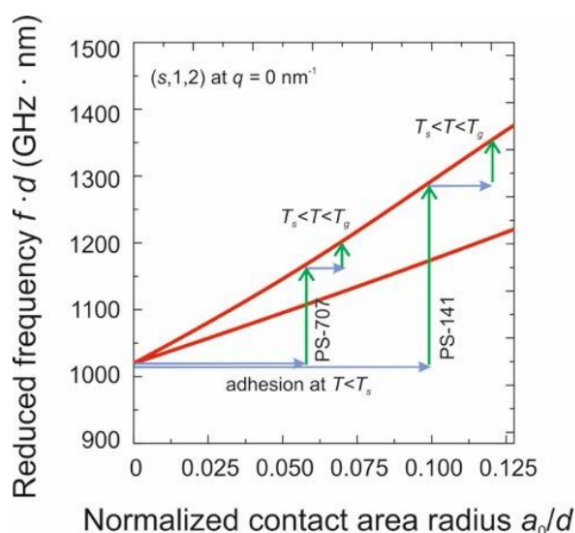

Figure S6.1.1. Graphical presentation of enhanced resolution with decreasing NP size. Reduced frequency f(s,1,2)·d as a function of the normalized contact area radius calculated at Γ point (**Figure S6.1.9**). The two branches (upper triplet and lower doublet) originating in (s,1,2) are presented. Horizontal arrows (long gray) depict the increase of the normalized contact area in the aggregation of the particles al low temperature, while the vertical arrows (green, shown only fir the upper triplet) indicate the corresponding blue-shift. Increasing temperature above T_s (short gray arrow) leads to larger blue shifts (short green arrows) for smaller NP's (PS-141 vs PS-707)[12]
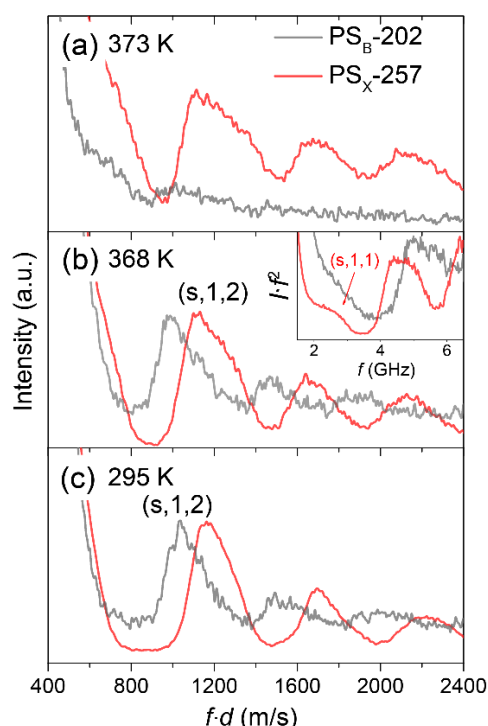
Figure S6.1.2. The influence of crosslinking on the colloid vibration. Brillouin light scattering (BLS) spectra of two polystyrene spherical particles with diameter $d = 202$ nm (PS_B-202, gray) and 257 nm (PS_X-257, red) in two presentations: $I(f)$ vs. $f \cdot d$ (main plot) at **(a)** 295 K, **(b)** 368 K, and **(c)** 373 K and (inset to **(b)**) power spectra, $I \cdot f^2$ vs. f.[12]
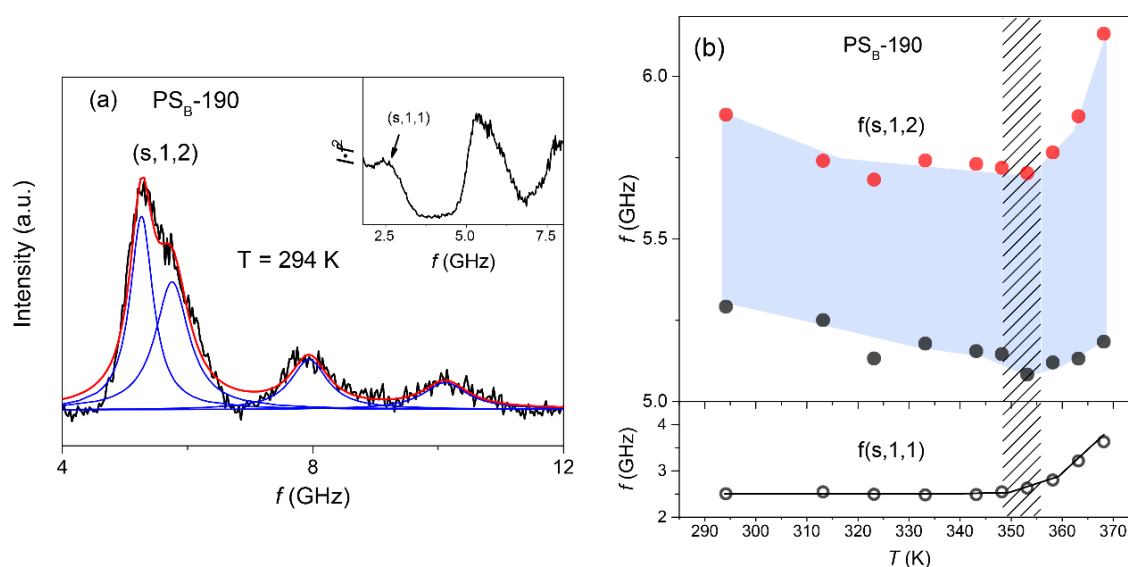

Figure S6.1.3. Temperature dependence of PS_B-190 nanoparticle eigenfrequencies. **(a)** Brillouin light scattering (BLS) spectra of PS_A-141 particles at room temperature, $T = 293$ K, as frequency f vs. intensity, I. Inset: Reduced spectra $I \cdot f^2$ $vs.$ f. Blue and red lines in **(a)** refer to Lorentzian lines of (1,2) mode and sum of them, respectively. **(b)** The temperature dependent $f(1,1)$ and $f(1,2)$ obtained at the maximum intensity for PS_B-190 are presented in the lower (open circles) and top panel (closed black and red circles indicating two frequencies of Lorentzian peaks), respectively. The hatched area in **(b)** indicates the softening T_s.[12]
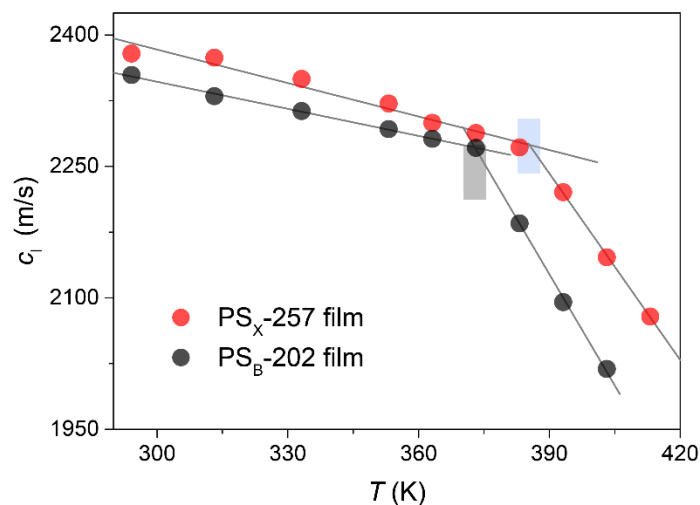
Figure S6.1.4. Temperature dependence of longitudinal sound velocities in annealed bulk films. The longitudinal sound velocities (c_l) in annealed PS_B-202 (red) and PS_X-257 (black) bulk films are recorded by increasing temperature from room temperature, T=293 K. Blue and black filled areas refer to the T_g of annealed PS_B-202 (red) and PS_X-257 (black) bulk films, respectively.[12]

Temperature dependent eigenfrequencies of core/shell nanoparticles

As described in the "Discussion", the lack of T_g depression can be attributed to a higher presence of NaVBS and AA at the surface. Therefore, given the fact that the surface mobility is due to either a gradient in dynamics (at near constant density) or a gradient in density, there should not be a lower density at the free surface for the neat PS NPs, which do not contain crosslinked networks. To support the latter, the temperature dependent eigenfrequencies of core/shell NPs (CS-168) consisting of a PS_A-141 core and a 14 nm shell are investigated. The shell is copolymer of styrene and trimethoxysilylpropylacrylate (TMSPA) with 10:1 styrene to TMSPA weight ratio. The density of this particle can be presumed to be very similar to PS. Based on **Figure S6.1.5**, the CS-168 NP with homogeneously dense shell displays higher T_s (by about 20K) and higher T_g (by about 7 K) than its parent PS_A-141 NP core. This corroborates the notion that the surface mobility is not the consequence of a gradient in density in the present polymer NPs. Instead, changing the surface dynamics in CS-168 NP impacts the softening transition temperature. Nevertheless, future work will systemically explore the role of surface capping and crosslinking on the observed properties of the nanoparticles.
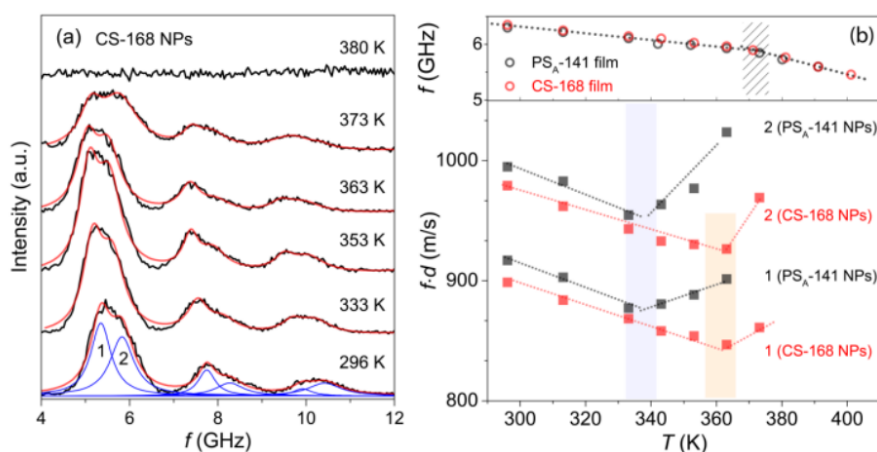
Figure S6.1.5. Glass transition temperature and softening temperature of core-shell NPs with PS_A-141 core and PS- like thin shell. **(a)** BLS spectra at different temperatures represented by Lorentzian curves and the featureless BLS spectrum at 380 K indicating the formation of a contiguous film; this temperature is higher than that measured for the PS_A-141 of **Figure 6.1.4a**. **(b)** Temperature dependence of the frequency, $f(s,1,1)$ of the interaction mode and the split $(s,1,2)$ mode (lower panel) in CS-168 and PS_A-141 NP in an scaled version ($f(s,1,2)\cdot d$) (lower panel) and the frequency of the longitudinal phonon, f (at q = 0.0167 nm^{-1}) in the contiguous film obtained from the heating of CS-168 at 410 K (upper panel).[12]
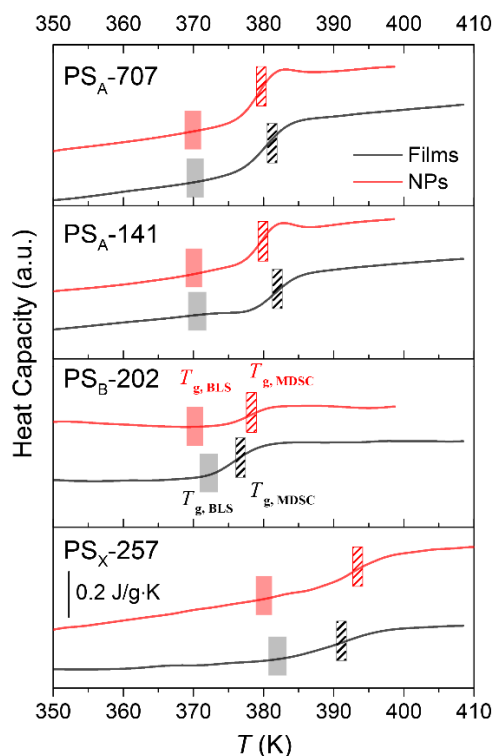
Figure S6.1.6. The modulated differential scanning calorimetry (MDSC) thermograms plotted heat capacity (arbitrary unit) vs. temperature (K) both for NPs powder state (red solid line) and for annealed bulk state (black solid line) of PS_A-707, PS_A-141, PS_B-202, and PS_X-257 (from top to bottom). The filled and dashed areas indicate T_g from BLS and from MDSC, respectively. The red and black areas refer to the T_g of the NP cluster and that of annealed bulk polystyrene, respectively.[12]

Figure S6.1.7. Scanning electron microscope (SEM) images of PS_A-141 at room temperature **(a)** without thermal annealing, **(b)** after annealing at T=363 K ($T_g > T > T_s$), and **(c)** after annealing at T=383 K ($T > T_g$). Thermal annealing has been processed for 24 hrs.[12]

Calculation of BLS spectra

The mechanical eigenmodes of single polystyrene nanoparticles (PS-NPs) and the phonon dispersion in PS NPs arranged in fcc lattice were calculated using finite element method (COMSOL Multiphysics). The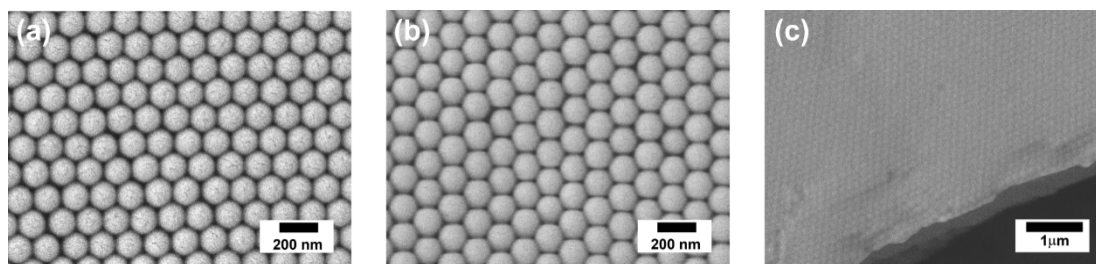 used material properties were: longitudinal speed of sound $c_l = 2350$ m/s, transverse speed of sound $c_t = 1210$ m/s, and mass density $\rho = 1050$ kg/m^3. The primitive unit cell is defined as shown in **Figure S6.1.8**. For simplicity we assume perfect bonding among the neighboring NPs. This interaction is governed by the circular contact area of radius a_0, which follows Johnson-Kendall-Roberts (JKR) model. In this case, a_0 can be related to the NP diameter d as following: $a_0 \cong 0.24\, d^{2/3}$. Using the notation as in Supplementary **Figure S6.1.8**, the primitive basis vectors are $\mathbf{a_1} = \frac{a'}{2}[0,1,1]$, $\mathbf{a_2} = \frac{a'}{2}[1,0,1]$, and $\mathbf{a_3} = \frac{a'}{2}[1,1,0]$, where $a' = \sqrt{2(d^2 - 4a_0^2)}$ is the lattice reduced by the particle adhesion. The basis vectors of the reciprocal lattice are further defined in a common manner. To check the effect of the increased contact area we calculated eigenfrequecies at Γ ($\mathbf{q} = [0,0,0]$) for d=141 nm (for example, PS_A-141) as a function of a_0. The results and the normalized values (top and right axis) are displayed in **Figure S6.1.9**. Since only spheroidal modes are BLS active, we may conclude that A1-C1 and L1-P1 modes are in principle observed in BLS. A1-C1 have zero frequency at $q = 0$ and non-zero for L1-P1. These modes (L1-P1) are originated from (s,1,2) mode at $a_0 = 0$ and split into two groups, 1) L1 and M1 and 2) N1, O1, and P1. At higher a_0, f(s,1,2) gradually increase. In other words a finite contact area results in two (s,1,2) peaks in BLS spectra, which can increase their frequency and splitting upon an increased contact area. Nevertheless, as the contact area radius scales as $a_0 \sim d^{2/3}$ this effect is less pronounced for bigger spheres. This is evident if we use normalized units (top and right axis in Supplementary **Figure S6.1.9**). Here we compare PS_A-141and PS_A-707 by taking a_0 based on JKR model; for $d = 707$ nm, $a_0 = 19.2$ nm and for $d = 141$ nm, $a_0 = 6.6$ nm. In this

case (dotted arrows in **Figure S6.1.8**) the expected normalized frequency and splitting is smaller for PS-707, what agrees with the BLS experimental data.
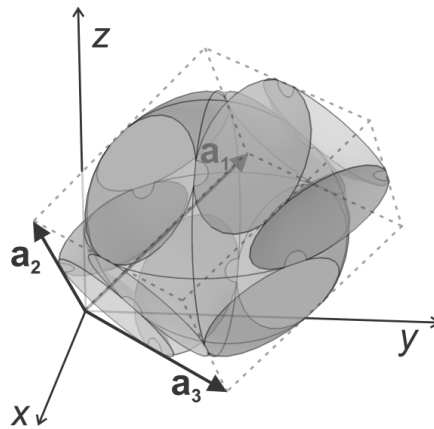
Figure S6.1.8. Primitive unit cell of a particle with interaction among neighboring particles used for finite element method (FEM) calculation.[12]
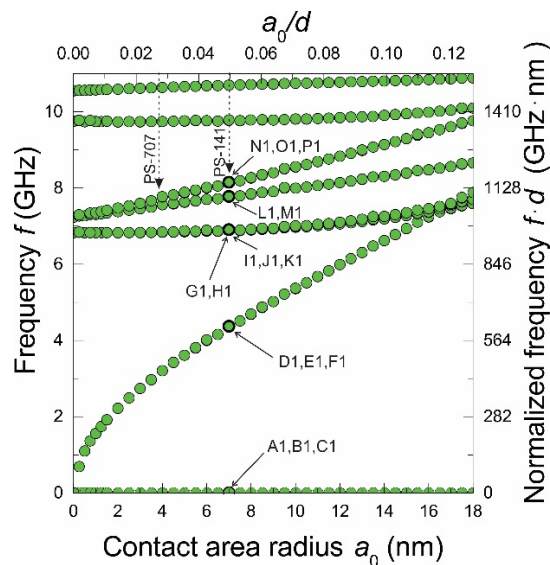
Figure S6.1.9. Mechanical eigenmode frequencies as a function of radius a_0 the contact area, calculated for PS sphere with diameter, $d = 141$ nm, at Γ (q = [0,0,0]).[12]

Brillouin spectra of fcc crystals of spheres

The five (s,1,2) modes periodically transform the sphere in an oblate and a prolate ellipsoid. At **q** = 0, where all particles move in phase, the quintet splits in a doublet and a triplet due to the lowering of the symmetry from spherical to cubic. Further degeneracy is removed at **q** ≠ 0. In principle, one could calculate the Brillouin spectra by the previous method,[142] if the mode pattern

are available by FEM calculations. The following quantities are important: i) the maximum q-value in the experiment (in our case, $\mathbf{q}_{bs} = 4\pi n/\lambda = 0.375$ nm^{-1}, meaning back scattering, for $\lambda = 532$ nm and a refractive index of PS, n = 1.59) and ii) the size of the Brillouin zone, measurable by the $\mathbf{q}_X$ value at the X-point ($\mathbf{q}_X = \pi/D_{100}$); the q-dependence of the Brillouin activity, that has a broad maximum at about qd = 6.4 in the free sphere. In the case of PS$_A$-141 particle, $\mathbf{q}_X = 0.032$ nm^{-1}, smaller than $\mathbf{q}_{bs}$. Therefore, Brillouin scattering can occur at all q-vectors of the Brillouin zone. This is quite different from the Brillouin spectroscopy by laser light in simple crystals, where the size of the unit cell is of the order of a fraction of nm, and the Brillouin zone (BZ) has a size of the order of 10 nm^{-1}, and where only a small volume of the BZ around the Γ-point is achievable. It is similar to the Brillouin spectroscopy by inelastic X-ray scattering. For even larger sizes of the unit cell, the BZ size is further reduced and many BZs are achievable. In the presence of multiple scattering, all q-vectors contribute. The lineshapes of the Brillouin bands will resemble the density of phonon states, but modulated by a q dependence of the activity.[140,142,144,145] Therefore, we will use only qualitative argumentation to describe the shape of the Brillouin bands.

The sound velocities can be estimated from the cut-off frequencies reported in **Figure 6.1.1c** that is associated with the frequency of the longitudinal acoustic band at the X point of a fcc crystal. In fact, for phonon propagation along the [100] direction, the system should be well described by a linear chain of mass M at distance $D_{100} = \sqrt{(d^2 - 4a_0^2)/2}$ between next planes, coupled by elastic springs of stiffness $K_{l,t}$, for longitudinal (subscript l) or transverse (subscript t) phonons. The frequency at the X-point is given by $\omega_{l,t} = 2(K_{l,t}/M)^{1/2}$ and the sound velocity by $v_{l,t} = D_{100}(K_{l,t}/M)^{1/2}$.[165] Therefore, $v_{l,t} = D_{100}\omega_{l,t}/2$. In this way, the sound velocities of the clusters can be estimated by taking the measured values of $\omega_l = 2\pi f(1,1)$ from **Figure 6.1.1c**. The estimated values are reported in **Table S6.1.1**.

As for the (s,1,2) band, the FEM calculations show two main results: i) the phonon band has its low frequency tail at the Lamb frequency of the free particle; ii) a splitting at q = 0 and a nearly flat dispersion of two components. The latter suggests a two peaked DOS, associated with the observed two peaked structure of the experimental (s,1,2) shapes of **Figure 6.1.1a**. Based on the calculated BLS spectra, a rough estimation can be made using two maxima of the DOS (f_1 and f_2 indicating the lower and higher peak, respectively): $f_1 - f_2 \approx f_1 - f_L(s, 1,2)$, where $f_L(s, 1,2)$ is the frequency of the free sphere. Within this simple model, we have two methods for estimating the single particle frequency: i) $f_L(s, 1,2) = f_{lfco}$ where f_{lfco} refers to the low frequency cutoff of the observed peak and ii) $f_L(s, 1,2) = 2f_1 - f_2$, when the splitting is observed. FEM calculations at $q = 0$ as a function of a_0 (**Figure S6.1.9**), which gives a measure of the strength of the interaction, show that the splitting and the shift of the doublet (L1 and M1) and triplet (N1, O1, and P1) of the (s,1,2) modes are nearly linear with a_0. This ensures that the above two methods can be used for particles having different sizes and interactions among them. In all cases when the two methods are

used, the same result is obtained within the estimated error and the calculation results are reported in **Table S6.1.1** together with the effective transverse sound velocity of the free particle obtained by inverting the Lamb equation (**Equation 6.1.1**).

Table S6.1.1. Estimated $f_L(s, 1,2)$ by the equation, $f_L(s, 1,2) = 2f_1 - f_2$ (values in the parenthesis are from the equation $f_L(s, 1,2) = f_{lfco}$). $c_{t,eff}$ is obtained by using the Lamb equation in **Equation 6.1.1**. For $f_L(s, 1,2) \cdot d$ and $c_{t,eff}$, an error of about 5% has been estimated on the basis of the used methods. The values for PS-707 is derived from a rough deconvolution of the experimental lineshape (a nearly Gaussian with a width that is about 90% of the width of the observed peak).

Sample	f_1 [GHz]	f_2 [GHz]	$f_L(s, 1,2)$ [GHz], ($\pm$ 20)	$f_L(s, 1,2) \cdot d$ [m/s], ($\pm$ 40)	$c_{t,eff}$ [m/s], ($\pm$ 50)
PS$_A$-141	6.5	7.1	6.0 (6.0)	840 (840)	1000
PS$_B$-190	5.3	5.9	4.7 (4.7)	900 (900)	1070
PS$_B$-202	5.1	5.6	4.6 (4.6)	930 (930)	1100
PS$_x$-257	4.5	4.9	4.1 (4.0)	1040 (1020)	1240
PS$_A$-707	-	-	- (1.2)	- (840)	1000

6.2. Ultrathin Shell Layers Dramatically Influence Polymer Nanoparticle Surface Mobility

Advances in nanoparticle synthesis, self-assembly, and surface coating or patterning has enabled a diverse array of applications ranging from photonic and phononic crystal fabrication to drug delivery vehicles. One of the key obstacles restricting its potential is structural and thermal stability. The presence of a glass transition can facilitate deformation within nanoparticles, thus resulting in a significant alteration in structure and performance. Recently, we detected a glassy-state transition within individual polystyrene nanoparticles and related its origin to the presence of a surface layer with enhanced dynamics compared to the bulk. The presence of this mobile layer could have dramatic impact on the thermal stability of polymer nanoparticles. Here, we demonstrate how the addition of shell layer, as thin as a single polymer chain, atop the nanoparticles could completely eliminate any evidence of enhanced mobility at the surface of polystyrene nanoparticles. The ultrathin polymer shell layers were placed atop the nanoparticles via two approaches: i) covalent bonding or ii) electrostatic interactions. The temperature dependence of the particle vibrational spectrum, as recorded by Brillouin light scattering, was used to probe the surface mobility of nanoparticles with and without a shell layer. Beyond suppression of the surface mobility, the presence of the ultrathin polymer shell layers impacted the nanoparticle glass transition temperature and shear modulus, albeit to a lesser extent. The implication of this work is that the core-shell architecture allows for tailoring nanoparticle elasticity, surface softening and glass transition temperature.

6.2.1. Introduction

Nanomaterials made of polymer nanoparticles (NPs) have been widely studied for their unique optical and mechanical properties, which are made possible due to their nanostructure. Emerging state-of-the-art techniques for self-assembling NPs has enabled more complex structures and nucleated numerous applications including photonic[166,167] and phononic crystals,[115,116,168] drug delivery,[109,169] and sensing materials.[170,171] Polymer NPs are, however, thermally unstable so their performance can be easily disturbed by temperature variation resulting in structural deformation above the glass transition temperature (T_g). For instance, it has been reported that drug release of NPs is activated by increasing the temperature near the T_g of a polymer NP carrier.[10,11] In the case of photonics applications, colloidal crystals should be treated below the T_g to prevent NPs from fusing into consolidated films.[12] Nonetheless, mechanical properties of colloidal films composed of polymer NPs have received less attention in comparison to polymer thin films due to experimental limitations in the ability to study the temperature dependence of mechanical properties of polymer

NPs.[159,175] In addition, polymer dynamics of NPs is quite complex given nanoconfinement effects and cohesive forces between adjacent polymer NPs in colloidal films.

We have recently reported that temperature-dependent Brillouin light scattering (BLS) spectroscopy can be used to estimate the shear modulus and characteristic softening temperature (T_s) of polymer NPs *via* analysis of their mechanical vibrational spectra.[12] Particle vibrational frequencies revealed not only the thermomechanical properties of NPs, but also the adhesive force between neighbors. By systematically scanning the eigenfrequencies, these experiments showed the first direct experimental observation of a thermal transition well below the T_g of polystyrene (PS) NPs, which verified the activation and presence of a mobile surface layer within PS NPs, as previously suggested.[4]

Based on the fundamental study of onset of surface mobility activation, it raises a question how one can control the thermal response of polymer NPs by tuning the surface mobile layer in terms of its glass transition dynamics. Since the surface mobile layer causes enhanced polymer segmental dynamics at the interface with the surrounding medium, the resulting T_g of polymer NPs is typically reduced.[4,6,7,118,119,126,127] To improve the thermal stability of polymer NPs, it is crucial to control the thermal and mechanical properties of individual NPs, in addition to any adhesion between them. Here, we modify the surface of NPs with the aim to tailor the polymer surface mobility, and therefore, thermomechanical properties of individual NPs. Polystyrene core-shell structured NPs that have thin shells with different T_g values compared to the core T_g were employed to exploit interfacial effects on the thermomechanical properties. The thin shells were synthesized by seeded emulsion polymerization or by physical adsorption based on electrostatic interactions between the core polymer and oppositely charged polyelectrolytes in manner similar to layer-by-layer (LbL) adsorption.[54,176] BLS was used to measure the shear modulus and softening temperature T_s, defined subsequently, of NPs assembled atop a glass substrate while T_g of the aqueous suspended NPs was measured by modulated differential scanning calorimetry (MDSC). All annealed contiguous films were compared with the corresponding NPs to understand how the structure of the shell influences (or not) surface mobility of NPs. We demonstrate that by varying the shell composition of core-shell polymer NPs that surface mobility can be tuned, which subsequently impacted NP interparticle interactions and thermal mechanical properties.

6.2.2. Experimental section

Preparation of core-shell nanoparticles

Two types of different polystyrene cores were used to create the shell architecture system and LbL architecture NPs. For the shell architecture system (PS$_A$ system), we adopted styrene as a monomer and acrylic acid as a comonomer. PS$_A$ NPs were used for as the core for shell architecture

64

NPs, PS_A-PS and PS_A-poly(methyl methacrylate) (PMMA) core-shell NPs. All polymer suspension was treated water and ethanol mixture to remove unreacted monomer and impurities before use. For LbL architecture system (PS_B system), we used styrene as a monomer and sodium 4-vinylbenzylsulfonate (NaVBS) as a comonomer.[163] PS_B@poly(diallyldimethylammonium chloride) (PDADMAC) and PS_B@PDADMAC@poly(sodium 4-styrenesulfonate) (PSS) polyelectrolytes adsorbed nanoparticles were prepared by layer-by-layer (LbL) polyelectrolyte adsorption method.[54,177] Briefly, 0.5 mL of PS_B NPs (0.5 vol. % suspended in water) was mixed with 0.5 mL of PDADMAC (MW<100 000) cationic polyelectrolyte (20 mg/mL in 0.5 M NaCl aqueous solution) and a mixture is vortexed for 30 min. Polyelectrolyte coated NPs were washed by centrifugation and replacing medium with water (Millipore Direct-Q, resistivity ρ >18.2 MΩ·cm) following by removal of supernatant. Particle are washed three times. For another layer of anionic polyelectrolyte PSS (MW=70 000) layer adsorption, the same procedure is repeated. Information about particle diameters and shell thicknesses are on **Table 6.2.1** and more detailed procedure is on the supporting information (**Chapter 6.2.5**).

Brillouin light scattering spectroscopy

Brillouin light scattering (BLS) spectroscopy is usually applied to see direct phonon propagation relation in a medium. A high resolution six-pass tandem Fabry–Perot interferometer[178] provides non-contact, non-destructive technique to examine thermally excited elastic waves (phonons) in gigahertz regime.[179] The scattering wave vector **q** is defined by the $\mathbf{q} = \mathbf{k}_s - \mathbf{k}_i$, where $\mathbf{k}_s$ and $\mathbf{k}_i$ refer to scattered and incident wave vector, respectively.[180] For transparent media, such as the present annealed films, a specific transmission geometry ($\theta = 2\alpha$) was adopted, where θ is the angle between the incident and scattered light from sample surface and α is the incident laser angle to the surface normal of the sample. In transmission geometry, **q** lies in sample plane, and the magnitude is expressed as $q = (4\pi/\lambda)\sin(\theta/2)$, where $\lambda = 532$ nm is the wavelength of the incident laser light in vacuum.[179,181]

A description of fundamental modes of vibration of elastic spheres was first presented by H. Lamb.[11] The vibrational modes are categorized into torsional and spheroidal modes, which are obtained from the stress-free boundary condition of sphere surface.[182] The spheroidal mode accompanies shear and stretching motion of particle surface and causes radial displacement, while torsional mode accompanies only shear motion and no change on radial displacement. These modes are expressed in angular momentum (l) ($l = 0, 1, 2, \ldots$) and radial dependence of displacement (n) ($n = 0, 1, 2, \ldots$)[142] and those have specific frequencies inversely proportional to particle size.[183] In our study, polarized (vv) Brillouin spectra and constant wave vector q = 0.0167 nm^{-1} (at $\theta = 90^{\circ}$) are used to measure fundamental modes of vibration. Temperature is varied with a home-built temperature scanning apparatus.

Table 6.2.1. Characteristics dimensions for the shell and the LbL architecture polymer nanoparticles.

System	Shell Architecture			LbL Architecture[c]		
Sample	PS_A	PS_A-PS	PS_A-PMMA	PS_B	PS_B@ PDADMAC	PS_B@ PDADMAC @PSS
Core Chemical Composition	Poly (styrene-co-acrylic acid)			Poly (styrene-co-styrene sulfonate)		
Size[a] (nm)	220 ± 7	256 ± 6	236 ± 7	167 ± 4	168 ± 4	169 ± 5
Shell thickness (nm)	Core	18 ± 3	8 ± 3	Core	Ultrathin[b]	Ultrathin[b]

[a] Particle size was measured from SEM image.

[b] Physically adsorbed layer on PS_B (LbL architecture) is ultrathin, layer thickness is in error range of SEM size measurement. Surface roughness shown by SEM images in **Figure S6.2.1** (in **Chapter 6.2.5**) confirms adsorbed polyelectrolyte layers.

[c] The Zeta-potential of the three NP's is plotted in **Figure S6.2.2**.

Modulated differential scanning calorimetry

Modulated differential scanning calorimetry (TA Instruments Q2000) was conducted to determine the glass transition temperature of the core-shell nanoparticles. Nanoparticles were either suspended in water, or dried into a powder, or the dried powder was annealed overnight at 413K to anneal the NPs into a film. In all cases, the sample was briefly heated above T_g and cooled at 10 K/min then heated at a rate of 20 K/min with a modulation of 0.2 K per 20 s. **Table 6.2.2** reports the midpoint T_g measured on heating.

Table 6.2.2. Glass transition temperature (T_g) for the PS particles and PS film with thin shell by BLS and MDSC.[a]

Samples	Particle		Bulk Film	
	T_g, BLS (K)	T_g, MDSC (K)	T_g, BLS (K)	T_g, MDSC (K)
PS_A	366 ± 2	369 ± 1	368 ± 5	379 ± 1
PS_A-PS	366 ± 2	370 ± 1		375 ± 1
PS_A-PMMA	371 ± 2	370 ± 1		378 ± 1
PS_B	361 ± 2	372 ± 1		383 ± 1
PS_B@PDADMAC	361 ± 2	377 ± 1		382 ± 1
PS_B@PDADMAC@PSS	366 ± 2	374 ± 1		382 ± 1

[a] PS bulk films for both BLS and MDSC were annealed for 14 h at 413K.

6.2.3. Results and discussion

Elastic modulus and interactions

The characteristic sizes of the shell architecture, PS_A-PS, and PS_A-PMMA NPs based on PS_A core and the LbL architecture , PS_B@PDADMAC, and PS_B@PDADMAC@PSS NPs using PS_B as the core NP template are listed in **Table 6.2.1**. For the PS_A, acrylic acid was used as a comonomer, whereas the PS_B NPs were synthesized with sodium 4-vinylbenzenesulfonate as the comonomer. In the quasi core-shell PS_A-PS NP, the thin PS shell was based on the same chemistry with the PS_A core. **Figure 6.2.1a** shows the anti-Stokes side of BLS spectra of the three shell architecture NPs (**Table 6.2.1**) at 294K. In order to compare the (n,l) bands of the spectra, the scattered light intensity (I) versus frequencies (f) is normalized by particle diameter (d), where n and l denote the radial and angular dependence of the displacement of the spheroidal modes, respectively. The Lorentzian shape representation of the $f(1,2)$ branch reveals split doublets shown by gray solid lines in **Figure 6.2.1a.**
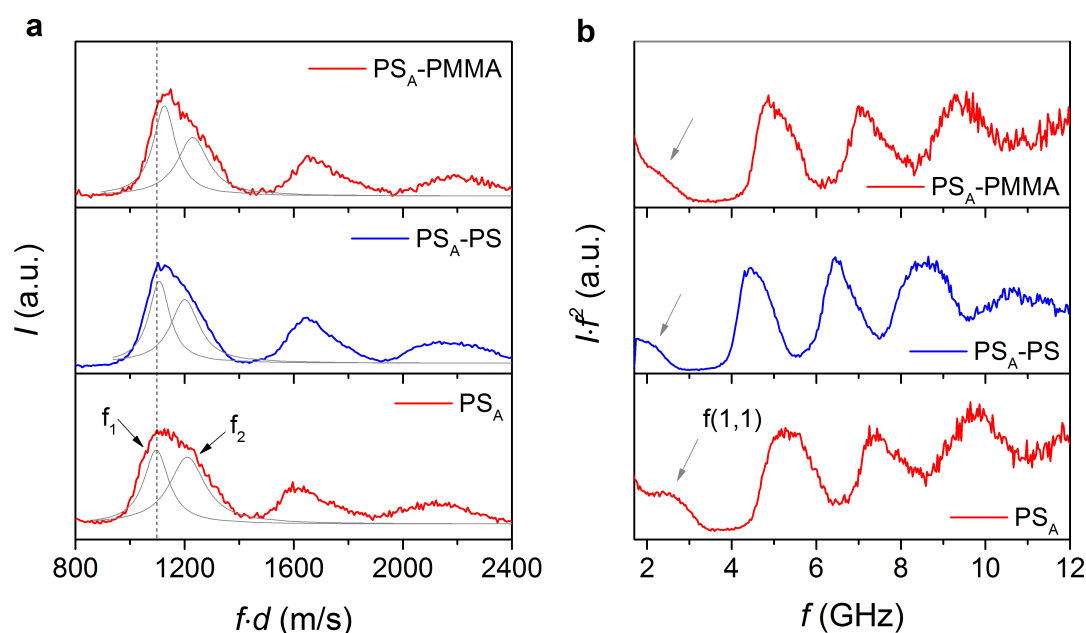

Figure 6.2.1. Brillouin light scattering (BLS) spectra of PS_A, PS_A-PS, and PS_A-PMMA nanoparticles. (**a**) Intensity (I) vs reduced frequency $f \cdot d$ (f is the frequency and d is the particle diameter) of the anti-Stokes side of the spectrum. The two line shapes (solid grey lines) indicate the representation of the (1,2) mode by a double Lorentzian with frequencies f_1 and f_2. The vertical dotted line indicates f_1 for the PS_A nanoparticles. (**b**) power spectra ($I \cdot f^2$) for the three nanoparticles plotted by $I \cdot f^2$ vs f at 294 K. The arrows indicate the interaction induced (1,1) mode.[184]

The BLS spectra of **Figure 6.2.1** reveal information about the intrinsic elastic properties of the nanoparticles and the strength of their interaction governed by the adhesion forces. The BLS peaks correspond to a discrete set of Lamb spheroidal modes which are further affected by the interaction

with the neighboring particles. The particle-particle attractive interactions in a colloidal cluster result in a simultaneous frequency blue-shift and splitting of the particle (1,2) mode (**Figure 6.2.1a**) and appearance of the low frequency (1,1) mode (**Figure 6.2.1b**).[136,137,144,145,147,185,186] This new mode is absent in the vibration spectrum of independent, individual NP's due to its pure translational nature. The interaction-induced changes in the BLS spectrum of independent, individual NPs are schematically shown in the Table of Contents graphic and the close packing (fcc structure) is clearly evident from the SEM images (**Figure S6.2.3**).

The low frequency peak of the split (1,2) branch undergoes a blue shift in the PS$_A$-PMMA NP compared to precursor PS$_A$ NP, as shown by the vertical dashed line in **Figure 6.2.1a**. To estimate the strength of the interaction-induced effect, the eigenfrequency of the (1,2) mode for the three PS NPs, which are based on the same core, PS$_A$, PS$_A$-PS, and PS$_A$-PMMA, are computed using finite element method (FEM) in the absence of interactions between the NP's. In this ideal case, the (1,2) mode corresponds to a single peak at $f(1,2)$ which is computed using a core-shell structure and elastic parameters of the bulk components. The reduced $f(1,2) \cdot d$ value for PS$_A$-PMMA is the same as that for PS$_A$ and the quasi-core-shell, PS$_A$-PS, thus implying a negligible influence of the 8 nm thick PMMA shell layer on the surface mobility (see **Figure S6.2.4**). The effective transverse sound velocity, which can be expressed by $c_t = \sqrt{G/\rho} = f(1,2) \cdot d/A$ with the effective shear modulus (G), the mass density (ρ) of the NP, and the constant ($A = 0.84$ for PS), are directly computed from $f(1,2) \cdot d$.[11] According to the FEM calculations, the PS$_A$-PMMA NP should have the same modulus, $G = 1.5$ GPa, with the precursor PS NP. However, for the former NP, the (1,2) mode appears at higher $f(1,2) \cdot d$ in **Figure 6.2.1a**.

The spitting of the peak and concurrent blue shift of $f(1,2)$ can be attributed to adhesive forces between neighboring particles[12] enabling vibrational modes of individual NPs to resonate with each other. The (1,1) mode is made more distinct by plotting power spectra ($I \cdot f^2$ against f, as shown in **Figure 6.2.1b**). The interparticle adhesion is described by the Johnson-Kendall-Roberts (JKR) model[150] ; the factor f^2 in the power spectra accounts for the thermal population of phonons at $k_B T \gg 2\pi f \hbar$. The position of $f(1,1)$ obtained at the cutoff frequency, where the intensity is 20 % of the maximum peak intensity, agrees well with the scaling law based on the JKR model: $f(1,1) \propto d^{-7/6}$ (see **Figure S6.2.5**) reflecting a similar adhesion energy for all PS based NP's and further justifying the origin of the splitting of the (1,2) mode.[12] The latter renders the calculation of the transverse sound velocity c_t (or shear modulus) from the (1,2) mode less straightforward but the calculation should be able to proceed through the lower f_1 and higher f_2 frequencies of (1,2) doublet (see **Figure 6.2.1a**). We have recently described the (1, 2) peak splitting and shifting behavior under adhesion and presented a new method to compute the shear modulus of NPs in colloidal clusters with the following relation: $f_L(1,2) = 2f_1 - f_2$, where f_L refers to $f(1,2)$ of individual NP in case of no adhesion (see **Table 6.2.3** for computed values).[12] The $f_L(1, 2)$ estimated by this relation provides

quite comparable $f(1,2) \cdot d$ values to the values calculated by FEM, whereas neither lower f_1 nor higher f_2 represent eigenfrequencies of free-standing NPs as shown in **Figure S6.2.4**. Furthermore, the $f_L(1,2)$ reveals an ~8% increase in the shear modulus of PS_A-PMMA in comparison to PS_A and PS_A-PS core-shell NP, as indicated in **Figure 6.2.2**. In the context of the FEM calculations, this higher G value suggests that either PS or PMMA in the core-shell NP should assume slightly higher density and/or c_t than in the core and shell. Given the similar G of PS_A-PS and PS_A NPs, we argue it is the thin layer of PMMA that impacts the elasticity of PS_A-PMMA NPs.
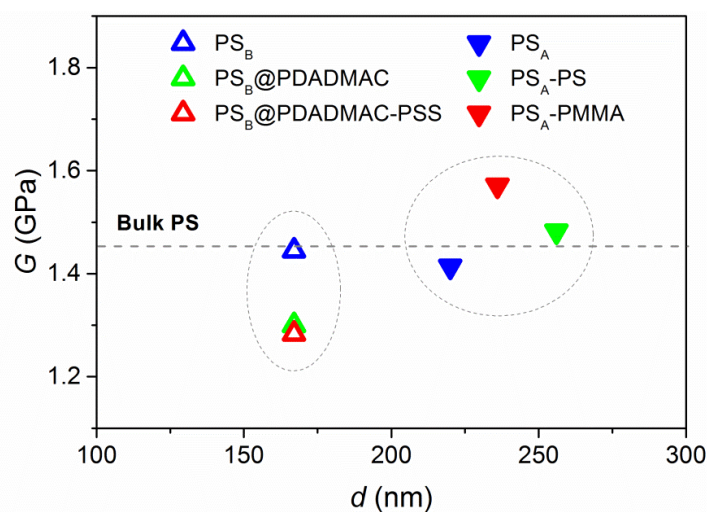

Figure 6.2.2. Shear modulus (G) of PS_A, PS_B, the shell (PS_A-PS, and PS_A-PMMA) and the LbL architecture (PS_B@PDADMAC, and PS_B@PDADMAC@PSS) nanoparticles. The dashed horizontal line indicates the shear modulus of bulk polystyrene.[184]

Table 6.2.3. Characteristic particle vibration frequencies, transverse sound velocity, and shear modulus of chemically bonded and adsorbed polymer core-shell particles

Sample	f_1 (GHz)	f_2 (GHz)	$f_L(s,1,2)$ (GHz)	$f_L(s,1,2) \cdot d$ (m·s^{-1})	c_t (m·s^{-1})	G (GPa)
PS_A	4.98	5.50	4.47	983	1170	1.41
PS_A-PS	4.30	4.68	3.93	1006	1190	1.48
PS_A-PMMA	4.77	5.21	4.34	1023	1210	1.57
PS_B	6.50	7.06	5.95	994	1180	1.44
PS_B@PDADMAC	6.31	6.97	5.64	942	1120	1.30
PS_B@PDADMAC @PSS	6.38	7.16	5.61	936	1110	1.28

To examine the role of the shell structure in determining the mechanical vibrational modes, LbL adsorption was applied to coat one or two layers of polyelectrolyte on PS_B NPs.[176] Two different core-shell NPs were formed using PS_B as the core NP template: (i) one layer of PDADMAC coated atop PS_B (PS_B@PDADMAC) and (ii) one more layer of PSS coated atop PS_B@PDADMAC (PS_B@PDADMAC@PSS). The adsorbed layers were ultrathin as indicated by SEM images (see **Figure S6.2.1** and **Table 6.2.1**). The T_g's of the polyelectrolyte homopolymers depend critically on humidity and storage conditions. For PDADMAC and PSS, the reported T_g ranges from 297 K to 443 K and from 453 K to 484 K, respectively. For the PSS homopolymer's, the T_g is mostly not detectable by DSC and is estimated using the Fox equation.[187–191] **Figure 6.2.3a** and **6.2.3b** show BLS spectra I ($f \cdot d$) and $I \cdot f^2$ (f), respectively for the three NP's. The change in the shape of the BLS spectra is more pronounced than for the shell architecture core-shell NPs, as shown in **Figure 6.2.1**, and the significant split (f_2-f_1) increases with the number of adsorbed layers through a red shift of f_1 relatively to the PS_B NP. Given the negligible thickness of each adsorbed polyelectrolyte layer (1-2 nm/layer) the observed change in the (1,2) mode is quite significant and it might be attributed to an enhanced adhesion between NPs.[176] Interparticle interactions are more pronounced in the frequency of the interaction induced (1,1) mode indicated by the arrows in **Figure 6.2.3b**.
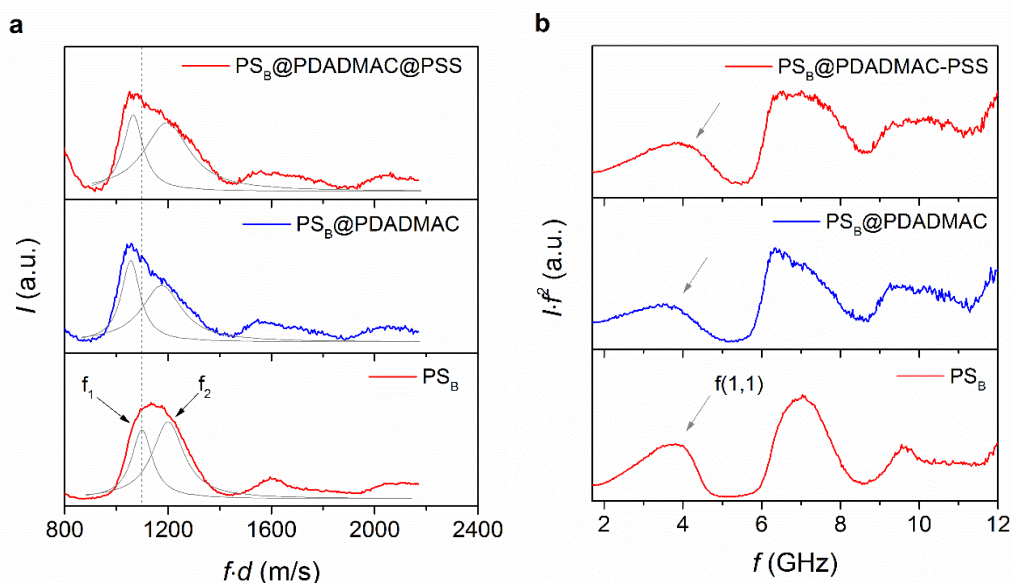

Figure 6.2.3. BLS spectra of PS_B, PS_B@PDADMAC, and PS_B@PDADMAC@PSS. **a** Intensity (I) vs reduced frequency, $f \cdot d$, of the anti-Stoke side of the spectrum. The two line shapes (solid grey lines) indicate the representation of the (1,2) mode by a double Lorentzian with frequencies f_1 and f_2. The vertical dotted line indicates f_1 for the PS_B nanoparticles. **b** Power spectra for the three nanoparticles plotted by $I \cdot f^2$ vs f at 294 K. The arrows indicate the interaction induced (1,1) mode.[184]

Because of the negligible increase in the NP diameter through the adsorption of one or two layers of polyelectrolytes, $f(1,1)$ should be virtually that of the PS_B NP cluster. On the contrary,

$f(1,1)$ systematically increases from PS_B to PS_B@PDADMAC to PS_B@PDADMAC@PSS as better seen in **Figure S6.2.5**. Since $f(1,1)$ is the direct representation of adhesive forces between neighboring NPs, the observed trend corroborates the notion that the existence of a thin polyelectrolyte shell promotes NPs attraction more than that of bare un-coated NPs. It further shows the sensitivity of the particle vibration spectrum to small changes in NP surface modification. However, this strong surface effect does not necessarily imply a change in the NP's shear modulus.

The shear modulus for the PS_B, PS_B@PDADMAC, and PS_B@PDADMAC@PSS can be estimated as previously from $f_L(1,2) = 2f_1$-f_2. The computed shear moduli plotted in **Figure 6.2.2** reveal a profound effect of the physical adsorption of PDADMAC and PSS on the surface of the core PS_B NP; G decreases by about 10 % from that of PS_B NPs. It is a remarkably strong effect in view of the ultrathin adsorbed shell and it could be anticipated from the red shift of f_1 in **Figure 6.2.3a**. We note that an increase of G is observed when a higher modulus shell, i.e., PMMA, is chemically bound to the PS_A core (see **Figure 6.2.2**). We hypothesize that shell structure plays an important role in interfacial mobility and as a result the mechanical properties of the core NPs are tunable by core-shell geometries.

Temperature dependence of surface mobility and mechanical behavior

Temperature-dependent particle vibration spectra allow us to understand not only the thermal relaxation of polymer associated with the NP's T_g but also the surface mobility between T_s and T_g. By means of BLS, the T_g of NPs is indicated by the point where eigenmodes disappear due to the formation of a bulk polymer film. T_s is a characteristic temperature defined from the change of slope in the temperature dependence of both $f(1,2)$ (**Figure 6.2.4**) and $f(1,1)$ (**Figure S6.2.6**). The anticipated red-shift of $f(1, 2)$ (decrease of c_t) with increasing temperature reverses into a blue-shift at T_s (**Figure 6.2.4**) whereas $f(1,1)$ abruptly increases (**Figure S6.2.6**) due to a significant enlargement of the contact area, in spite of no other thermal transition below T_g. This crossover T_s is assigned to the onset of surface mobility,[12] while the bulk of the NP's is still in the glassy state. Because all examined NP's and shells possess very similar T_g (**Figure 6.2.5**), the strong change of T_s is attributed to the surface modification via core-shell and LbL architectures. To exploit the relation of T_s to T_g, the core-shell architecture should involve high T_g contrast between core and shell.

Figure 6.2.4 shows $f(1,2)$ of the shell and the LbL architecture NPs, as well as their precursor core NPs (PS_A and PS_B), at elevated temperatures. Both T_s and T_g of PS_B NP at 338 K and 361 K, respectively, are 5 K lower than PS_A NPs because of a different comonomer used for the synthesis. In the case of the quasi PS_A-PS core-shell geometry, the same chemistries of the shell with the PS_A core consistently provide comparable T_s implying that the polymerization process, necessary for the formation of the shell, does not influence T_s. Moreover, T_g of both PS_A and PS_A-PS NPs are experimentally the same, i.e., 366 ± 2 K. The formation of an 8 nm thick PMMA shell atop core

71

PS$_A$ NPs leads to an increase of T_g for the PS$_A$-PMMA NPs to 371 K. In addition, T_s of the core-shell NPs increased to 360 K, *i.e.*, ~10 K greater that PS$_A$. The increase of T_g for PS$_A$-PMMA NPs could be attributed to either a higher T_g of PMMA[192] and the suppression of surface mobility by the placement of the PMMA shell layer atop the NP. It effectively eliminates the free PS interface and hence the T_g confinement effect,[193] but here it is achieved by a much thinner shell. Moreover, higher T_s of PS$_A$-PMMA than that of PS$_A$ and PS$_A$-PS is observed so it assures the fact that the surface mobility can be significantly reduced by PMMA shell with 8 nm thickness. In contrast, when capping the NPs by the physical adsorption of a polyelectrolyte shell layer, the surface mobility is shown to be strongly affected by the interactive oppositely charged polyelectrolyte layer.
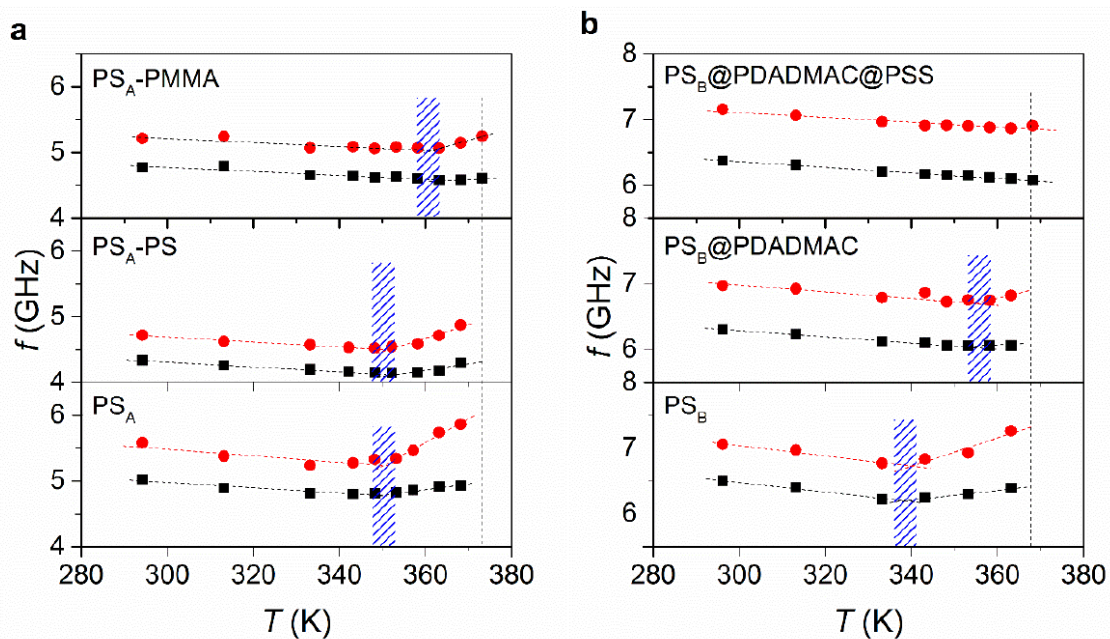

Figure 6.2.4. Temperature dependence of the frequencies f_1 and f_2 of the (1,2) mode (Figure 1a and Figure 3a) of (a) shell and (b) LbL architecture nanoparticles. The vertical hatched areas indicate the position of the softening transition temperature (T_s). The vertical dashed line displays the T_g of core PS$_A$ and PS$_B$ nanoparticles.[184]

As discussed earlier (see **Figure 6.2.3**), a PDADMAC layer capped on the PS$_B$ NP attenuates the surface mobility because anionic surface of the PS$_B$ NP (due to sulfonate groups provided by potassium persulfate initiator) interact electrostatically to the cationic PDADMAC polyelectrolyte.[176,194,195] The surface adsorption of PDADMAC polymer plays a similar role as a surfactant on a NP surface. A surfactant on the surface of NPs suppresses surface mobility, and therefore no T_g nanoconfinement effect has been reported.[7] Similarly, PS$_B$-PDADMAC interactions perturb the PS$_B$-air interface, and as a result, hinder the softening transition at the T_s of PS$_B$. The attenuated surface mobility of PS$_B$@PDADMAC results in an increase of T_s to 358 K. The detection of T_s relates to the presence of adhesive forces in colloidal clusters, as surface mobility activates

adhesive forces between NPs, and the blue shift of $f(1,2)$ with temperature above the T_s is present. Given this, for PS_B@PDADMAC NPs more thermal energy is required to promote adhesion between NPs.

One additional layer adsorption of PSS atop PS_B@PDADMAC NPs (PS_B@PDADMAC@PSS) leads to a further decrease of the surface mobility. Since one or two layers of polyelectrolytes are adsorbed in this study, we assumed that the effect of thermal shrinking or swelling depending on the outermost layer is nearly negligible.[191,196] PSS layer adsorption is based on the interaction with PDADMAC layer and PSS-terminated shell is expected to form a harder shell on the core particle surface than that of PDADMAC-terminated shell.[197] The $f(1,2)$ of PS_B@PDADMAC@PSS shown in **Figure 6.2.4** confirms this complete suppression of surface layer mobility. Below the NP T_g, no T_s is observed, which verifies the fact that the polyelectrolyte layer attached on the core NPs could effectively prohibit the activation of a surface mobile layer even in the presence of stronger adhesion (previous section and **Figure S6.2.5**). The $f(1,1)$ of PS_B@PDADMAC@PSS (see **Figure S6.2.6**) increases to $T = 365$ K which is higher than that of PS_B@PDADMAC ($T_s = 358$ K). Given the fact that PS NPs capped by a hard silica shell showed no T_s, it is confirmed that the shell's interaction with the surface of the core can play a similar role as hard silica capping.[154] Because typical elasticities of a silica shell fabricated by the Stöber method and PDADMAC@PSS multilayer are a few tens of GPa and a few hundreds of MPa, respectively, it corroborates the notion that the suppression of surface mobility is independent of the elasticity of shell structure.[198,199] In the case of the double layers of PDADMAC and PSS polyelectrolyte shell, which is, in terms of the elasticity,[198] even softer than the PS core, complete suppression of surface mobility is achieved by the electrostatically adsorbed soft shell. This independence of surface mobility and elasticity conforms to that of the glass transition behavior of polymer thin films.[200,201] Recalling the fact that the presence of charge surfactants eliminates the T_g confinement effect in NPs,[7] which is consistent with this observation, both cases can be attributed to removed free surface.[8] The mechanism controlling how the charged polyelectrolytes and charged surfactants impede mobility at the surface is not yet fully understood.

The systematic tuning of surface mobility, and thus the T_s, by both chemically and electrostatically fabricated core-shell NPs is shown so far as inferred by BLS. **Figure 6.2.5** shows the T_s and T_g of the polymer NPs. In shell architecture core-shell NPs, their T_s and T_g increase compared to PS_A and the amount of change of these transition temperatures depends more on the chemistries than the thickness of the shell. The robustness of T_s on the addition of 18nm PS shell atop of PS_A core of PS_A-PS indicates that the observed strong T_s increase in PS_A-PMMA NPs is not due to chemistry effects in the interface core-shell; the quasi core-shell PS_A-PS NPs essentially behave like a simply thicker PS NPs. The increase in T_s of PS NPs with the addition of a PMMA shell layer agrees with measurements of freestanding films of PS and PMMA, in which PS exhibits a greater T_s-confinement effect.[122,202] Physical adsorption of polyelectrolytes also affects surface

mobility of the core NP as shown by the strong increase of T_s as more polyelectrolytes are adsorbed (**Figure 6.2.5**, right panel). We note that core-shell NPs based on electrostatic interactions have a greater influence on T_s in comparison to those based on covalent attachment, which is consistent with a greater influence of a charged shell layer on surface mobility reduction.[7,8] These observations corroborate the notion that the shell allows us to tailor the surface mobility of polymer segmental dynamics.
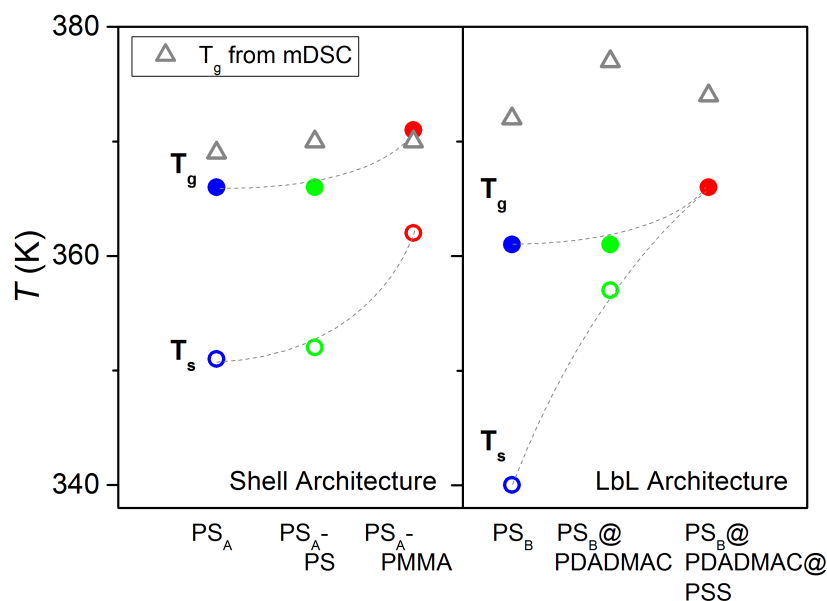

Figure 6.2.5. The effect of a thin shell on the T_s and T_g of core-shell nanoparticles. The T_s (open symbols) and T_g (closed symbols) of the shell architecture (left panel) and LbL architecture (right panel) nanoparticles are shown. Dashed line shows the trend of the T_s and T_g among the NP's The open triangles in the two panels denote the T_g values of all six nanoparticles obtained from modulated differential scanning calorimetry in aqueous dispersions of all six nanoparticles.[184]

The T_g values of NPs measured by BLS are compared with those of MDSC using NPs suspended in water. Both NPs in air used by BLS and in water phase by MDSC are under soft confinement condition so the extent of T_g suppression is expected to be independent for both cases.[129] According to MDSC results in **Figure 6.2.5** (see **Table 6.2.2** for all T_g values measured by BLS and MDSC and **Figure S6.2.7** for MDSC thermograms), the T_g is varied slightly depending on the shell structure. Approximately 5 K higher T_g values of MDSC than those of BLS are consistently observed. This has been reported previously and it was attributed to different physical mechanisms that both techniques are based on; BLS relies on the softening of the elasticity, whereas MDSC measures the relaxation of polymer segments.[12] The softening transition induced by the mobile surface layer is removed by thermal annealing of NPs above their T_g, shown in **Figure S6.2.8**. Forming a contiguous polymer bulk film by annealing above T_g leads to the merging of NPs,

and removal of individual surface layers. The absence of interfacial effects leads to the same T_g in spite of different chemistries of shell structures.

6.2.4. Conclusions

We studied the effect of the shell and its architecture (shell and LbL NP's) on surface mobile layer, elastic moduli, and T_g of polymer NPs using BLS and MDSC technique. By engineering the shell of NPs, we showed that NP elasticity could be tuned via a thin shell structure either by chemically bonded shell or by electrostatic adsorption of polyelectrolytes at room temperature. In addition to this, NPs bearing thin shells revealed the critical impact on thermal transitions of polymeric segments including T_s and T_g. When polymer colloidal films formed contiguous polymer bulk films above the T_g, the T_g values were analogous to the bulk PS T_g due to no interfacial effect of the surface mobile layer. This observation confirmed the notion that the thermomechanical properties of polymer NPs can be tailored by tuning the interfacial effects of surface mobile layer with a core-shell structure, regardless the thickness of the shell. We employed shell structures that show similar thermal transition behaviors with the core PS NPs in this article. Large mismatch of thermomechanical properties between core and shell may provide more dramatic changes in thermal transition and is of great interest to investigate further.

6.2.5. Supplementary information

Synthesis of covalently bonded shell atop a nanoparticle

PS$_A$ nanoparticles (NPs) were synthesized by surfactant-free emulsion polymerization.[203] A three-necked round bottom flask with 240 g of Milli-Q water is connected to a reflux condenser and Ar gas. The flask was heated to 80 °C with stirring speed of 1200 rpm and degassed by argon gas for 30 min. Styrene (St) monomer 3.2 g and acrylic acid (AA) monomer 0.2 g were injected with syringes to the reaction flask. Then, the stirring rate was fixed at 700 rpm. After 10 min, 0.2 g of ammonium peroxodisulfate (APS, $(NH_4)_2S_2O_8$) initiator dissolved in 10 g milli-Q water was injected into the reactor and the reaction was continued for 24 hr.

PS$_A$-PS was synthesized with PS$_A$ core NPs. 50 g of PS$_A$ latex (1.3 wt. % in water) is added in a three-neck round bottom flask equipped with a reflux condenser and argon input for argon condition. The reaction flask was heated up to 80 °C and stirred 700 rpm for 30 min. Then, initiator solution, APS 0.3 g dissolved in 5 g of water, was injected into the flask. Another 30 min later, a mixture of St/AA, 550 µL/29 µL, was fed by a syringe pump with flow rate 414 µL/hr to keep the reaction in monomer hunger state. Reaction was continued for 5 hr.

PS_A-PMMA was synthesized as PS_A-PS NPs were prepared. Instead of the St/AA mixture, methyl methacrylate was used. Methyl methacrylate monomer 621 µL was injected steadily in flow rate 414 µL/hr with a syringe pump to keep the reaction in monomer hunger state. After the injection, reaction was continued for 5 hr to finish polymerization.
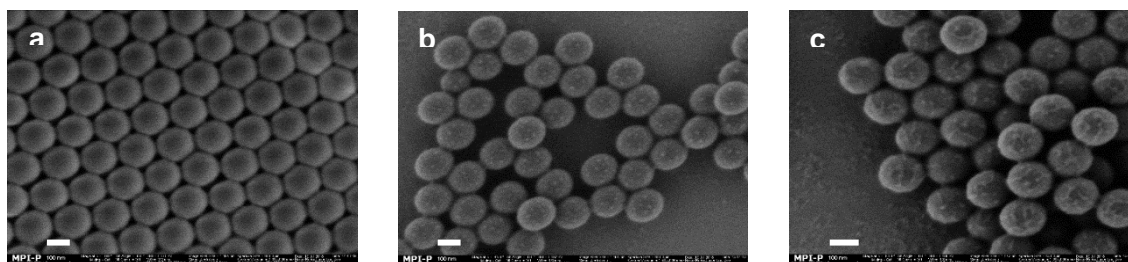

Figure S6.2.1. SEM images of **(a)** PS_B and the LbL architecture **(b)** PS_B@PDADMAC, **(c)** PS_B@PDADMAC@PSS nanoparticles (NP). Scale bar: 100 nm[184]
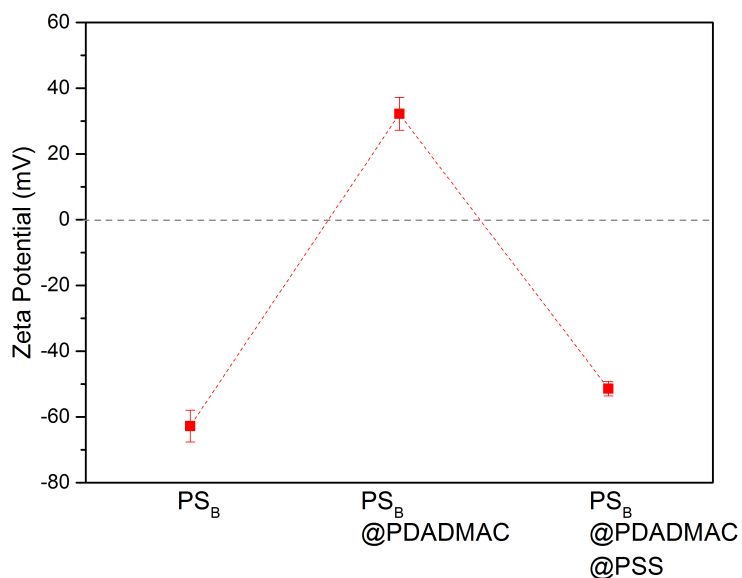

Figure S6.2.2. The Zeta potential for the LbL architecture PS_B@PDADMAC, PS_B@PDADMAC@PSS NP's along the parent PS_B NP.[184]
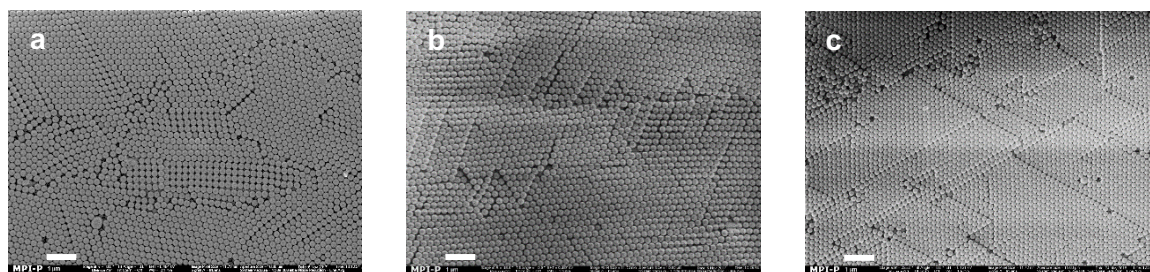
Figure S6.2.3. SEM images of closely packed NP's (fcc) for **(a)** PS_A, **(b)** PS_A-PMMA, **(c)** PS_B NP's assemblies on glass. Scale bar: 1 μm.[184]
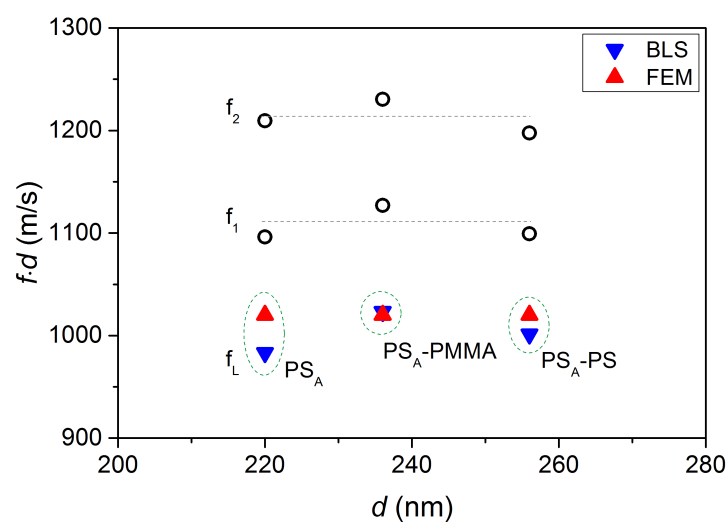

Figure S6.2.4. Reduced frequencies ($f \cdot d$) of the fundamental branch (1,2) of PS_A, PS_A-PS and PS_A-PMMA NP's vs plotted vs their diameter, d. The open and blue solid symbols denote the frequencies f_1 and f_2 of the two Lorentzian lines representing the BLS spectra of **Figure 6.2.1a** and $f_L = 2f_1 - f_2$, respectively. The three red solid symbols denote the $f(1,2)$ computed by finite element model (FEM) for the individual PS_A, PS_A-PS and PS_A-PMMA NP's using the elastic moduli of the bulk PS and PMMA, and the core and shell sizes. The horizontal dotted lines are guide to the eye.[184]
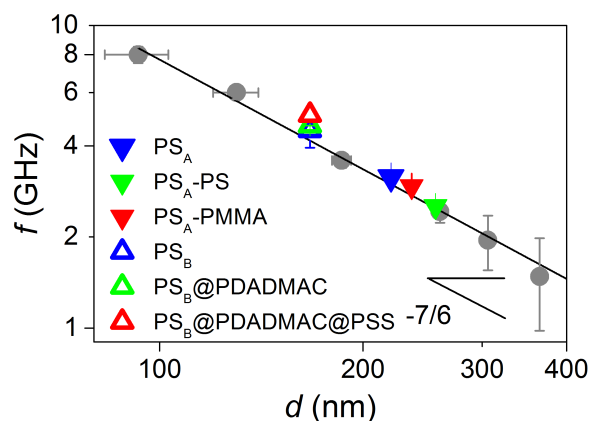
Figure S6.2.5. Double logarithmic plot, frequency of the interaction mode (1,1) vs particle diameter (*d*) for two PS core sizes bearing either covalently bound (*d* = 220nm) or physically absorbed chains (*d* = 167nm).The other data (gray circles) are exported from previously reported publication.[145] Deviation from the solid line (PS$_B$@PDADMAC@PSS) might suggest different adhesion energy.[184]
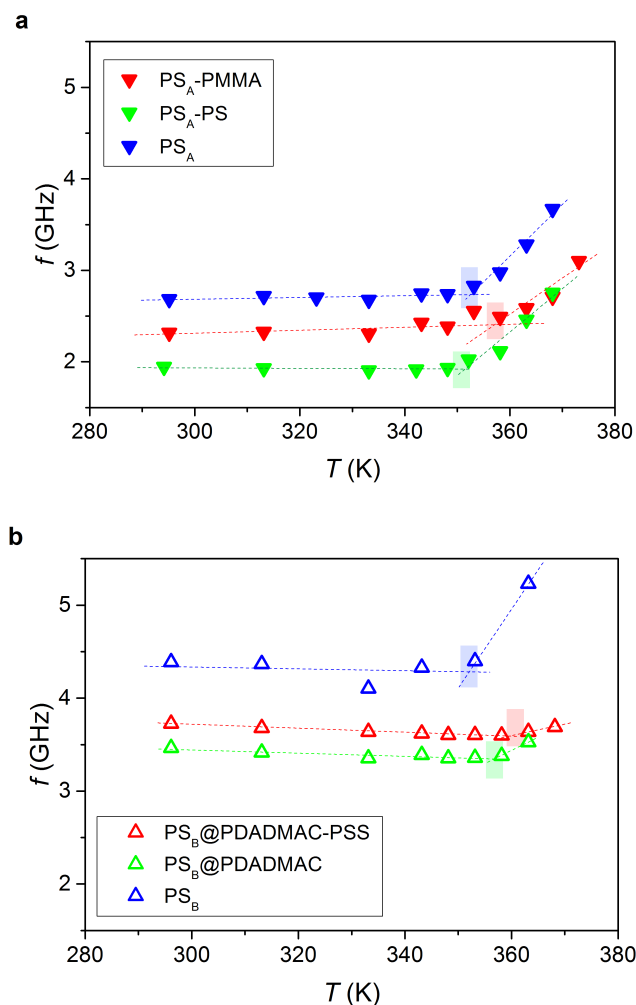

Figure S6.2.6. Variation of *f*(1,1) with temperature of NPs with **(a)** covalently bonded, **(b)** physically bonded core-shell nanoparticles. The vertical slices indicate the softening transition region in the six nanoparticle assemblies.[184]
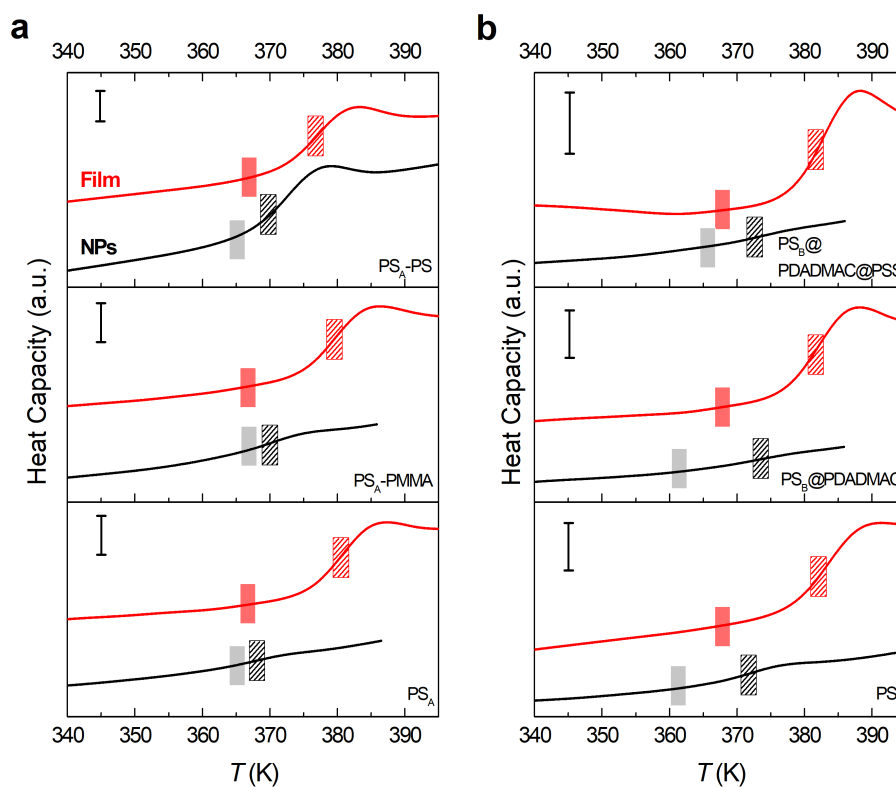
Figure S6.2.7. The modulated differential scanning calorimetry (MDSC) thermograms plotted heat capacity (arbitrary unit) vs. temperature, T (K) both for NPs aqueous state (black solid line) and for annealed bulk state (red solid line); **(a)** covalently bonded and **(b)** physically adsorbed. The filled and dashed areas indicate T_g from BLS and from MDSC, respectively. The black and red areas refer to the T_g of the NPs and that of annealed bulk polystyrene, respectively. Scalebar: 0.2 J/g·K[184]

Figure S6.2.8. Temperature dependence of the longitudinal sound velocity in the contiguous films of the two systems; **(a)** covalently bonded, **(b)** physically adsorbed. The blue border rectangle in each graph displays T_g range of all nanoparticle contiguous films[184]

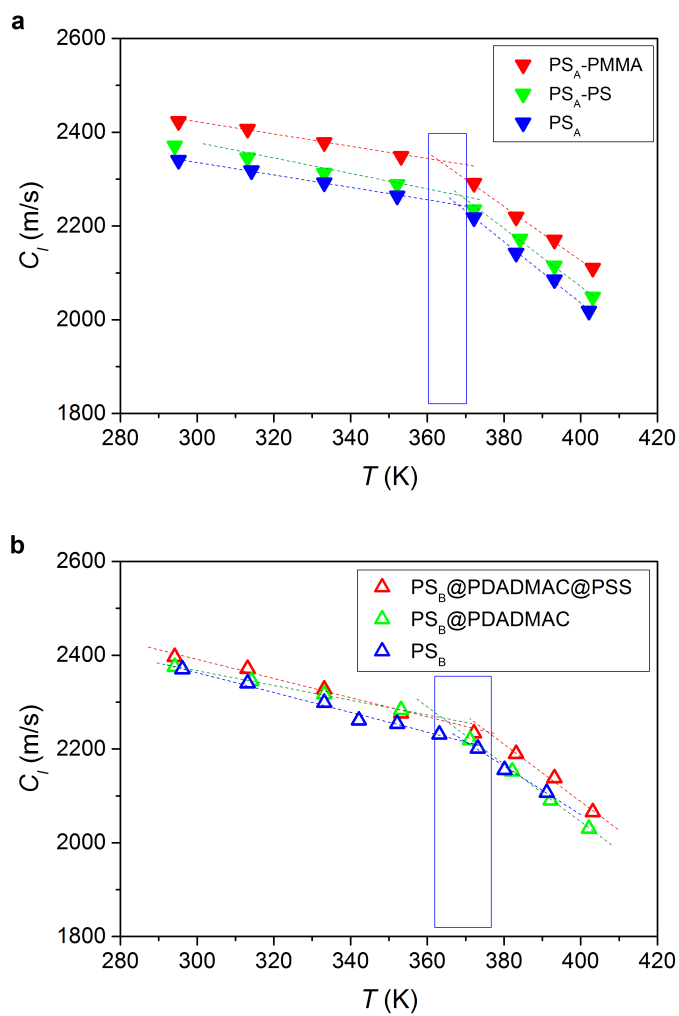## 6.3. Shell architecture strongly influences the glass transition, surface mobility, and elasticity of polymer core-shell nanoparticles

Despite the growing application of nanostructured polymeric materials, there still remains a large gap in our understanding of polymer mechanics and thermal stability under confinement and near polymer-polymer interfaces. In particular, knowledge of polymer nanoparticle thermal stability and mechanics are of great importance for their application in drug delivery, phononics and photonics. Here, we quantified the effects of a polymer shell layer on the modulus and glass transition temperature (T_g) of polymer core-shell nanoparticles via Brillouin light spectroscopy and modulated differential scanning calorimetry, respectively. Nanoparticles consisting of a polystyrene (PS) core and shell layers of poly(n-butyl methacrylate) (PBMA) were characterized as model systems. We found that the high T_g of the PS core was largely unaffected by the presence of an outer polymer shell, while the lower T_g of the PBMA shell layer decreased with increasing PBMA thickness. The surface mobility was revealed at a temperature about 15K lower than the T_g of the PBMA shell layer. Overall the modulus of the core-shell nanoparticles decreased with increasing PBMA shell layer thickness. These results suggest that nanoparticle modulus and T_g can be tuned independently through control of nanoparticle composition and architecture.

6.3.1. Introduction

Nanoscaled polymeric materials are increasingly used in advanced technologies, for example, as separation membranes,[204,205] drug delivery vehicles,[110] reinforcing modifiers,[206] and photonic[207] and phononic crystals.[168] These technologies utilize one-dimensional (e.g. thin films) and three-dimensional (e.g. nanoparticles (NPs)) confinement to modify polymer properties. When the length scale of a polymeric system is reduced to the nanoscale, polymer materials show deviations in physical properties[6,208,209] such as viscosity,[126,210,211] elasticity,[212,213] and glass transition temperature (T_g) from the bulk.[5,119,193,214–219] Although the mechanism behind these deviations is of much debate, interfacial and surface effects dominate confined polymer properties due to the large ratio of surface area to volume.[6]

The influence of polymer-polymer interfaces on T_g of confined polymers remains an open question. Polymer T_g near the polymer-polymer interface has been observed in stacked multilayer films[220–224] and phase separated block copolymers.[225,226] The interfacial width, contrast between bulk T_g values, chain connectivity, and relative Debye-Waller factors may all play a role in determining the change in T_g across a polymer-polymer interface.[226,227] Less well studied is the influence of polymer-polymer interfaces on mechanical properties of confined polymer.[162,212,228–231] Various techniques including buckling,[212] nanobubble inflation,[228] and nanoindentation[230,232] have been used to measure the Young modulus or compliance of polymer thin films both above and

below T_g. Below T_g, both a substantial reduction[212,229] or increase[232] in the Young modulus, depending on the nature of the underlying substrate, has been measured for films with a thickness less than ~40 nm. In rubbery films, above the T_g, stiffening has been observed under nanoscale confinement.[228] While these experiments have been done in a variety of geometries including free-standing films, films supported atop elastomers, and films with and without a topcoat polymer layer supported atop silicon, a thorough investigation of the mechanical properties near polymer-polymer interfaces of confined systems has not yet undertaken. To understand the effect of polymer interfaces on modulus and T_g, we recently introduced PS core-shell NPs with varying ultrathin shells via seeded surfactant-free polymerization and layer-by layer (LbL) adsorption.[184] We found significant change in elastic modulus and thermal behavior of NPs by the introduction of ultrathin shell layers with different chemical composition via Brillouin light scattering spectroscopy (BLS).[184]

Recently, focus has been placed on studying deviations in the glass transition of nanoparticles.[130,4,7,184] Spherical geometries have received less attention partially due to the limited number of experimental techniques available to measure material properties of nanoparticles. Zhang et al.[4] first measured a decrease in T_g (~50 K for ~90 nm PS NPs) prepared by surfactant-free emulsion polymerization. When capped with a silica shell, the T_g confinement effect was absent due to the removal of the free surface.[4] Feng et al.[7] modified PS NPs with different types of surfactants and discovered a strong surfactant effect on T_g deviations for NPs less than 200 nm in diameter, thus emphasizing the importance of the NP surface in determining confinement effects. Furthermore, recent measurements of molecular mobility in NPs[129,233] have shown a decoupling between the decrease in NP T_g with decreasing diameter and no change in the segmental mobility as measured by dielectric relaxation spectroscopy (DRS)[233] and fast scanning calorimetry.[129]

Here, we examine PS core NPs with a low T_g poly(butyl methacrylate) (PBMA) shell layer of varying thickness to understand the effects of the outermost surface and core-shell interface on the thermomechanical properties of the shell. The PS core was synthesized by surfactant-free polymerization. Seeded surfactant-free polymerization was adapted to produce the PS-PBMA and PS-PMMA core-shell NPs. Synthesis of core-shell NPs is elaborated in Supporting Information. BLS with high-resolution tandem Fabry-Perot interferometer was used to measure the elastic properties, particle surface softening temperature (T_s), and T_g. Modulated differential scanning calorimetry (MDSC) was used to measure T_g of the NPs. To understand the influence of the shell layer on the thermomechanical properties via BLS and MDSC, we have also investigated the thermal behavior of contiguous films, prepared by annealing NPs.

82

6.3.2. Experimental section

Preparation of polymer core-shell nanoparticles (NPs)

PS core was prepared by surfactant-free polymerization[203] as a seed for PS based core-shell NPs (PS-PS, PS-PBMA$_7$, PS-PBMA$_{34}$, PS-PBMA$_{58}$, PS-PMMA$_8$, PS-PMMA$_{16}$). For the PS core, styrene and acrylic acid were adopted as a monomer and a comonomer, respectively. Acrylic acid was added to stabilize the particles. For the core-shell structure, each shell (PBMA, PMMA) was polymerized atop the PS core by a two-step surfactant-free polymerization. Different quantities of monomer were used to change the shell thickness. As the shell was grown atop the core particles, some surface activation enabling partially chain grafting to the seed particle surface is conceivable.[234] The growing chain of shell polymers in aqueous media diffuses to the surface of the core and forms a coating structure shell.[235] After the polymerization, unreacted monomer and impurities were removed by a mixture of high purity ethanol and Milli-Q water. Particle dimensional information is listed in **Table 6.3.1**, the detailed NP preparation procedure is in **Chapter 6.3.5**, supplementary information.

Brillouin light scattering spectroscopy (BLS)

BLS experiments were performed for polymer nanoparticle colloids and annealed films in transmission geometry by means of a six-pass tandem Fabry-Perot interferometer. The scattering (acoustic) wave vector $\mathbf{q}$ is defined as $\mathbf{q} = \mathbf{k}_s - \mathbf{k}_i$, where $\mathbf{k}_s$ and $\mathbf{k}_i$ are the wave vectors of scattered and incident light, respectively. In transmission geometry, $\mathbf{q}$ is parallel to the sample plane and of the magnitude $q = (4\pi/\lambda) \sin(\theta/2)$, where θ is the angle between incident light and scattered light. λ is the wavelength of the incident laser light. In our study, we used a laser operating at $\lambda = 532$ nm, fixed $\theta = 90^\circ$ ($q = 0.0167$ nm^{-1}) and vertical-vertical (vv) polarization of incident and scattered light, respectively. A temperature was diversified with a home-built temperature scanning apparatus to see the thermal behavior of nanoparticles.

Modulated differential scanning calorimetry (MDSC)

MDSC, TA Instruments Q2000 was used to measure glass transition temperature of core-shell nanoparticles. The samples were heated at 20 K/min with 0.2 K per 20 s modulation. Before the measurement, nanoparticle suspensions were dried under vacuum at room temperature or annealed at 413 K for overnight into a film.

6.3.3. Results and discussion

Nanoparticle shear elastic modulus

Figure 6.3.1 shows the anti-Stokes side of the BLS spectra of four different close-packed clusters of core-shell NPs: PS-PS, PS-PMMA$_8$, PS-PBMA$_7$, and PS-PBMA$_34$ at 294 K with the particle size information listed in **Table 6.3.1**. For all core-shell NP's, the diameter was obtained from the SEM images averaging the size of one hundred particles randomly chosen. The identification number within the nomenclature represents the thickness of the shell in nanometers and a change in shell volume fraction. In the quasi-core shell PS-PS NP, the thin PS shell layer which has the same chemistry as the PS core, shows negligible effects on the particle elasticity[184] and hence is used as a reference. To compare the spectral features of systems differing both in structure and size, we account for the latter by scaling the particle vibration frequencies by the NP diameter (d). The BLS spectra were then plotted against particle diameter normalized frequency ($f \cdot d$) in **Figure 6.3.1a**. In principle, BLS probes spheroidal mechanical eigenmodes of NPs. The eigenfrequencies of these modes are labeled $f(n,l)$, where n and l are integers defining radial and angular dependence of the displacement, respectively.[145] In order to determine the thermomechanical properties of NP, we focused on the spectral position and line shape of the (1,2) mode. Here, 1,2 stand for the radial and angular vibrations of spheres, respectively.[185] As depicted in **Figure 6.3.1**, in each case the (1,2) modes correspond to Lorentzian doublets (solid gray lines) peaked at f_1 and f_2. The split and blue shift of the $f(1,2)$ with respect to the isolated NPs is the result

Table 6.3.1. Dimensions of shell architecture of PS-based core-shell nanoparticles

Sample	PS-PS	PS-PBMA$_7$	PS-PBMA$_34$	PS-PBMA$_58$	PS-PMMA$_8$	PS-PMMA$_16$
Core diameter[a] (nm)	222 ± 7	220 ± 7	222 ± 7	201 ± 9	220 ± 7	222 ± 7
NP diameter[a] d (nm)	256 ± 6	234 ± 9	290 ± 11	317 ± 12	236 ± 7	254 ± 6
Shell thickness h (nm)	18 ± 3	7 ± 5	34 ± 5	58 ± 6	8 ± 3	16 ± 3
Shell vol. fraction	0.35 ± 0.1	0.17 ± 0.07	0.55 ± 0.1	0.75 ± 0.08	0.19 ± 0.1	0.33 ± 0.1

[a] particle size was measured by SEM images

of attractive interactions between NPs in a colloidal cluster.[136,145,147,12,185,236,237] The (1,2) peak position clearly shifts depending on the chemical composition and thickness of the shell as indicated by the two dashed vertical lines in **Figure 6.3.1a**. For example, $f(1,2)$ of PS-PBMA undergo red shift, compared to the quasi core-shell PS-PS NPs. The blue (red) shift in the spectra implies

stiffening (softening) of the NP modulus. Interestingly, the enhanced modulus of the PS-PMMA core-shell NPs is independent of the PMMA shell layer thickness; see **Figure S6.3.1**(in **Chapter 6.3.5**. supplementary information). For the PS-PBMA NP's, the red shift of (1,2) increases with the thickness of the PBMA shell layer from PS-PBMA$_7$ to PS-PBMA$_{58}$ (**Figure S6.3.1**). This trend reflects a reduction in NP modulus as a function of PBMA shell layer thickness, as discussed in details below.
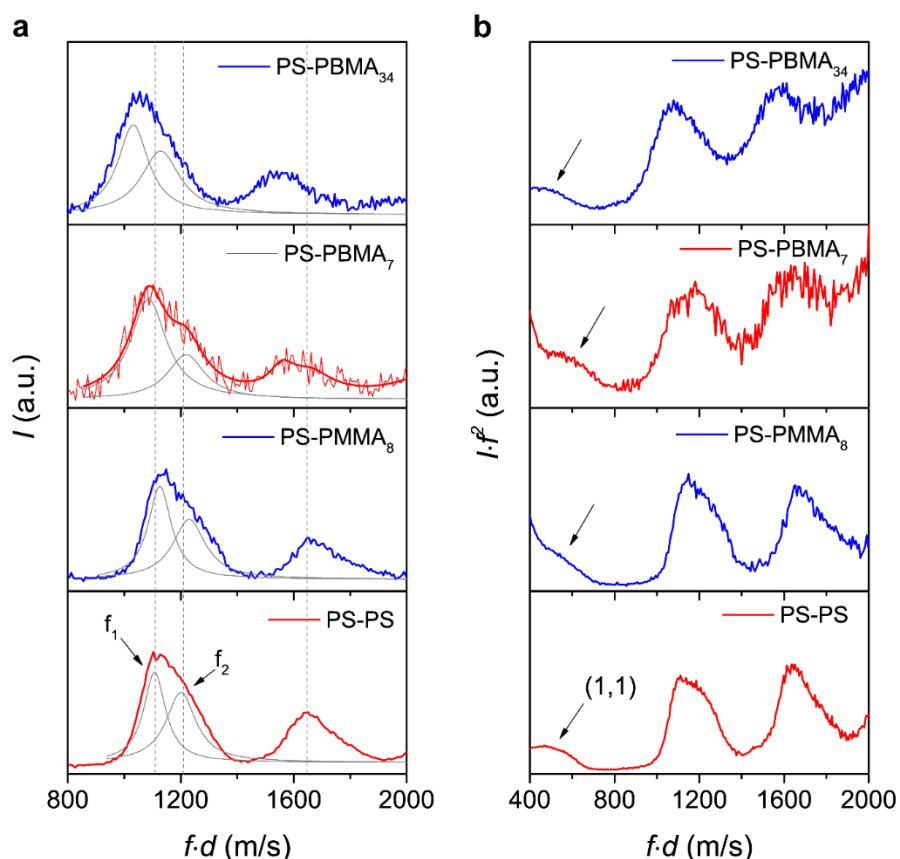

Figure 6.3.1. **(a)** Anti-Stokes side of the Brillouin light scattering (BLS) vibrational spectra of shell architecture PS-PS, PS-PMMA$_8$, PS-PBMA$_7$, PS-PBMA$_{34}$ vs reduced frequency, $f \cdot d$, with d being the particle diameter. The frequencies, f_1, f_2, denote the spectral split of the (1,2) mode and the vertical dotted lines indicate f_1, f_2, and $f(1,3)$ of the PS-PS NPs. **(b)** BLS power spectra, $I \cdot f^2$ vs frequency, f, at 294 K. The arrows indicate the interaction induced (1,1) branch.[238]

To account for the thermal phonon population and better reveal the low frequency side of the BLS spectra near the elastic Rayleigh peak, **Figure 6.3.1b** displays the power spectra $I \cdot f^2$. A clear low frequency peak (arrows) appears in the power spectrum. This (1,1) mode[145] is related to longitudinal phonons in the cluster of the NPs induced by their mutual adhesion, and its frequency $f(1,1)$ can be described by the Johnson-Kendall-Roberts (JKR) model.[150] The precise $f(1,1)$ position is defined at the cutoff frequency in the right tail where the intensity is 20% of the $f(1,1)$ maximum intensity at power spectrum. When this peak position is plotted against diameter, it follows the

scaling $f(1,1) \sim d^{-7/6}$ as shown in **Figure S6.3.2**. While all core-shell NPs follow the scaling because of similar adhesion energy,[12] PS-PBMA$_{58}$ data deviated from the solid line suggesting higher adhesion energy.

We have recently reported that, $f_L(1,2) = 2f_1 - f_2$, can account for the effect of interparticle interactions providing a good approximation of the frequency $f(1,2)$ of the single (1,2) mode of individual NPs ($f_1 = f_2$).[12] To estimate the shear modulus (G), of NPs, the equation, $C_t = f_L(1,2) \cdot d/A = \sqrt{G/\rho}$, was applied.[11] Here, C_t is the effective transverse sound velocity of NPs, d is the diameter, and ρ is density of particles. The value of the Lamb constant, A, which depends on the Poisson's ratio (**Figure S6.3.3**), and for the present case $A = 0.84$ for PS spheres was used. **Figure 6.3.2** depicts G vs shell thickness for the studied NP's (The plot for G vs shell volume fraction is shown Figure **S6.3.4**); C_t and G values for the NPs are listed in **Table S6.3.1**. Note that given the high frequency of the NP vibrations, G refers to the elastic (frequency independent) modulus. As the thickness of the soft PBMA shell increases, C_t and G decrease. In **Figure 6.3.2**, the estimated shear modulus of the NPs is plotted against shell thickness. Based on previous studies,[12,184] particle size does not affect the shear modulus but chemical composition plays a more important role in determining NP shear modulus in homogeneous NP's. PS and the quasi PS-PS core-shell NPs have
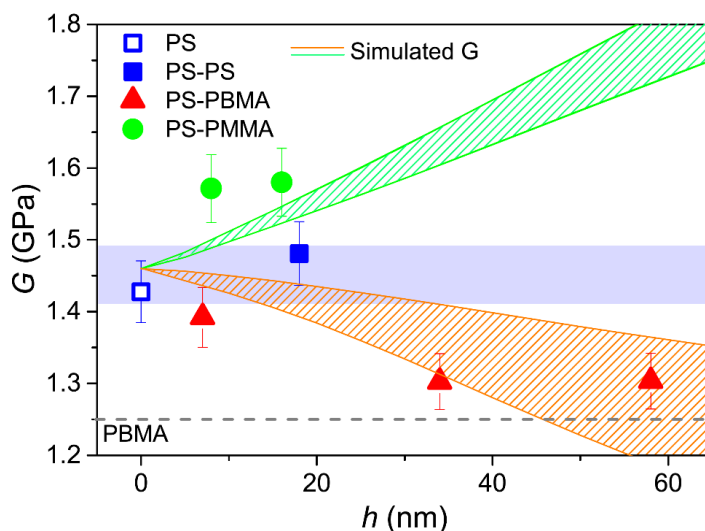

Figure 6.3.2. Shear modulus, G, of PS and core-shell architecture, PS-PS, PS-PBMA group (PS-PBMA$_7$, PS-PBMA$_{34}$, PS-PBMA$_{58}$) and PS-PMMA group (PS-PMMA$_8$, PS-PMMA$_{16}$) NPs plotted against the shell thickness, h. The dashed straight line indicates the shear modulus for the bulk PBMA, while the open square and solid circle refer to the shear modulus of the precursor PS and a PS-PMMA core-shell nanoparticles.[184] The shaded area indicates the maximum error for the modulus of PS. The red and green solid lines indicate the calculated shear modulus for PS-PBMA and PS-PMMA core-shell NPs at constant PS core diameter ($d = 220$ nm) using bulk moduli values for the PS core and two different values for the PMMA ($C_t = 1500$ and 1400 m/s and PBMA ($C_t = 900$ m/s and 1050 m/s) shells. A similar plot for G but as function of the shell volume fraction is shown in **Figure S6.3.4** in **Chapter 6.3.5.** Supporting Information.[238]

similar shear modulus in spite of their different particle size and polymerization process. The shell forming process has no discernible effect on the shear modulus but the chemical composition of the shell can impact the shear modulus of NPs.[184] PS NPs with a high modulus PMMA shell manifest about 10% higher modulus than their precursor PS core even with the addition of thin (8 nm) harder shell layer. The hardening trend is also observed for the PS-PMMA$_{16}$ NP's but is mainly due to the increased of density as the NP's C_t remains virtually constant; there is no significant blue shift for the PS-PMMA$_{16}$, see **Figure S6.3.1**. Compared to PS-PS NPs, a lower shear modulus was revealed for PS-PBMA NPs. The NP modulus decreased with increasing PBMA thickness reaching ~ 12% lower value than PS-PS NPs at 58 nm PBMA shell (see **Figure 6.3.2**). The enhancement of the modulus in the case of the PS-PMMA NP corroborates the notion that a thin shell layer of elastically different material, atop of the PS core, can significantly modify core-shell NP elasticity.

Finite element method (FEM) was used to calculate the shear modulus of the PS-PMMA and PS-PBMA NPs assuming no interactions among NPs and perfect bonding between core and shell interface and bulk elastic properties of each component (see **Figure S6.3.5**). In this case, the (1,2) peak is single in contrast to the interaction induced double spectral shape (see **Figure 6.3.1**, **Figure S6.3.1**, and **Figure S6.3.5**).[12] Using C_t = 1400 m/s for PMMA[149] and C_t = 1050 m/s PBMA, G is presented by the lower green and upper red lines in **Figure 6.3.2**. For PBMA, C_t was obtained from the experimental longitudinal C_L=2200 m/s and using the value 0.35 for the Poisson's ratio. The agreement is only qualitative, since the calculated G overestimates the experimental value of G of PS-PBMA (upper red line, C_t = 1050 m/s) and underestimates the G value for the two PS-PMMA NPs (lower green line, C_t = 1400 m/s). To obtain quantitative agreement between FEM calculations and experiment, the transverse sound velocity C_t for the PBMA shell should deviate from its bulk value. The lower red line in **Figure 6.3.2** corresponds to C_t = 900 m/s being about 15% lower than in bulk PBMA. The deviation between the assumed PBMA shell and PBMA bulk C_t decreases with increasing PBMA shell thickness as indicated by the deviation of the experimental G values from the two red lines. For thinner PBMA shell, PS-PBMA$_7$, C_t (shell) is about 15% lower than in bulk PBMA (1050 m/s), while for PS-PBMA$_{58}$ its elastic G can be captured with the bulk PBMA C_t. In analogy, for the PS-PMMA NPs, a higher C_t (=1500m/s) than for bulk PMMA is required as indicated by the upper green line .

While for colloids there are no other experiments on the elastic modulus, the impact of confinement on the Young's modulus of polymer thin films has been investigated by buckling instability techniques,[212,229,239] AFM,[219,240,241] and a nano-bubble inflation method.[228] A reduction in the glassy modulus has been reported for thin (< 40 nm) PS films atop elastic polydimethylsiloxane (PDMS) substrates, and has been assigned to a free surface layer with reduced modulus.[229,239] An enhancement of the glassy modulus was reported near interfaces, when thin polymer films were supported on hard substrates (e.g. silicon, glass).[219,232,240,241] Quasi-static finite element simulations[241] of the AFM experiment assuming elastic properties of the substrate and the glassy

polymer (PMMA) film indicate stiffening near the rigid substrate. Very recent molecular dynamics simulations[242] have further suggested that the stiffness gradient length scale increases with temperature from below to above the polymer glass transition. Both simulations are based on several elastic and energetic parameters for the polymer interactions with the substrate and the indenter. Hence, the determining factor for either reduction or enhancement of the modulus for film-substrate systems is still unclear. Another system of polymer nanofibers such as PS and Nylon-11 shows dramatic elastic moduli increase as the diameter drops below 200 nm.[243,244] Very recently, the enhanced elasticity in films of polymer tethered nanoparticles at low grafting density was attributed to strong polymer–polymer interactions compared to densely tethered NPs with short chains.[245] For the spherical confinement of **Figure 6.3.2**, the NP shear modulus can be rationalized assuming hardening for the PMMA and softening for the PBMA shell atop of the same PS core.

Nanoparticle surface mobility and glass transition

The sensitive dependence of the (1,2) branch to the NP adhesion was utilized to directly probe the NP surface mobility and identify T_s as the temperature at which a crossover from red to blue frequency shift was observed.[12] It originates from the activation of NPs outermost surface mobility.[12,184] At T_s, the surface of the polymer particles undergoes a glass to rubber crossover. At temperatures above T_s interparticle interactions become activated and thereby increase the contact area between NPs.[12] The resulted reinforced adhesion force is at the origin of the $f(1,2)$ blue-shift above T_s. The presence of a mobile surface layer was firstly reported by whispering gallery modes light localization that revealed negative optical birefringence.[246] The frequencies f_1 and f_2 of the (1,2) branch obtained by the representation of the (1,2) peak in BLS spectra by a double Lorentzian line shape are shown in Figure 3a for the PS-PS, PS-PMMA$_8$, PS-PBMA$_7$, and PS-PBMA$_{58}$ NPs as a function of temperature (see **Figure S6.3.6**). As temperature increases, the first crossover at T_s is indicated by vertical hatched squares. T_s is also resolved in the temperature dependence of the frequency $f(1,1)$ of the interaction induced mode (see **Figure S6.3.7**). With further increase in temperature, the disappearance of the eigenmodes occurs at T_g where the polymer NPs transform in a contiguous film supporting a single acoustic phonon. This crossover from the particle-like vibration spectrum to a homogeneous BLS spectrum is shown in the heat maps of **Figure S6.3.8**. Such maps depict the frequencies (white circles) of the main peaks in the BLS spectrum at each recorded temperature. For the PS-PBMA NP's, no spectral peak was evident in the BLS spectrum recorded in the temperature (dark) region B, as the coalescence of the PBMA shell rendered the resolution of the NP's vibrations impossible. When the sample temperature exceeded this dark region, the sample transforms to a contiguous film and the BLS spectrum displayed only the longitudinal acoustic peak. In the case of PS-PBMA NP's, the incompatibility of the two components preserve the PS cores from merging within the annealed PBMA matrix, as indicated

by the SEM images (see **Figure S6.3.9**). For PS-PS NPs both T_s (= 352 K) and T_g (= 371 K) assume the same values for the PS NPs in our previous work.[184] This indicates that the performed polymerization process, necessary for the formation of the shell does not influence T_s or T_g.
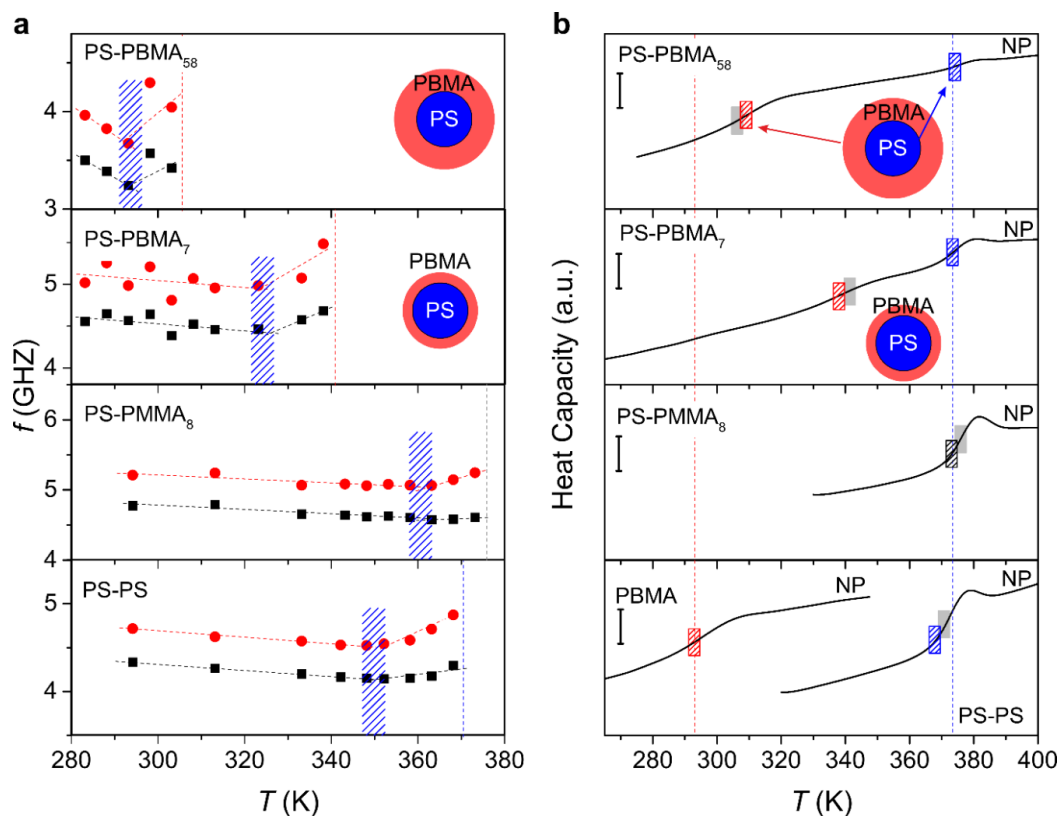

Figure 6.3.3. (a) Temperature dependence of the frequencies f_1 and f_2 for the (1,2) branch in PS-PS, PS-PMMA$_8$, PS-PBMA$_7$, and PS-PBMA$_{58}$ NPs. The vertical hatched squares indicate the softening transition temperature, T_s. The highest temperature at which vibration BLS is still resolved estimates the low glass transition temperature, $T_{g,l}$ of the NPs. T_g, marked with vertical dashed lines. **(b)** MDSC traces of dried powder for the indicated NP's. Shaded and hatched areas indicate, respectively, the glass transition temperatures from the BLS and MDSC experiments. Red and blue hatched areas denote the low T_g ($T_{g,l}$) and high T_g ($T_{g,h}$), respectively.[238]

A thin (8 nm) PMMA shell atop PS NPs causes both an increase of T_s (~ 8 K) and T_g (~ 5 K) compared to PS-PS NPs. As in the case of G, both transition temperatures are robust upon further increase of the PMMA thickness (16 nm) as T_g has already reached the value for bulk PMMA. From the two characteristic temperatures of the NP's, only a single T_g can be measured by DSC as shown in **Figure 6.3.3b**. This T_g assumes the same value in both PS-PMMA$_{8,16}$ NPs in agreement with the BLS and it is indistinguishable, within experimental error, from the glass transition of PS-PS. For PS on PMMA bilayer films[223] experiencing hard confinement next to PMMA (higher T_g than PS) the T_g in the PS domain deviated from the bulk T_g of PS below about 100 nm away from the PS/PMMA interface. A local T_g elevation of about 7 K was reported 25 nm from the PMMA layer but no data exist for PMMA on PS film geometry. The relatively small difference (~15 K) in bulk

T_g between PS and PMMA limits the resolution of possible dynamic asymmetries in the PS core vs PMMA shell. For comparison, $\Delta T_g = T_{g,PS} - T_{g,PBMA} \approx 80$ K between the PS and PBMA components.
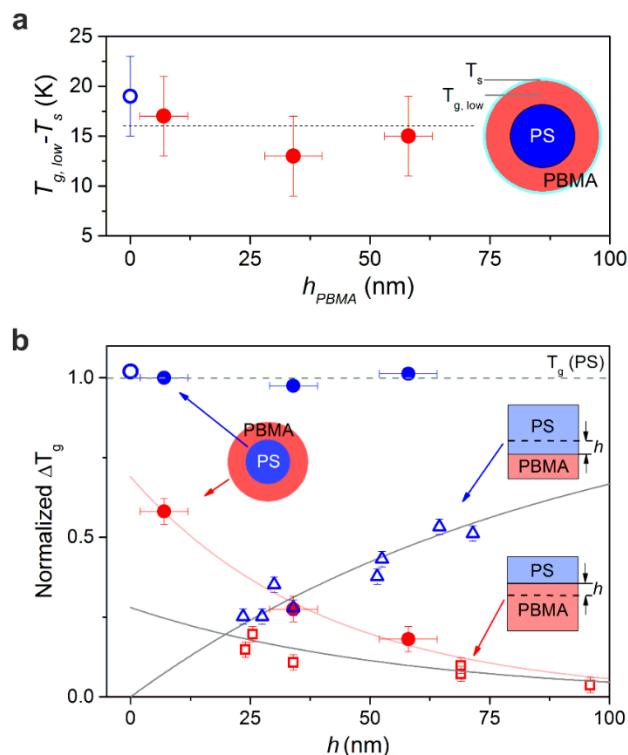

Figure 6.3.4. a) The difference between the low glass transition and the softening transition temperatures for the PS-PS and three PS-PBMA NPs in dependence of the shell thickness, h. b) Normalized glass transition temperature contrast, $\Delta T_g = (T_g(h) - T_{g,PBMA}) / (T_{g,PS} - T_{g,PBMA})$ for the low ($T_g(h) = T_{g,l}$, filled red circles) and high ($T_g(h) = T_{g,h}$, blue solid circles) glass transitions in PS-PBMA as a function of the shell thickness. Note that $T_{g,h}$ refers to the PS core bearing a PBMA shell of thickness, h. Red solid line denotes exponential decay excluding the data point for PS-PS ($\Delta T_g = 1$). To display the actual T_g change, $T_g(h)$ is shown in **Figure S6.3.10** in the Supporting Information (**Chapter 6.3.5**). The comparison with a flat PS/PBMA bilayer film is indicated by the red square symbols for the T_g(PBMA) in PBMA on PS layer, whereas the blue triangle symbols are for T_g(PS) on PBMA layer.[222] h refers to the distance from the PS/PBMA interface.[238]

For PS-PBMA NPs, the large dynamic asymmetry between core and shell revealed (i) strong dependence of both T_s and $T_{g,l}$ (see **Figure 6.3.3a**, **Figure S6.3.6a**) and (ii) a low and high glass transition temperatures ($T_{g,l}$, $T_{g,h}$) (see **Figure 6.3.3b**) on the PBMA thickness as in the case of G (see Figure 4.3.2), but (iii) a robust value for $T_{g,h} = T_{g,PS}$. BLS can access only T_s and $T_{g,l}$ due to the disappearance of the NP vibration at $T = T_{g,l} < T_{g,\,PS}$ (see **Figure 6.3.3a**, **Figure S6.3.6**), whereas DSC probes both glass transitions (see **Figure 6.3.3b**). These characteristic temperatures for all systems are compiled in Table **S6.3.2**. The glass transition enhancement and the relation between T_s and $T_{g,l}$ as a function of the proximity to the PS surface is illustrated in the lower and upper panels of **Figure 6.3.4**. To compare data of different geometry systems, we plot normalized enhancements,

$\Delta T_g = (T_g(h) - T_{g,PBMA}) / (T_{g,PS} - T_{g,PBMA})$, where $T_g(h)$ is either $T_{g,l}$ (filled red circles) or high $T_g(h) = T_{g,h}$ (blue solid circles). To appreciate the actual T_gs changes we have replotted **Figure 6.3.4** as T_g vs h in **Figure S6.3.10**.

The robustness of the PS T_g (solid blue circles in **Figure 6.3.4b**) is an unexpected result in view of the flat PBMA/PS bilayer films. For the latter, the glass transition temperature was determined by fluorescence intensity measurements of pyrene labeled layers (PS or PBMA) inserted at different distance, h, (dashed line in the insets to **Figure 6.3.4b**) from the PS/PBMA interface (solid line in upper bilayer model).[222] The T_g in the PS layer softens with proximity to PBMA interface as indicated in **Figure 6.3.4b** (blue open triangles) and reaches the bulk PS value at about 200 nm far from the interface. Alternatively, the T_g in the PBMA layer is enhanced with increasing distance from the interface but the dependence is weaker than for the PS layer (open red squares). For the spherical geometry, the enhancement of the $T_{g,l}$ in the PBMA shell is stronger than in the corresponding bilayer film (red circles vs red squares) but show as similar trend. The representation of the $T_g(h)$ dependence by an exponential decay (red solid line) cannot describe the initial T_g softening ($h < 8$nm) as indicated by the intercept ($h = 0$) value (< 1). Hence, the glass dynamics appears to reflect a topology effect since in bilayer films the layers are less confined along the direction parallel to the film. The higher T_g of PBMA even at about 60 nm thickness is apparent from the robust surface of PS-PBMA NP compare to PBMA NPs with $T_g = 293$ K.

The huge T_g enhancement effect in the PBMA shell suggests that free surface effects are significantly counter balanced by the influence of the polymer-polymer interface. This is supported by the observation of very similar DSC T_g's in the PS-PBMA NP's and the corresponding contiguous films of PS (cores) in PBMA matrix (no free interface) in **Figure S6.3.11**. This effect mimics that observed in polymer tightly adsorbed on solid interface. Here the effect of free surface is erased by the presence of such adsorbed layer.[247] On the same line of reasoning, we can consider the (soft)polymer / (hard) polymer interface as analogous to that of polymer/hard substrate, where the analogy is marked by the presence of extensive van der Waals interaction involving several pinpoints on each polymer chain, whose effects propagates to the free interface.[242,247–250] However, it is worth noting that polymers in contact with an inorganic interface at best exhibit bulk T_g or only a few degrees higher than bulk. Thereby, the large T_g enhancement observed here may be at least partly explained accounting for the presence of an interfacial mixed layer. The presence of such layer has been demonstrated[251] and, was found to be about 8 nm. This thickness may explain the very large T_g deviation found for PS-PBMA$_7$. The effect of the free (PBMA) surface is, however, evident in the NP's thermal behavior as indicated by the presence of the softening T_s ($< T_{g,l}$). It does relate to $T_{g,l}$ and the difference $T_{g,l} - T_s \sim 15$K seems to be virtually independent of the PBMA thickness as shown in **Figure 6.3.4a** suggesting a constant free surface contribution to T_s.

6.3.4. Conclusion

We synthesized core-shell nanoparticles with a PS core and low T_g PBMA or high T_g PMMA shell layer of varying thicknesses. We used Brillouin light scattering to measure the vibrational frequency spectrum of each nanoparticle type. We found that PS-PMMA core-shell particles exhibited a small, shell-thickness-independent increase in elastic modulus. The elastic modulus of PS-PBMA core-shell particles decreased as the PBMA shell thickness increased. The change in elastic modulus of core-shell particles is not well described by finite-element analysis assuming bulk moduli for each component. Our results are more consistent with modulus hardening in the PMMA shell layer and softening in the PBMA shell layer under the spherical confinement induced by the NP core-shell geometry. Temperature dependent Brillouin light spectroscopy reports the softening temperature as an increase in the vibrational frequency. Additionally, modulated DSC was used to measure the T_g of the nanoparticles. The softening temperature and T_g for PS-PMMA core-shell particles both increased slightly, consistent with the ~5 K higher PS-PMMA T_g than PS T_g. The softening temperature dramatically decreased for PS-PBMA particles with thick shells. Modulated DSC measured two T_gs for PS-PBMA NPs, a low shell-thickness-dependent T_g for the PBMA shell, and a high, constant T_g for the PS core. The softening temperature measured via BLS was consistently ~15 K below the low T_g measured by MDSC suggesting that BLS is more sensitive to the shell of the nanoparticle and that the PBMA shell layer has enhanced mobility at the free surface. However, the PS-PBMA interaction dominates the MDSC T_g measured for the PBMA shell layer. Finally, according to a just appeared article[224] on supported flat bilayer films, the T_g of PS with a rubbery topcoat is affected only for PS thickness below about 60 nm. This is consistent with the unaffected T_g of the PS NP's (d ~ 220 nm) with PBMA shell. In contrast, the T_g of PS on the top of unsupported free- PBMA film[222] is unaffected only for PS thickness above 200 nm.

6.3.5. Supplementary information

Synthesis of PS based core-shell nanoparticles

PS nanoparticles (NPs) were prepared by surfactant-free emulsion polymerization[203] as seeds for PS based core-shell NPs (PS-PS, PS-PBMA$_7$, PS-PBMA$_{34}$, PS-PBMA$_{58}$, PS-PMMA$_8$, PS-PMMA$_{16}$). A three-necked round bottom flask filled with 240 g of Milli-Q water was connected to a reflux condenser and nitrogen (N$_2$) gas. The flask was heated to 80 $^{\circ}$C with stirring speed 1200 rpm and degassed by nitrogen gas for 30 min. 3.2 g of styrene (St) monomer and 0.2 g of acrylic acid (AA) comonomer were injected to the flask. The stirring rate was adjusted from 1200 rpm to 700 rpm and N$_2$ gas flow rate reduced by 0.5 - 1 bubble / 1 sec. After 10 min, 0.2 g of ammonium persulfate (APS, initiator) dissolved in 10 g of Milli-Q water was injected into the reactor. The polymerization was continued for 24 hrs.

92

PS-PS was polymerized with PS core NPs. PS latex 50 g (1.3 wt. % in water) is put in a three neck round bottom flask with a reflux condenser and N_2 input for nitrogen atmosphere. The reaction flask was heated up to 80 $^\circ$C and stirred 700 rpm for over 30 min. Then, initiation solution (APS 0.3 g in 5 g of water) was injected into the flask. Another 30 min later, a monomer mixture St/AA 550 µL / 29 µL, was continuously fed by a syringe pump with flow rate 414 µL/hr. After the feed, polymerization reaction was continued for 5 hr more.

PS-PBMA was synthesized as PS-PS NPs were prepared. Butyl methacrylate monomer is used, instead of the St/AA mixture. Butyl methacrylate (BMA) monomer was injected steadily in flow rate 414 µL/hr with a syringe pump to keep the reaction in monomer hunger state. For PS-PBMA$_7$, PS-PBMA$_{34}$, and PS-PBMA$_{58}$, BMA monomer 585 µL, 1650 µL, 2721 µL was used respectively. After the continuous feed, reaction was continued for 5 hr to finish polymerization.

PS-PMMA follows the same procedure of PS-PBMA NPs synthesis. Methyl methacrylate monomer was used instead of BMA. The amount of MMA for PS-PMMA$_8$, PS-PMMA$_{16}$, MMA monomer 621 µL, 1750 µL were used respectively for shell.

Preparation of samples for BLS

After the polymerization, polymer emulsions were treated to remove unreacted monomer and impurities. When a sample was prepared for BLS, unreacted monomer and impurities between particles interrupt the phonon propagation along the sample. At the first step, the emulsion sample was mixed with high purity ethanol ($\geq$ 99.8 %) 1:1 volume fraction. This mixture was sonicated for 15 min in a sonication bath. Polymer nanoparticles were collected as a pellets by centrifugation at 7000 rpm for 90 min. Then, the pellet mixed with high purity ethanol and Milli-Q water mixture (1:1 volume fraction). Follow the purification procedure twice additionally. At the final purification step, the precipitated polymer nanoparticle pellet was suspended with Milli-Q water. FCC structured polymer particles were obtained by evaporating the aqueous medium from a droplet of the purified suspension on an oxygen plasma treated glass substrate.
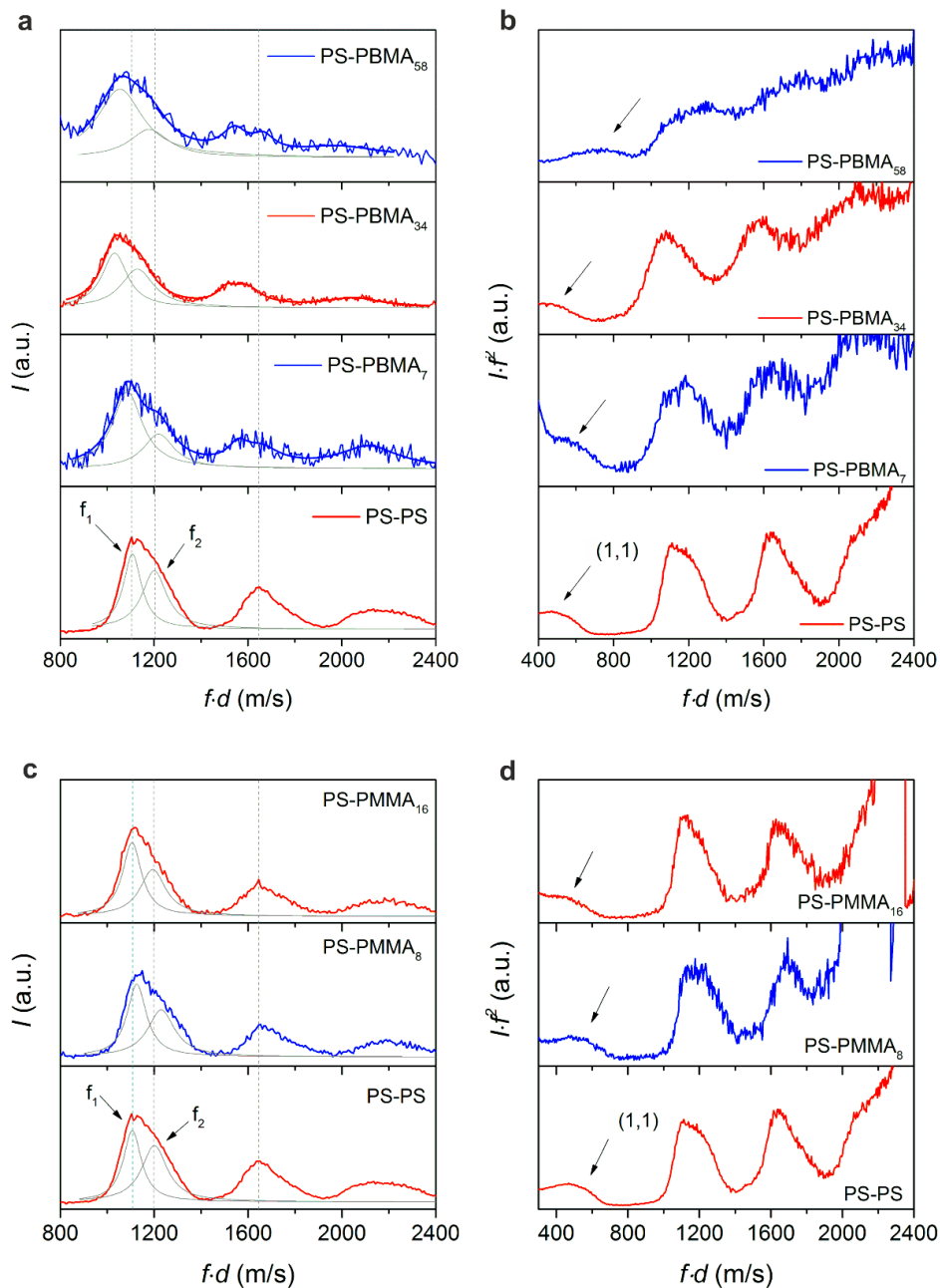
Figure S6.3.1. Anti-stokes side of BLS spectra of **(a)** PS-PS and PS-PBMA group (PS-PBMA$_7$, PS-PBMA$_{34}$, PS-PBMA$_{58}$) **(c)** PS-PS and PMMA group (PS-PMMA$_8$, PS-PMMA$_{16}$) vs reduced frequency, $f \cdot d$, here d is diameter of particle sphere at 294 K. The Lorentzian analyzed frequencies of f(1,2), f_1, f_2, stand for the split of the f(1,2) branch. The vertically dashed lines indicated the f_1, f_2, and f(1,3) of PS-PS NP. Power spectra of **(b)** PS-PS and PS-PBMA group and **(d)** PS-PS and PS-PMMA group, $I(f) \cdot f^2$ vs reduced frequency, $f \cdot d$, at 294 K. The arrows stand for the interaction induced (1,1) branch.[238]
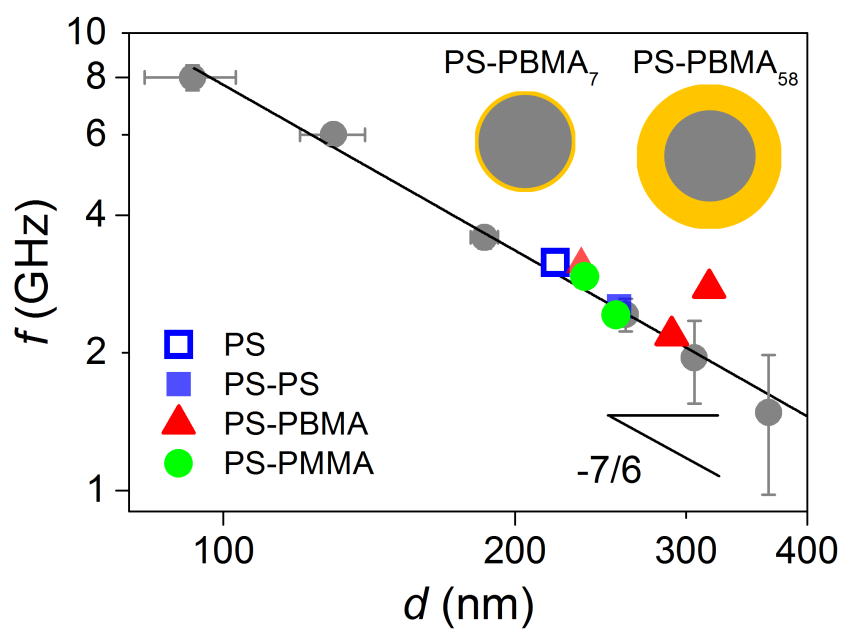
Figure S6.3.2. Double logarithmic plot, frequency ($f(1,1)$) of the interaction mode vs particle diameter (*d*) for PS, PS-PS, PS-PMMA group, PS-PBMA group.[238] The other systens are from Ref.[145]

Table S6.3.1. Characteristic particle vibration frequencies, f_1, f_2, f_L (1,2), transverse sound velocity, and shear modulus for the shell architecture nanoparticles

Sample	f_1 (GHz)	f_2 (GHz)	f_L (1,2) (GHz)	f_L (1,2)·d (m/s)	C_t (m/s)	G (GPa)[a]
PS-PS	4.30	4.68	3.93	1006	1190	1.48
PS-PBMA$_7$	4.56	4.99	4.14	969	1150	1.39
PS-PBMA$_{34}$	3.56	3.89	3.23	936	1110	1.30
PS-PBMA$_{58}$	3.35	3.75	2.94	933	1110	1.30
PS-PMMA$_8$	4.77	5.21	4.34	1023	1210	1.57
PS-PMMA$_{16}$	4.34	4.68	4.00	1017	1205	1.58

[a] error ±2%

Table S6.3.2. Glass transition temperature (T_g) for the PS based core-shell nanoparticles and the films from them by BLS and MDSC. Films for BLS were annealed 413 K overnight, for 14 hrs.

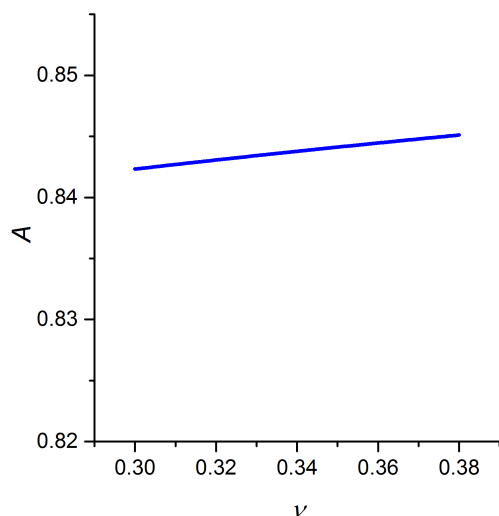| Samples	Particle			Film
	T_s BLS	T_g BLS	T_g DSC	T_g DSC
PS-PS	352 ± 5	371 ± 3	368 ± 1	375 ± 1
PBMA	-	-	293 ± 1	293 ± 1
PS-PBMA$_7$	324 ± 5	341 ± 3	338 ± 1 373 ± 1	338 ± 1 374 ± 1
PS-PBMA$_{34}$	303 ± 5	316 ± 3	314 ± 1 371 ± 1	311± 1 373± 1
PS-PBMA$_{58}$	291 ± 5	306 ± 3	309 ± 1 374 ± 1	307 ± 1 376 ± 1
PS-PMMA$_8$	360 ± 5	376 ± 2	373 ± 1	378 ± 1
PS-PMMA$_{16}$	360 ± 5	376 ± 2	373 ± 1	377 ± 1

Figure S6.3.3. The value of the Lamb constant A as a function of the Poisson's ratio v computed for PS nanoparticles.[238]
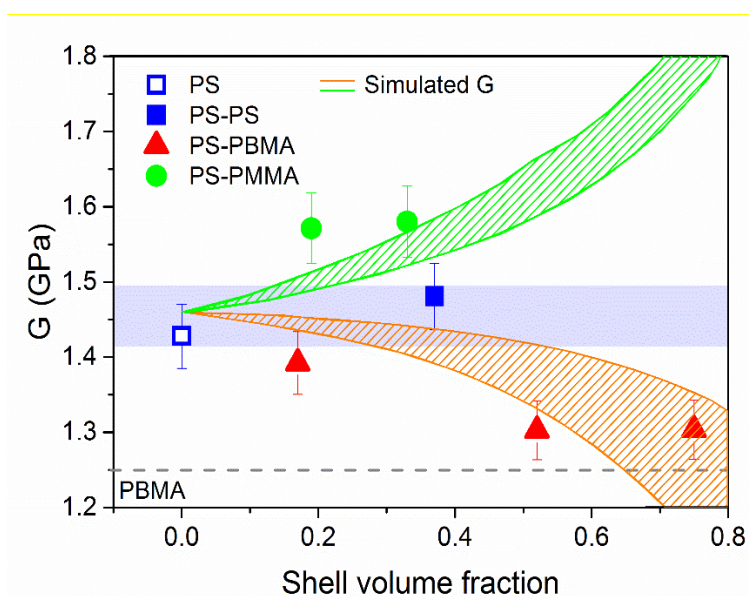

Figure S6.3.4. Shear modulus, G, of PS and core-shell architecture, PS-PS, PS-PBMA group (PS-PBMA$_7$, PS-PBMA$_{34}$, PS-PBMA$_{58}$) and PS-PMMA group (PS-PMMA$_8$, PS-PMMA$_{16}$) NPs plotted against the shell volume fraction to entire particle volume. The dashed straight lines indicate the shear modulus of the bulk PBMA, the shaded area indicates the maximum error for the modulus of PS. The open square and solid circle refer to the shear modulus of the precursor PS and a PS-PMMA core-shell nanoparticles.[184] The red and green solid lines indicate the calculated shear modulus for PS-PBMA and PS-PMMA core-shell NPs at constant PS core diameter ($d = 220$ nm) using bulk moduli values for the PS core and two different values for the PMMA ($C_t = 1500$ and 1400 m/s and PBMA ($C_t = 900$ m/s and 1050 m/s) shells.[238]
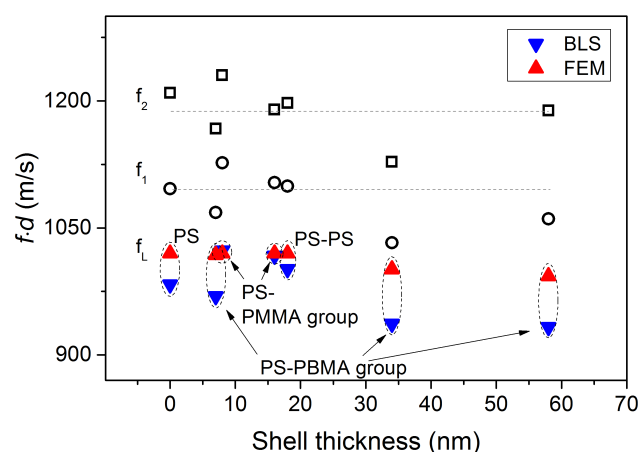
Figure S6.3.5. Calculated from BLS (blue) and Computed (red symbols) from FEM, Normalized *f·d* vs shell thickness for the different core shell particles PS, PS-PS, PS-PMMA group, and PS-PBMA group.[238]
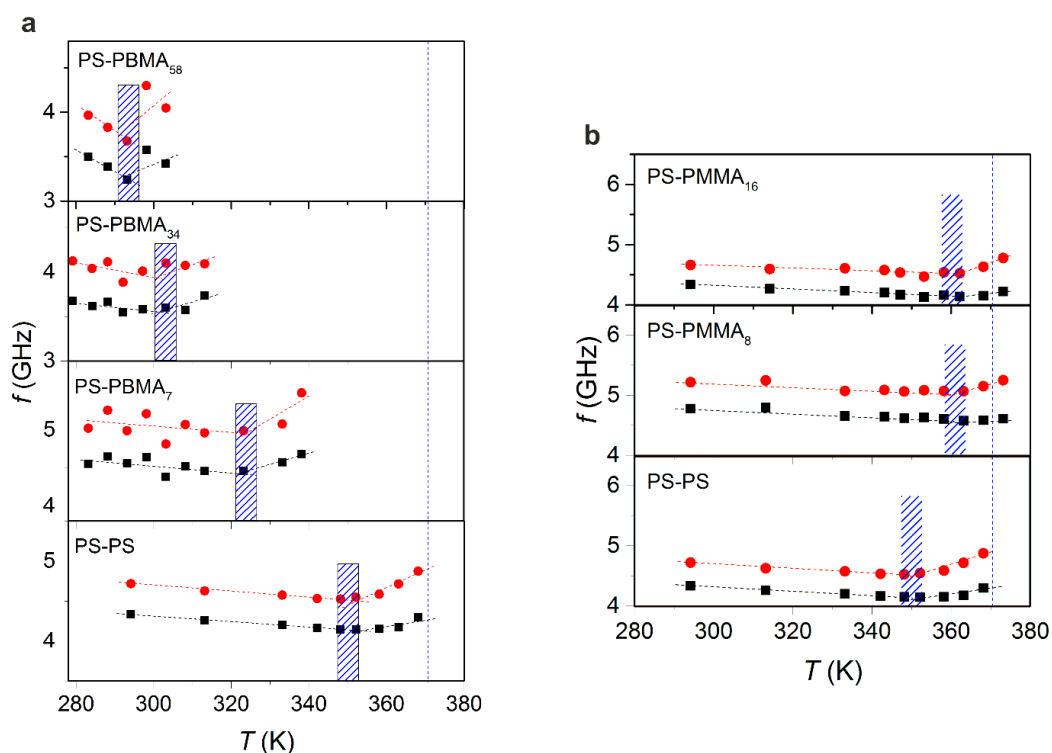

Figure S6.3.6. Temperature dependence f_1, f_2 of the $f(1,2)$ of **(a)** PS-PS and PS-PBMA group, **(b)** PS-PS and PS-PMMA group NPs. The vertical hatched squares denote the position of the softening temperature, T_s of NPs. The highest temperature when vibration BLS f_1, f_2 disappear estimates the NP low glass transition temperature. The vertical dotted lines (blue) denote T_g of PS-PS NPs.[238]
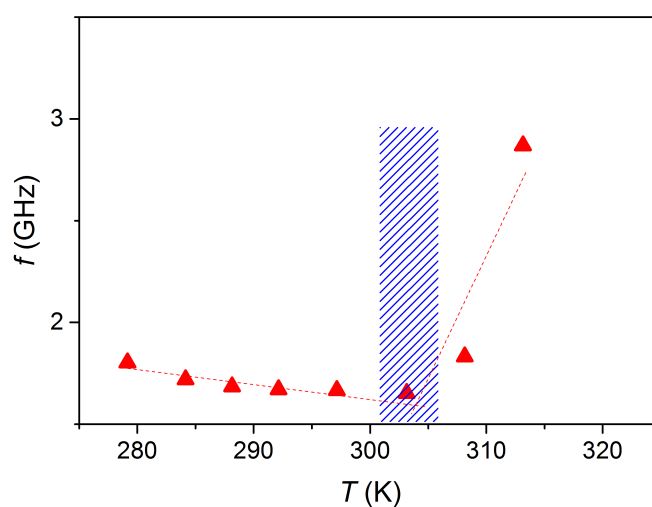
Figure S6.3.7. Temperature dependence of PS-PBMA$_{34}$ $f(1,1)$ The vertical hatched square stands for the position of the softening temperature, T_s of PS-PBMA$_{34}$ NP. The highest temperature, when vibration BLS disappears, estimates the low glass transition temperature of PS-PBMA$_{34}$.[238]
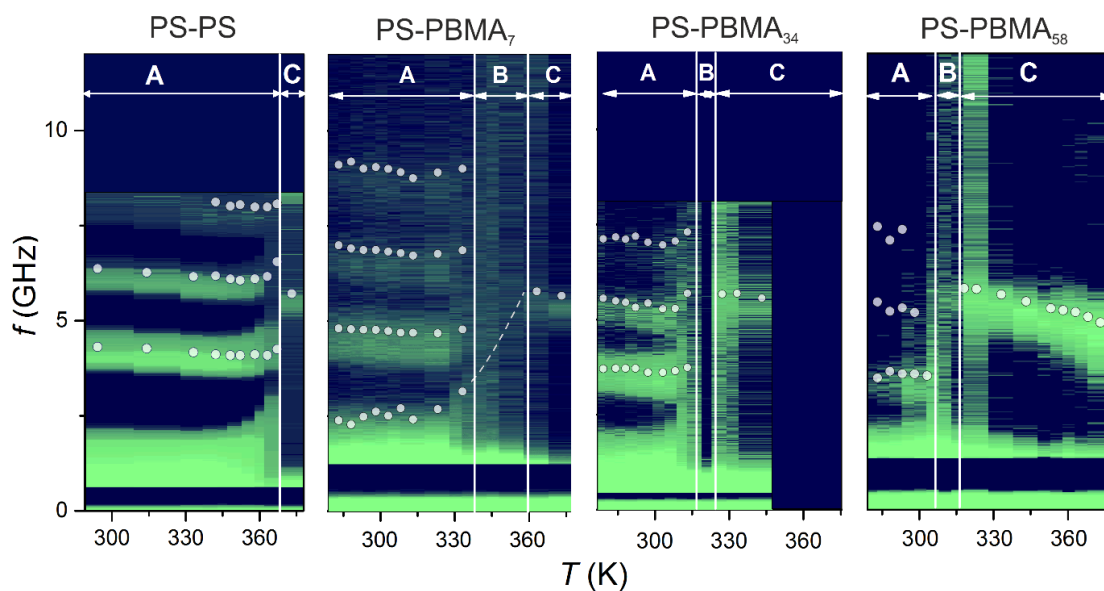
Figure S6.3.8. Heat maps showing the variation of the intensity of PS-PS, PS-PBMA$_7$, PS-PBMA$_{34}$, PS-PBMA$_{58}$ BLS spectral peaks with temperature (each maximum peak marked with a white circle). Vibration eigenmodes are resolved in regime A but are absent in the temperature window B (dark region). Longitudinal acoustic mode in the annealed film of PS-PBMA NPs is observed above the glass transition of PS in regime C.[238]
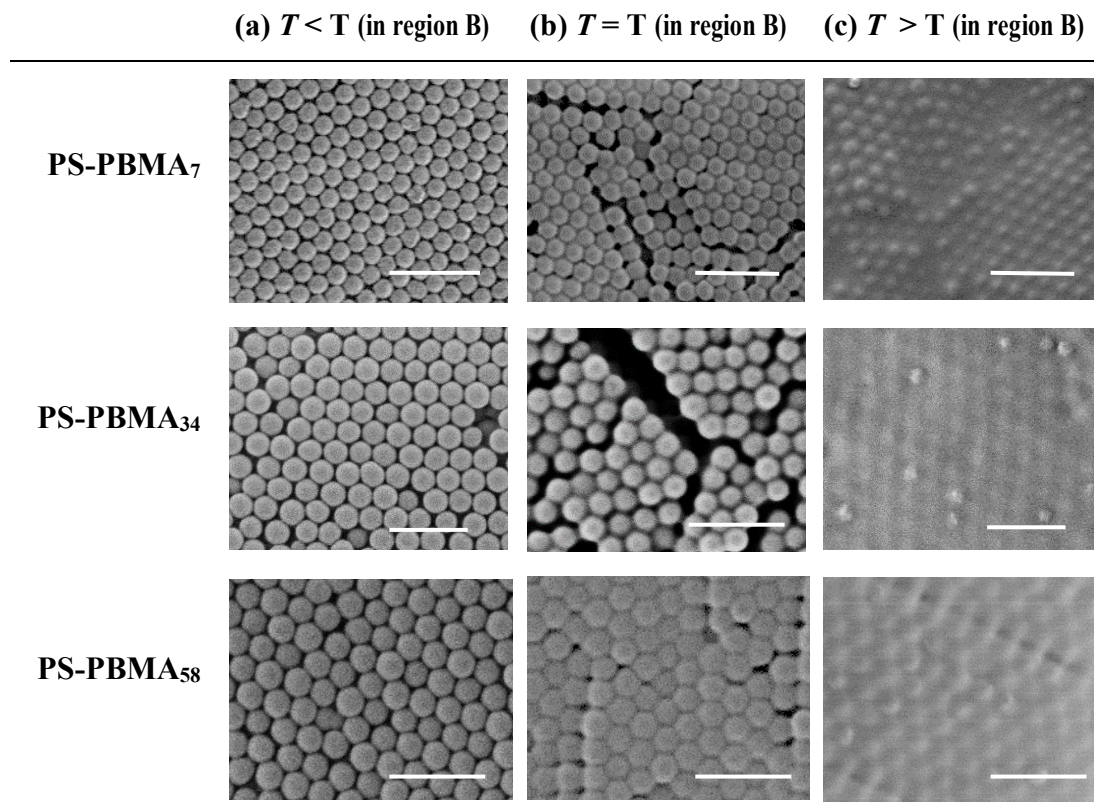
Figure S6.3.9. SEM images of PS-PBMA group particles kept in (a) $T <$ T (in region B), (b) $T =$ T (region B), (c) $T >$ T(in region B) in the oven overnight. Scale bar is 1 μm.[238]

Figure S6.3.10. Glass transition temperature for the low ($T_{g,l}$, filled red circles) and high ($T_{g,h}$, blue solid circles) of PS-PBMA particles. The comparison with a flat PS/PBMA bilayer film is indicated by the red square symbols for the T_g(PBMA) in PBMA on PS layer, whereas the blue triangle symbols are for T_g(PS) on PBMA layer.[222] h refers to the distance from the PS/PBMA interface.[238]

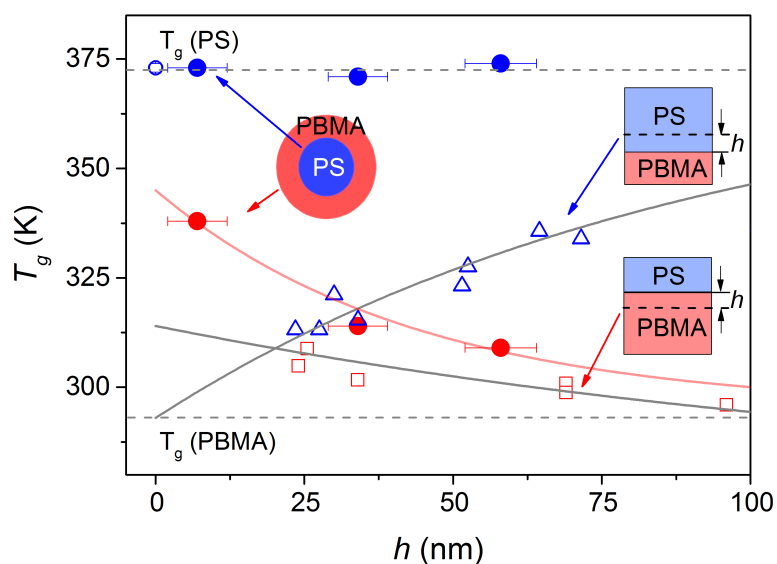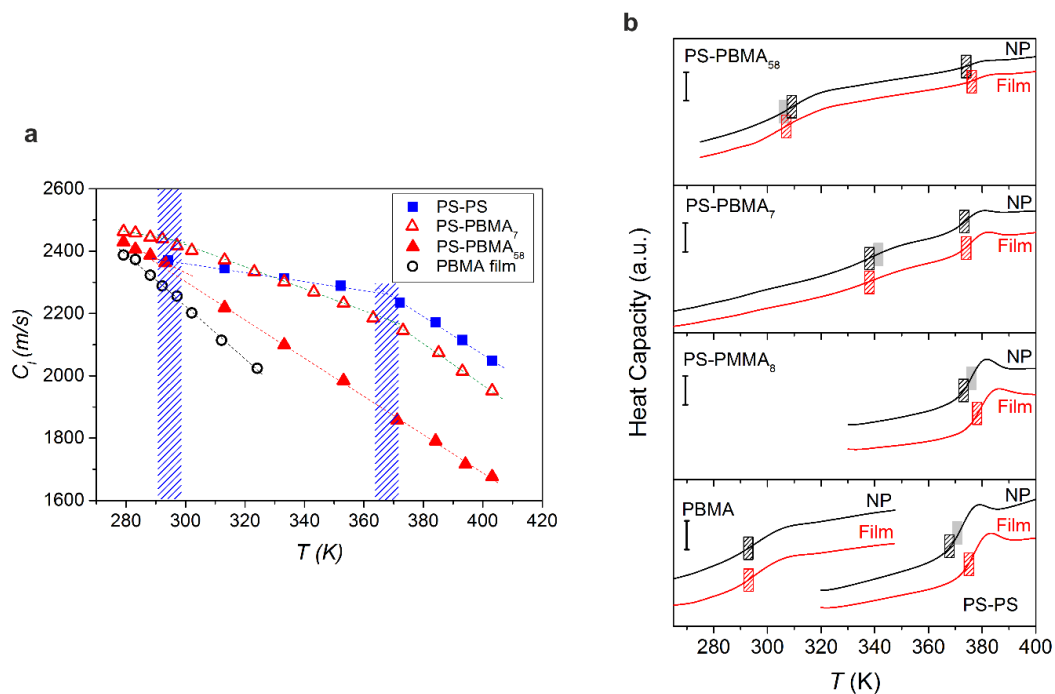**Figure S6.3.11**. a) Temperature dependence of the longitudinal sound velocity, C_L, with annealed films (PS-PS, PS-PBMA$_7$, PS-PBMA$_{58}$). The vertical hatched areas indicate the T_g and its error of PS-PS and PBMA films from BLS. b) The modulated differential scanning calorimetry (MDSC) thermograms plotted heat capacity (arbitrary unit) vs. temperature, T (K) both for NPs (black solid line) and for annealed bulk film (red solid line). The filled and dashed areas indicate T_g from BLS and from MDSC, respectively. The black and red areas refer to the T_g of the NPs and bulk films. Scale bar: 0.25 J/g·K [238]

Chapter 7. Conclusions and Outlook

Through my Ph.D. work, the non-contact and non-destructive Brillouin light scattering (BLS) method has been applied to estimate the elastic moduli and probe the thermomechanical behavior of colloidal particles by probing particle elastic vibrations. The first goal was to observe thermally excited phonons in nanoparticle crystals and thereby investigate particle interactions and elastic properties. Polystyrene (PS) nanoparticles (NPs) with different sizes (diameter between 141 nm and 707 nm) and compositions (different co-monomers or crosslinkers) were prepared by surfactant-free emulsion polymerization (SFEP). SFEP is a well-known polymerization method which does not require the addition of surfactants and avoids thus such contaminations in the resulting particles. However, also for this method a purification process is required to remove amphiphilic polymer chains physisorbed to the particle surfaces, in order to fabricate appropriate samples by colloidal assembly for BLS characterization. The remained unreacted co-monomer and mobile amphiphilic oligomers can disturb phonon propagation in the sample (see appendix in **Chapter 8.2.**). Especially, the vertical lift deposition (VLD) sample strongly showed this effect in unpurified samples when it was compared to the drop evaporation sample. During the VLD process, colloidal assemblies continuously form at the air-water-solid interface. Therefore, remaining water-soluble polyacrylic acid (PAA)-rich amphiphilic oligomers from the polymer NPs dispersion is constantly supplied from the liquid phase to the forming particle assembly and accumulates between PS NPs after drying. Otherwise, for the drop evaporation method, a PS NPs dispersion droplet forms on a glass substrate. The remained PAA-rich polymer fraction in the dispersion accumulates at the ring edge of the droplet during the dry process because of the coffee strain effect. Therefore, all PS NPs colloidal assembly samples were prepared after the purification process.

The particle vibration spectra of the PS NPs demonstrate distinctive elastic properties and thermomechanical behavior. In particular, temperature-dependent BLS revealed an anisotropic thermal response of the NPs due to the presence of a surface mobile layer and glassy core. In addition, PS NPs with different surface roughness were examined to see the roughness effect on elastic moduli of the NP. The PS NPs with rough and smooth surfaces were provided by Prof. Duits group (University of Twente). The acoustic vibration of PS NPs with different surface roughness showed no difference (see appendix in **Chapter 8.3**.).

To investigate the surface mobile layer effect on physical properties, tuning of the colloid architecture was the next step. This was achieved by chemical and physical methods: (i) chemically bonded groups (by two-step surfactant-free polymerization), (ii) physically adsorbed groups (by layer-by-layer adsorption method) led to PS NP systems with thin shells (8 ~ 18 nm for chemically bonded groups, 1 ~ 2 nm for physically adsorbed groups) atop the PS core. By tailoring the shell on the PS core, the NP elasticity can be tuned at ambient conditions and NPs with thin shells displayed a pronounced change in both softening T_s and glass transition, T_g, temperatures.

Elimination of free surfaces by forming contiguous films above T_g, the bulk PS T_g is recovered. This result confirmed that the thermomechanical behavior of polymer NPs can be tuned by engineering the surface mobile layer of NPs with a core-shell structure.

To exploit the effect of the shell thickness on the thermomechanical properties of core-shell particles with T_g contrast was introduced. Therefore, core-shell structures with a PS core and low T_g poly(n-butyl methacrylate) (PBMA) or high T_g poly(methyl methacrylate) (PMMA) was prepared by two-step surfactant-free emulsion polymerization. For the low T_g contrast PS-PMMA core-shell NPs, displayed a subtle layer effect. For the high T_g contrast PS-PBMA core-shell NPs, the PBMA shell thickness impacted both elasticity and NP dynamics. The shear modulus of the NPs decreased, whereas the elevation of the PBMA T_g dropped with the PBMA shell thickness. Expectedly as the PBMA thickness increased, the T_g value of the shell approached the bulk PBMA T_g. Due to the coalescence of the PS-PBMA NPs at temperatures above the PBMA T_g, the high T_g for the PS core was inaccessible by BLS measurements. The intriguing findings on the thermal properties of the core-shell NPs were supported by modulated differential scanning calorimetry (MDSC). MDSC provided two T_g values, one being very close to the PBMA T_g from BLS and the second higher T_g was for the PS core. The T_g of PS core was found to be independent of the PBMA shell thickness. The thickness dependent PBMA T_g suggested a competing open surface and PBMA-PS interface effect in close analogy to PS and PBMA bilayer film.[222]

The results from my Ph.D. research suggest three new research directions related a) to the confinement and the interface effect, b) the influence of surfactants for interfacial control and c) the non-contact impact of NP vibrations. The confinement effect originates from the surrounding shell and it suppresses the influence of the core T_g. Hence the hardening interface effect depends on the shell thickness. Therefore, the inverse core-shell structure with low T_g core (PBMA) and high T_g shell (PS) is proposed. This research will provide important information on the role of the dimensionality (3D core-shell structure vs 2D bi-layer structure). To control the interaction between the particles the use of surfactants is suggested. Recently, Wang *et al.*,[252] discovered that structured clusters of PS NPs can be fabricated from the emulsion droplet mixed with polymeric surfactants in a microfluidic device. The evaporation time influences the particle interaction and can lead to different shaped clusters. The controlled accumulated effect of interactions should be manifested in the vibration spectrum of the NP cluster. The non-contact transmittance of NP vibrational motion in a polymer matrix should depend on the distance and the elastic contrast. A promised system is plasmonic NP's (e.g. Ag, Au), either dispersed in polymer matrix[253] or grafting the polymer on the NP's. In additional to the fundamental (*s*,1,2) mode a low frequency mode should monitor the non-contact interactions.

Chapter 8. Appendix

8.1. FEM simulation for eigenmodes of nanoparticles

Chapter 8.1 is added to show each vibration mode schematically as a supplement. All experimental conditions and results originate Tim Still's dissertation.[254] **Figure 8.1** shows the finite element method (FEM) displacement fields of polystyrene (PS) nanoparticles (NPs) with $d = 540$ nm. For FEM, same PS parameter were used ($c_L = 2350$ m/s, $c_t = 1200$ m/s, $\rho = 1050$ kg/m^3). The total local displacement is illustrated in the color scale. The each eigenmode of the PS NP ((1,2), (1,3), (1,4), (1,5), (1,6), (1,7)) of PS NP are shown from (a) to (f), respectively.
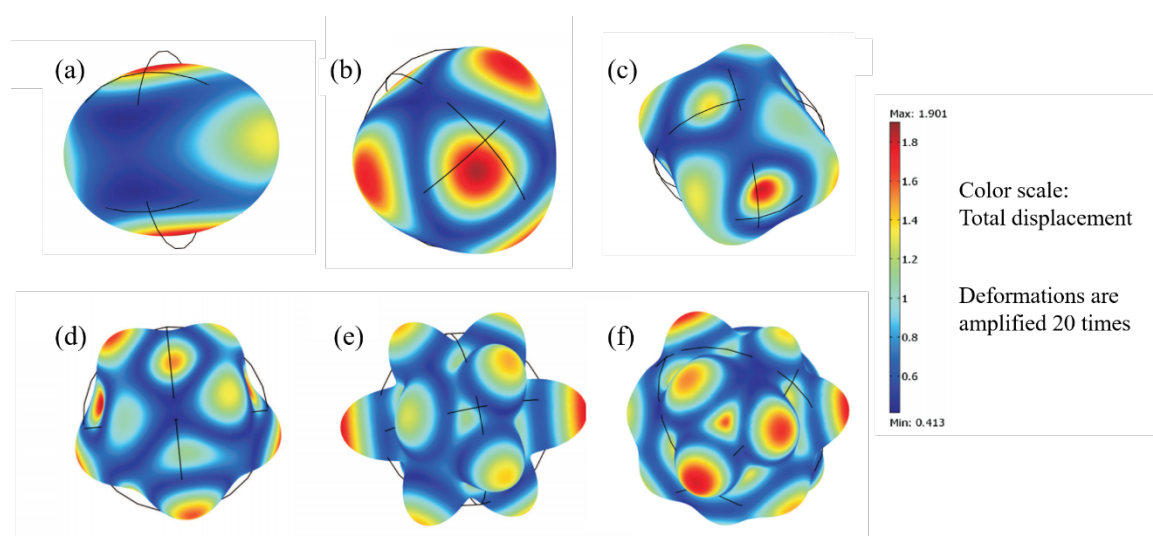

Figure 8.1. FEM simulation for the vibrational eigenmodes of a PS NP ($d = 540$ nm). From **(a)-(f)**, each eigenmode of the PS NP, (1,2), (1,3), (1,4), (1,5), (1,6), (1,7) is illustrated respectively. Displacement is illustrated with a color scale, and the deformation of the surface is amplified by 20 times. The schematic FEM results are from the original reference[254].

8.2. Purification effect on BLS spectrum

The purification process after polymerization is important to remove unreacted monomers and impurities from the dispersion. After the surfactant-free polymerization process, the dispersion of poly(styrene) (PS) was mixed with high purity ethanol (≥ 99.8 %) and Milli-Q water 1:1 volume fraction. The mixture was sonicated over 15 mins. PS NPs were collected by centrifugation at 7000 rpm for 90 mins. Then the collected NPs dispersed with the ethanol and the Milli-Q water mixture (1:1 volume ratio). The purification cycle was conducted two times more. At the final step, the pellet of PS NPs dispersed with Milli-Q water.
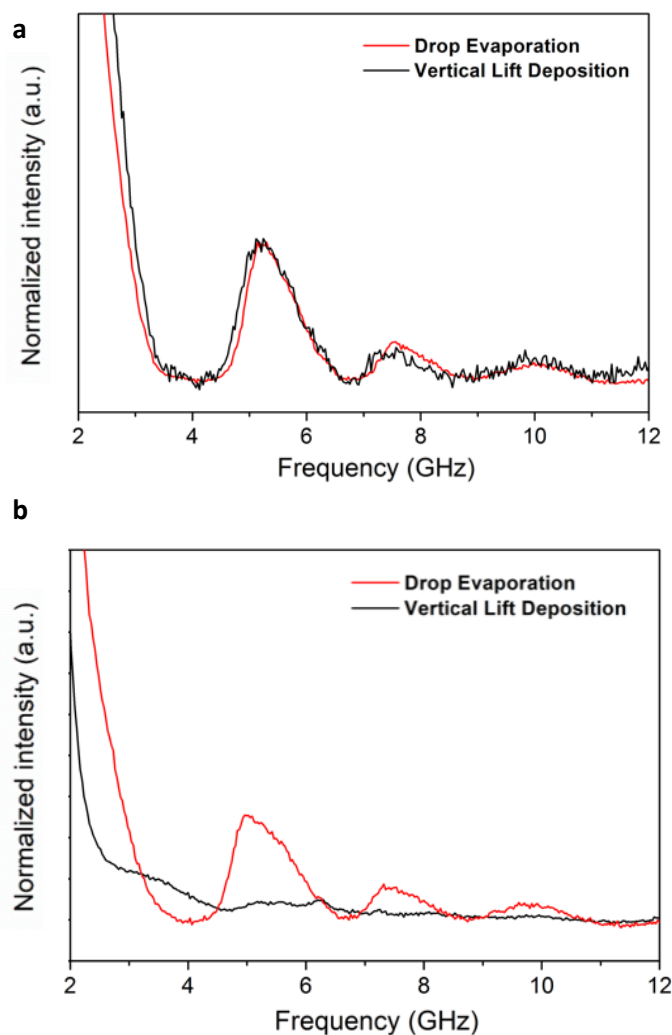
Figure. 8.2. Anti-stokes side of Brillouin light scattering (BLS) spectra (*I* vs. *f*) of drop evaporation (DE) and vertical lift deposition (VLD) sample of **(a)** purified polystyrene (PS) nanoparticles (NPs), **(b)** unpurified PS NPs.

For drop evaporation, the aqueous medium was evaporated from a droplet of unpurified and purified PS NPs suspension on oxygen-plasma treated glass substrates. For vertical lift deposition (VLD), oxygen-plasma treated glass substrates were used. The substrates dipped in the unpurified and purified PS NPs dispersions and lifted vertically with 1000 nm /sec in a humidity-controlled chamber. The temperature and humidity of the chamber were 60.0 $^{\circ}$C and 80.0% respectively.

The BLS spectrum of purified polystyrene (*d* = 202 nm) NPs in **Figure 8.2a**, it shows clear *f*(s,1,2) mode around 5.5 GHz for both methods of drop evaporation and VLD. However, in the case of unpurified PS NPs in **Figure 8.2b**, the VLD method does not show clear *f*(s,1,2) mode when it is compared to the drop evaporation method. During the VLD process, close-packed PS NP structures form at the air-water-solid interface. The polyacrylic acid(PAA)-rich amphiphilic oligomers constantly supplied from the liquid phase to the forming structure and accumulated between PS NPs. After drying, the existence of PAA-rich oligomers between the PS NPs disturbs

the observation of the acoustic vibration modes of PS NPs by BLS. On the other hand, for the drop evaporation method, a PS NPs dispersion droplet forms on a glass substrate. The remained PAA-rich polymer fraction in the dispersion accumulates at the ring edge of the droplet during the dry process because of the coffee strain effect. Therefore, f(s,1,2) mode can be observed inside of the dried droplet. To reduce remained oligomer effects, all PS NPs were purified after the surfactant-free polymerization process and prepared as colloidal assemblies for the BLS characterization.

8.3. Surface roughness effect on BLS

The PS NPs and atomic force microscopy (AFM) images with different surfaces (rough and smooth) were provided by Prof. Duits group (University of Twente).[255] All samples were fabricated on glass substrates by the drop evaporation method. The samples were characterized by BLS to investigate the surface roughness effect on particle interactions. From the AFM images on the right panel in **Figure 8.3b**, NPs have different roughness on the surfaces for each size. Anti-stokes sides
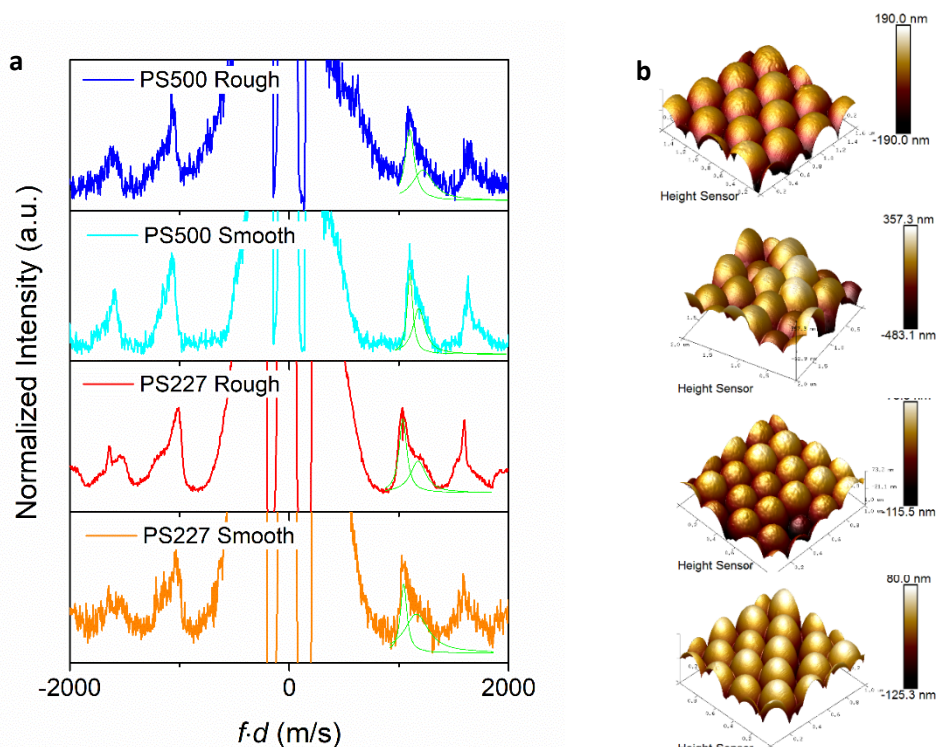
Figure 8.3. **(a)** Anti-stokes side of Brillouin light scattering (BLS) spectra (I vs. $f \cdot d$) for four different PS NPs with diameter, d = 227 nm, 500 nm with rough and smooth surfaces. The green solid lines represent the (1,2) mode by a double Lorentzian with frequencies f_1 and f_2. **(b)** AFM images of each NP surface. PS500 rough and smooth surface, PS227 rough and smooth surface (from top to bottom)

of BLS spectra (I vs $f \cdot d$) of two different groups in size and composition, PS227 and PS500 are shown in **Figure 8.3a**. The reduced frequency ($f \cdot d$) was used for the x-axis to remove diameter factors for the result. They showed no difference in particle interactions depending on the surface roughness. PS500 and PS227 have only different distributions of f_1 and f_2 in $f(1,2)$ because of their different chemical compositions.

Reference

(1)   Allen, T. M.; Cullis, P. R. Drug Delivery Systems: Entering the Mainstream. *Science* **2004**, *303* (5665), 1818–1822. https://doi.org/10.1126/science.1095833.

(2)   Prevo, B. G.; Kuncicky, D. M.; Velev, O. D. Engineered Deposition of Coatings from Nano- and Micro-Particles: A Brief Review of Convective Assembly at High Volume Fraction. *Colloids and Surfaces A: Physicochemical and Engineering Aspects* **2007**, *311*, 2–10. https://doi.org/10.1016/j.colsurfa.2007.08.030.

(3)   Panigrahi, S.; Kundu, S.; Ghosh, S.; Nath, S.; Pal, T. General Method of Synthesis for Metal Nanoparticles. *Journal of Nanoparticle Research* **2004**, *6* (4), 411–414. https://doi.org/10.1007/s11051-004-6575-2.

(4)   Zhang, C.; Guo, Y.; Priestley, R. D. Glass Transition Temperature of Polymer Nanoparticles under Soft and Hard Confinement. *Macromolecules* **2011**, *44* (10), 4001–4006. https://doi.org/10.1021/ma1026862.

(5)   Keddie, J. L.; Jones, R. A. L.; Cory, R. A. Size-Dependent Depression of the Glass Transition Temperature in Polymer Films. *EPL* **1994**, *27* (1), 59. https://doi.org/10.1209/0295-5075/27/1/011.

(6)   Ediger, M. D.; Forrest, J. A. Dynamics near Free Surfaces and the Glass Transition in Thin Polymer Films: A View to the Future. *Macromolecules* **2014**, *47*, 471–478. https://doi.org/10.1021/ma4017696.

(7)   Feng, S.; Li, Z.; Liu, R.; Mai, B.; Wu, Q.; Liang, G.; Gao, H.; Zhu, F. Glass Transition of Polystyrene Nanospheres under Different Confined Environments in Aqueous Dispersions. *Soft Matter* **2013**, *9* (18), 4614–4620.

(8)   Christie, D.; Zhang, C.; Fu, J.; Koel, B.; Priestley, R. D. Glass Transition Temperature of Colloidal Polystyrene Dispersed in Various Liquids. *Journal of Polymer Science, Part B: Polymer Physics* **2016**, *54* (17), 1776–1783. https://doi.org/10.1002/polb.24082.

(9)   Del Fatti, N.; Voisin, C.; Chevy, F.; Vallée, F.; Flytzanis, C. Coherent Acoustic Mode Oscillation and Damping in Silver Nanoparticles. *J. Chem. Phys.* **1999**, *110* (23), 11484–11487. https://doi.org/10.1063/1.479089.

(10)   Ivanda, M.; Furić, K.; Musić, S.; Ristić, M.; Gotić, M.; Ristić, D.; Tonejc, A. M.; Djerdj, I.; Mattarelli, M.; Montagna, M.; et al. Low Wavenumber Raman Scattering of Nanoparticles and Nanocomposite Materials. *Journal of Raman Spectroscopy* **2007**, *38* (6), 647–659. https://doi.org/10.1002/jrs.1723.

(11)   Lamb, H. On the Vibrations of an Elastic Sphere. *Proceedings of the London Mathematical Society* **1881**, *s1-13* (1), 189–212. https://doi.org/10.1112/plms/s1-13.1.189.

(12)   Kim, H.; Cang, Y.; Kang, E.; Graczykowski, B.; Secchi, M.; Montagna, M.; Priestley, R. D.; Furst, E. M.; Fytas, G. Direct Observation of Polymer Surface Mobility via Nanoparticle Vibrations. *Nature Communications* **2018**, *9* (1), 2918. https://doi.org/10.1038/s41467-018-04854-w.

(13)   Myers, D. *Surfaces, Interfaces, and Colloids*; John Wiley & Sons, Inc.: New York, USA, 1999. https://doi.org/10.1002/0471234990.

(14)   Sugimoto, T. *Fine Particles: Synthesis, Characterization, and Mechanisms of Growth*; CRC Press, 2000.

(15)   Matijevic, E. Preparation and Properties of Uniform Size Colloids. *Chem. Mater.* **1993**, *5* (4), 412–426. https://doi.org/10.1021/cm00028a004.

(16)   Arshady, R. Suspension, Emulsion, and Dispersion Polymerization: A Methodological Survey. *Colloid Polym Sci* **1992**, *270* (8), 717–732. https://doi.org/10.1007/BF00776142.

(17)   Caruso, F. *Colloids and Colloid Assemblies: Synthesis, Modification, Organization and Utilization of Colloid Particles*; John Wiley & Sons, 2006.

(18)   Matsumoto, T.; Ochi, A. Polymerization of Styrene in Aqueous Solution. *Kobunshi Kagaku* **1965**, *22* (244), 481–487. https://doi.org/10.1295/koron1944.22.481.

(19)   Goodall, A. R.; Wilkinson, M. C.; Hearn, J. Mechanism of Emulsion Polymerization of Styrene in Soap-Free Systems. *J. Polym. Sci. Polym. Chem. Ed.* **1977**, *15* (9), 2193–2218. https://doi.org/10.1002/pol.1977.170150912.

(20)   Tauer, K. Block Copolymers Prepared by Emulsion Polymerization with Poly(Ethylene Oxide)–Azo-Initiators. *Polymers for Advanced Technologies* **1995**, *6* (7), 435–440. https://doi.org/10.1002/pat.1995.220060703.

(21)   Fang, S.-J.; Fujimoto, K.; Kondo, S.; Shiraki, K.; Kawaguchi, H. Emulsifier-Free Emulsion Copolymerization of Styrene and Acrylamide Using an Amphoteric Initiator. *Colloid Polym Sci* **2000**, *278* (9), 864–871. https://doi.org/10.1007/s003960000337.

(22)   Williams, D. J. Morphology Considerations in Heterogeneous Latexes for Impact Polymers. *Journal of Elastoplastics* **1973**, *5* (1), 6–19. https://doi.org/10.1177/009524437300500102.

(23)   Napper, D. H. Particle Morphology in Emulsion Polymerization. *Journal of Polymer Science Part A-1: Polymer Chemistry* **1971**, *9* (7), 2089–2091. https://doi.org/10.1002/pol.1971.150090726.

(24)   Chung-li, Y.; goodwin, J. W.; Ottewill, R. H. Studies on the Preparation and Characterisation of Monodisperse Polystyrene Latices. In *Kolloidchemie heute II*; Kohlschütter, H. W., Müller, F. H., Weiss, A., Eds.; Progress in Colloid & Polymer Science; Steinkopff: Darmstadt, 1976; pp 163–175. https://doi.org/10.1007/BFb0117065.

(25)   Song, Z.; Poehlein, G. W. Particle Nucleation in Emulsifier-Free Aqueous-Phase Polymerization: Stage 1. *Journal of Colloid and Interface Science* **1989**, *128* (2), 486–500. https://doi.org/10.1016/0021-9797(89)90364-0.

(26)   Fitch, R. M.; Tsai, C. H. Particle Formation in Polymer Colloids, III: Prediction of the Number of Particles by a Homogeneous Nucleation Theory. In *Polymer Colloids*; Fitch, R. M., Ed.; Springer US: Boston, MA, 1971; pp 73–102. https://doi.org/10.1007/978-1-4684-1920-7_5.

(27)   Tanrisever, T.; Okay, O.; Sönmezoğlu, I. Ç. Kinetics of Emulsifier–Free Emulsion Polymerization of Methyl Methacrylate. *Journal of Applied Polymer Science* **1996**, *61* (3), 485–493. https://doi.org/10.1002/(SICI)1097-4628(19960718)61:3<485::AID-APP11>3.0.CO;2-0.

(28)   Hearn, J.; Wilkinson, M. C.; Goodall, A. R.; Chainey, M. Kinetics of the Surfactant-Free Emulsion Polymerization of Styrene:-The Post Nucleation Stage. *Journal of Polymer Science: Polymer Chemistry Edition* **1985**, *23* (7), 1869–1883. https://doi.org/10.1002/pol.1985.170230703.

(29)   Rao, K. S.; El-Hami, K.; Kodaki, T.; Matsushige, K.; Makino, K. A Novel Method for Synthesis of Silica Nanoparticles. *Journal of Colloid and Interface Science* **2005**, *289* (1), 125–131. https://doi.org/10.1016/j.jcis.2005.02.019.

(30)   Stöber, W.; Fink, A.; Bohn, E. Controlled Growth of Monodisperse Silica Spheres in the Micron Size Range. *Journal of Colloid and Interface Science* **1968**, *26* (1), 62–69. https://doi.org/10.1016/0021-9797(68)90272-5.

(31)   Lindberg, R.; Sjöblom, J.; Sundholm, G. Preparation of Silica Particles Utilizing the Sol-Gel and the Emulsion-Gel Processes. *Colloids and Surfaces A: Physicochemical and Engineering Aspects* **1995**, *99* (1), 79–88. https://doi.org/10.1016/0927-7757(95)03117-V.

(32)   Tan, C. G.; Bowen, B. D.; Epstein, N. Production of Monodisperse Colloidal Silica Spheres: Effect of Temperature. *Journal of Colloid and Interface Science* **1987**, *118* (1), 290–293. https://doi.org/10.1016/0021-9797(87)90458-9.

(33)   Bogush, G. H.; Zukoski, C. F. Studies of the Kinetics of the Precipitation of Uniform Silica Particles through the Hydrolysis and Condensation of Silicon Alkoxides. *Journal of Colloid and Interface Science* **1991**, *142* (1), 1–18. https://doi.org/10.1016/0021-9797(91)90029-8.

(34)   Bogush, G. H.; Tracy, M. A.; Zukoski, C. F. Preparation of Monodisperse Silica Particles: Control of Size and Mass Fraction. *Journal of Non-Crystalline Solids* **1988**, *104* (1), 95–106. https://doi.org/10.1016/0022-3093(88)90187-1.

(35)   Wei, L.; Lu, J.; Xu, H.; Patel, A.; Chen, Z.-S.; Chen, G. Silver Nanoparticles: Synthesis, Properties, and Therapeutic Applications. *Drug Discovery Today* **2015**, *20* (5), 595–601. https://doi.org/10.1016/j.drudis.2014.11.014.

(36)   Lee, P. C.; Meisel, D. Adsorption and Surface-Enhanced Raman of Dyes on Silver and Gold Sols. *J. Phys. Chem.* **1982**, *86* (17), 3391–3395. https://doi.org/10.1021/j100214a025.

(37)   Navaladian, S.; Viswanathan, B.; Viswanath, R. P.; Varadarajan, T. K. Thermal Decomposition as Route for Silver Nanoparticles. *Nanoscale Res Lett* **2007**, *2* (1), 44–48. https://doi.org/10.1007/s11671-006-9028-2.

(38)   Jin, R.; Cao, Y.; Mirkin, C. A.; Kelly, K. L.; Schatz, G. C.; Zheng, J. G. Photoinduced Conversion of Silver Nanospheres to Nanoprisms. *Science* **2001**, *294* (5548), 1901–1903. https://doi.org/10.1126/science.1066541.

(39)   Shin, H. S.; Yang, H. J.; Kim, S. B.; Lee, M. S. Mechanism of Growth of Colloidal Silver Nanoparticles Stabilized by Polyvinyl Pyrrolidone in γ-Irradiated Silver Nitrate Solution. *Journal of Colloid and Interface Science* **2004**, *274* (1), 89–94. https://doi.org/10.1016/j.jcis.2004.02.084.

(40)   Polte, J.; Tuaev, X.; Wuithschick, M.; Fischer, A.; Thuenemann, A. F.; Rademann, K.; Kraehnert, R.; Emmerling, F. Formation Mechanism of Colloidal Silver Nanoparticles: Analogies and Differences to the Growth of Gold Nanoparticles. *ACS Nano* **2012**, *6* (7), 5791–5802. https://doi.org/10.1021/nn301724z.

(41)   Evanoff, D. D.; Chumanov, G. Size-Controlled Synthesis of Nanoparticles. 1. "Silver-Only" Aqueous Suspensions via Hydrogen Reduction. *J. Phys. Chem. B* **2004**, *108* (37), 13948–13956. https://doi.org/10.1021/jp047565s.

(42)   Panáček, A.; Kvítek, L.; Prucek, R.; Kolář, M.; Večeřová, R.; Pizúrová, N.; Sharma, V. K.; Nevěčná, T.; Zbořil, R. Silver Colloid Nanoparticles: Synthesis, Characterization, and Their Antibacterial Activity. *J. Phys. Chem. B* **2006**, *110* (33), 16248–16253. https://doi.org/10.1021/jp063826h.

(43)   Alan Creighton, J.; G. Blatchford, C.; Grant Albrecht, M. Plasma Resonance Enhancement of Raman Scattering by Pyridine Adsorbed on Silver or Gold Sol Particles of Size Comparable to the Excitation Wavelength. *Journal of the Chemical Society, Faraday Transactions 2: Molecular and Chemical Physics* **1979**, *75* (0), 790–798. https://doi.org/10.1039/F29797500790.

(44)   Zielińska, A.; Skwarek, E.; Zaleska, A.; Gazda, M.; Hupka, J. Preparation of Silver Nanoparticles with Controlled Particle Size. *Procedia Chemistry* **2009**, *1* (2), 1560–1566. https://doi.org/10.1016/j.proche.2009.11.004.

(45)   Patakfalvi, R.; Virányi, Z.; Dékány, I. Kinetics of Silver Nanoparticle Growth in Aqueous Polymer Solutions. *Colloid Polym Sci* **2004**, *283* (3), 299–305. https://doi.org/10.1007/s00396-004-1138-8.

(46)   Pillai, Z. S.; Kamat, P. V. What Factors Control the Size and Shape of Silver Nanoparticles in the Citrate Ion Reduction Method? *J. Phys. Chem. B* **2004**, *108* (3), 945–951. https://doi.org/10.1021/jp037018r.

(47)   Shirtcliffe, N.; Nickel, U.; Schneider, S. Reproducible Preparation of Silver Sols with Small Particle Size Using Borohydride Reduction: For Use as Nuclei for Preparation of Larger Particles. *Journal of Colloid and Interface Science* **1999**, *211* (1), 122–129. https://doi.org/10.1006/jcis.1998.5980.

(48)   Rainville, L.; Dorais, M.-C.; Boudreau, D. Controlled Synthesis of Low Polydispersity Ag@SiO 2 Core–Shell Nanoparticles for Use in Plasmonic Applications. *RSC Advances* **2013**, *3* (33), 13953–13960. https://doi.org/10.1039/C3RA41677A.

(49)   Bastús, N. G.; Merkoçi, F.; Piella, J.; Puntes, V. Synthesis of Highly Monodisperse Citrate-Stabilized Silver Nanoparticles of up to 200 Nm: Kinetic Control and Catalytic Properties. *Chem. Mater.* **2014**, *26* (9), 2836–2846. https://doi.org/10.1021/cm500316k.

(50)   Oldenburg, S. J.; Averitt, R. D.; Westcott, S. L.; Halas, N. J. Nanoengineering of Optical Resonances. *Chemical Physics Letters* **1998**, *288* (2), 243–247. https://doi.org/10.1016/S0009-2614(98)00277-2.

(51)   Sajjadi, S. Particle Formation under Monomer-Starved Conditions in the Semibatch Emulsion Polymerization of Styrene. I. Experimental. *Journal of Polymer Science Part A: Polymer Chemistry* **2001**, *39* (22), 3940–3952. https://doi.org/10.1002/pola.10031.

(52)   Kim, J.-W.; Suh, K.-D. Monodisperse Polymer Particles Synthesized by Seeded Polymerization Techniques. *Journal of Industrial and Engineering Chemistry* **2008**, *14* (1), 1–9. https://doi.org/10.1016/j.jiec.2007.06.001.

(53)   Decher, G.; Hong, J. D.; Schmitt, J. Buildup of Ultrathin Multilayer Films by a Self-Assembly Process: III. Consecutively Alternating Adsorption of Anionic and Cationic Polyelectrolytes on Charged Surfaces. *Thin Solid Films* **1992**, *210–211*, 831–835. https://doi.org/10.1016/0040-6090(92)90417-A.

(54)   Decher, G. Fuzzy Nanoassemblies: Toward Layered Polymeric Multicomposites. *Science* **1997**, *277* (5330), 1232–1237. https://doi.org/10.1126/science.277.5330.1232.

(55)   Hoogeveen, N. G.; Cohen Stuart, M. A.; Fleer, G. J.; Böhmer, M. R. Formation and Stability of Multilayers of Polyelectrolytes. *Langmuir* **1996**, *12* (15), 3675–3681. https://doi.org/10.1021/la951574y.

(56)   Caruso, F.; Spasova, M.; Salgueiriño-Maceira, V.; Liz-Marzán, L. M. Multilayer Assemblies of Silica-Encapsulated Gold Nanoparticles on Decomposable Colloid Templates. *Advanced Materials* **2001**, *13* (14), 1090–1094. https://doi.org/10.1002/1521-4095(200107)13:14<1090::AID-ADMA1090>3.0.CO;2-H.

(57)   Lvov, Y.; Ariga, K.; Onda, M.; Ichinose, I.; Kunitake, T. Alternate Assembly of Ordered Multilayers of SiO2 and Other Nanoparticles and Polyions. *Langmuir* **1997**, *13* (23), 6195–6203. https://doi.org/10.1021/la970517x.

(58)   Guzmán, E.; Ritacco, H.; F. Rubio, J. E.; G. Rubio, R.; Ortega, F. Salt-Induced Changes in the Growth of Polyelectrolyte Layers of Poly(Diallyl-Dimethylammonium Chloride) and Poly(4-Styrene Sulfonate of Sodium). *Soft Matter* **2009**, *5* (10), 2130–2142. https://doi.org/10.1039/B901193E.

(59)   Sukhorukov, G. B.; Donath, E.; Lichtenfeld, H.; Knippel, E.; Knippel, M.; Budde, A.; Möhwald, H. Layer-by-Layer Self Assembly of Polyelectrolytes on Colloidal Particles. *Colloids and Surfaces A: Physicochemical and Engineering Aspects* **1998**, *137* (1), 253–266. https://doi.org/10.1016/S0927-7757(98)00213-1.

(60)   Sukhorukov, G. B.; Donath, E.; Davis, S.; Lichtenfeld, H.; Caruso, F.; Popov, V. I.; Möhwald, H. Stepwise Polyelectrolyte Assembly on Particle Surfaces: A Novel Approach to Colloid Design. *Polymers for Advanced Technologies* **1998**, *9* (10–11), 759–767. https://doi.org/10.1002/(SICI)1099-1581(1998100)9:10/11<759::AID-PAT846>3.0.CO;2-Q.

(61)   Tessier, M. D.; Biadala, L.; Bouet, C.; Ithurria, S.; Abecassis, B.; Dubertret, B. Phonon Line Emission Revealed by Self-Assembly of Colloidal Nanoplatelets. *ACS Nano* **2013**, *7* (4), 3332–3340. https://doi.org/10.1021/nn400833d.

(62)   Norris, D. J.; Arlinghaus, E. G.; Meng, L.; Heiny, R.; Scriven, L. E. Opaline Photonic Crystals: How Does Self-Assembly Work? *Advanced Materials* **2004**, *16* (16), 1393–1399. https://doi.org/10.1002/adma.200400455.

(63)   Baumgartl, J.; Zvyagolskaya, M.; Bechinger, C. Tailoring of Phononic Band Structures in Colloidal Crystals. *Phys. Rev. Lett.* **2007**, *99* (20), 205503. https://doi.org/10.1103/PhysRevLett.99.205503.

(64)   Wong, S.; Kitaev, V.; Ozin, G. A. Colloidal Crystal Films: Advances in Universality and Perfection. *J. Am. Chem. Soc.* **2003**, *125* (50), 15589–15598. https://doi.org/10.1021/ja0379969.

(65)   Chung, Y.-W.; Leu, I.-C.; Lee, J.-H.; Hon, M.-H. Influence of Humidity on the Fabrication of High-Quality Colloidal Crystals via a Capillary-Enhanced Process. *Langmuir* **2006**, *22* (14), 6454–6460. https://doi.org/10.1021/la060248n.

(66)   Dimitrov, A. S.; Dushkin, C. D.; Yoshimura, H.; Nagayama, K. Observations of Latex Particle Two-Dimensional-Crystal Nucleation in Wetting Films on Mercury, Glass, and Mica. *Langmuir* **1994**, *10* (2), 432–440. https://doi.org/10.1021/la00014a017.

(67)   Nagayama, K. Fabrication of Two-Dimensional Colloidal Arrays. *Phase Transitions* **1993**, *45* (2–3), 185–203. https://doi.org/10.1080/01411599308223723.

(68)   S. Lazarov, G.; D. Denkov, N.; D. Velev, O.; A. Kralchevsky, P.; Nagayama, K. Formation of Two-Dimensional Structures from Colloidal Particles on Fluorinated Oil Substrate. *Journal of the Chemical Society, Faraday Transactions* **1994**, *90* (14), 2077–2083. https://doi.org/10.1039/FT9949002077.

(69)   Kralchevsky, P. A.; Denkov, N. D. Capillary Forces and Structuring in Layers of Colloid Particles. *Current Opinion in Colloid & Interface Science* **2001**, *6* (4), 383–401. https://doi.org/10.1016/S1359-0294(01)00105-4.

(70)   Chan, D. Y. C.; Henry, J. D.; White, L. R. The Interaction of Colloidal Particles Collected at Fluid Interfaces. *Journal of Colloid and Interface Science* **1981**, *79* (2), 410–418. https://doi.org/10.1016/0021-9797(81)90092-8.

(71)   Tabor, D. Babylonian Lecanomancy: An Ancient Text on the Spreading of Oil on Water. *Journal of Colloid and Interface Science* **1980**, *75* (1), 240–245. https://doi.org/10.1016/0021-9797(80)90366-5.

(72)   Pockels, A. On the Spreading of Oil upon Water. *Nature* **1894**, *50* (1288), 223–224. https://doi.org/10.1038/050223a0.

(73)   Langmuir, I. THE CONSTITUTION AND FUNDAMENTAL PROPERTIES OF SOLIDS AND LIQUIDS. PART I. SOLIDS. *J. Am. Chem. Soc.* **1916**, *38* (11), 2221–2295. https://doi.org/10.1021/ja02268a002.

(74)   Blodgett, K. B. Films Built by Depositing Successive Monomolecular Layers on a Solid Surface. *J. Am. Chem. Soc.* **1935**, *57* (6), 1007–1022. https://doi.org/10.1021/ja01309a011.

(75)   Clint, J. H.; Taylor, S. E. Particle Size and Interparticle Forces of Overbased Detergents: A Langmuir Trough Study. *Colloids and Surfaces* **1992**, *65* (1), 61–67. https://doi.org/10.1016/0166-6622(92)80175-2.

(76)   Bardosova, M.; Pemble, M. E.; Povey, I. M.; Tredgold, R. H. The Langmuir-Blodgett Approach to Making Colloidal Photonic Crystals from Silica Spheres. *Advanced Materials* **2010**, *22* (29), 3104–3124. https://doi.org/10.1002/adma.200903708.

(77)   Huie, J. C. Guided Molecular Self-Assembly: A Review of Recent Efforts. *Smart Mater. Struct.* **2003**, *12* (2), 264–271. https://doi.org/10.1088/0964-1726/12/2/315.

(78)   Reculusa, S.; Ravaine, S. Synthesis of Colloidal Crystals of Controllable Thickness through the Langmuir−Blodgett Technique. *Chem. Mater.* **2003**, *15* (2), 598–605. https://doi.org/10.1021/cm021242w.

(79)   Szekeres, M.; Kamalin, O.; A. Schoonheydt, R.; Wostyn, K.; Clays, K.; Persoons, A.; Dékány, I. Ordering and Optical Properties of Monolayers and Multilayers of Silica Spheres Deposited by the Langmuir–Blodgett Method. *Journal of Materials Chemistry* **2002**, *12* (11), 3268–3274. https://doi.org/10.1039/B204687C.

(80)   Aveyard, R.; Clint, J. H.; Nees, D.; Paunov, V. N. Compression and Structure of Monolayers of Charged Latex Particles at Air/Water and Octane/Water Interfaces. *Langmuir* **2000**, *16* (4), 1969–1979. https://doi.org/10.1021/la990887g.

(81)   Wang, J.; Ahl, S.; Li, Q.; Kreiter, M.; Neumann, T.; Burkert, K.; Knoll, W.; Jonas, U. Structural and Optical Characterization of 3D Binary Colloidal Crystal and Inverse Opal Films Prepared by Direct Co-Deposition. *Journal of Materials Chemistry* **2008**, *18* (9), 981–988. https://doi.org/10.1039/B715329E.

(82)   Vogel, N.; Retsch, M.; Fustin, C.-A.; del Campo, A.; Jonas, U. Advances in Colloidal Assembly: The Design of Structure and Hierarchy in Two and Three Dimensions. *Chem. Rev.* **2015**, *115* (13), 6265–6311. https://doi.org/10.1021/cr400081d.

(83)   Landau, L.; Levich, B. Dragging of a Liquid by a Moving Plate. In *Dynamics of Curved Fronts*; Pelcé, P., Ed.; Academic Press: San Diego, 1988; pp 141–153. https://doi.org/10.1016/B978-0-08-092523-3.50016-2.

(84)   Ghosh, M.; Fan, F.; Stebe, K. J. Spontaneous Pattern Formation by Dip Coating of Colloidal Suspensions on Homogeneous Surfaces. *Langmuir* **2007**, *23* (4), 2180–2183. https://doi.org/10.1021/la062150e.

(85)   Berteloot, G.; Daerr, A.; Lequeux, F.; Limat, L. Dip Coating with Colloids and Evaporation. *Chemical Engineering and Processing: Process Intensification* **2013**, *68*, 69–73. https://doi.org/10.1016/j.cep.2012.09.001.

(86)   Grosso, D. How to Exploit the Full Potential of the Dip-Coating Process to Better Control Film Formation. *Journal of Materials Chemistry* **2011**, *21* (43), 17033–17038. https://doi.org/10.1039/C1JM12837J.

112

(87)   Giuliani, M.; González-Viñas, W.; Poduska, K. M.; Yethiraj, A. Dynamics of Crystal Structure Formation in Spin-Coated Colloidal Films. *J. Phys. Chem. Lett.* **2010**, *1* (9), 1481–1486. https://doi.org/10.1021/jz1002605.

(88)   Chen, J.; Dong, P.; Di, D.; Wang, C.; Wang, H.; Wang, J.; Wu, X. Controllable Fabrication of 2D Colloidal-Crystal Films with Polystyrene Nanospheres of Various Diameters by Spin-Coating. *Applied Surface Science* **2013**, *270*, 6–15. https://doi.org/10.1016/j.apsusc.2012.11.165.

(89)   Colson, P.; Cloots, R.; Henrist, C. Experimental Design Applied to Spin Coating of 2D Colloidal Crystal Masks: A Relevant Method? *Langmuir* **2011**, *27* (21), 12800–12806. https://doi.org/10.1021/la202284a.

(90)   Meyerhofer, D. Characteristics of Resist Films Produced by Spinning. *Journal of Applied Physics* **1978**, *49* (7), 3993–3997. https://doi.org/10.1063/1.325357.

(91)   Cregan, V.; O'Brien, S. B. G. A Note on Spin-Coating with Small Evaporation. *Journal of Colloid and Interface Science* **2007**, *314* (1), 324–328. https://doi.org/10.1016/j.jcis.2007.05.019.

(92)   Butler, J. H.; Joy, D. C.; Bradley, G. F.; Krause, S. J. Low-Voltage Scanning Electron Microscopy of Polymers. *Polymer* **1995**, *36* (9), 1781–1790. https://doi.org/10.1016/0032-3861(95)90924-Q.

(93)   Joy, D. C. Resolution in Low Voltage Scanning Electron Microscopy. *Journal of Microscopy* **1985**, *140* (3), 283–292. https://doi.org/10.1111/j.1365-2818.1985.tb02682.x.

(94)   Joy, D. C.; Joy, C. S. Low Voltage Scanning Electron Microscopy. *Micron* **1996**, *27* (3), 247–263. https://doi.org/10.1016/0968-4328(96)00023-6.

(95)   Hassan, P. A.; Rana, S.; Verma, G. Making Sense of Brownian Motion: Colloid Characterization by Dynamic Light Scattering. *Langmuir* **2015**, *31* (1), 3–12. https://doi.org/10.1021/la501789z.

(96)   Pecora, R. Dynamic Light Scattering Measurement of Nanometer Particles in Liquids. *Journal of Nanoparticle Research* **2000**, *2* (2), 123–131. https://doi.org/10.1023/A:1010067107182.

(97)   Kaszuba, M.; McKnight, D.; Connah, M. T.; McNeil-Watson, F. K.; Nobbmann, U. Measuring Sub Nanometre Sizes Using Dynamic Light Scattering. *J Nanopart Res* **2008**, *10* (5), 823–829. https://doi.org/10.1007/s11051-007-9317-4.

(98)   Ross Hallett, F. Particle Size Analysis by Dynamic Light Scattering. *Food Research International* **1994**, *27* (2), 195–198. https://doi.org/10.1016/0963-9969(94)90162-7.

(99)   Jasse, B. Fourier Transform Infrared Spectroscopy of Synthetic Polymers. In *Developments in Polymer Characterisation—4*; Dawkins, J. V., Ed.; Springer Netherlands: Dordrecht, 1983; pp 91–129. https://doi.org/10.1007/978-94-009-6628-4_3.

(100)   Koenig, J. L. Fourier Transform Infrared Spectroscopy of Polymers. In *Spectroscopy: NMR, Fluorescence, FT-IR*; Advances in Polymer Science; Springer: Berlin, Heidelberg, 1984; pp 87–154. https://doi.org/10.1007/3-540-12591-4_6.

(101)   Smith, B. C. *Fundamentals of Fourier Transform Infrared Spectroscopy*; CRC Press, 1995.

(102)   Schick, C. Differential Scanning Calorimetry (DSC) of Semicrystalline Polymers. *Anal Bioanal Chem* **2009**, *395* (6), 1589–1611. https://doi.org/10.1007/s00216-009-3169-y.

(103)   Höhne, G.; Hemminger, W. F.; Flammersheim, H.-J. *Differential Scanning Calorimetry*; Springer Science & Business Media, 2013.

(104)   Bershteĭn, V. A.; Egorov, V. M. *Differential Scanning Calorimetry of Polymers: Physics, Chemistry, Analysis, Technology*; Ellis Horwood, 1994.

(105)   Reading, M.; Luget, A.; Wilson, R. Modulated Differential Scanning Calorimetry. *Thermochimica Acta* **1994**, *238*, 295–307. https://doi.org/10.1016/S0040-6031(94)85215-4.

(106)   Schneider, D. Hypersonic Phonon Propagation in Mesoscopic Systems by Brillouin Spectroscopy. PhD Thesis, Johannes Gutenberg–Universiẗat Mainz, 2013.

(107)   Cheng, W. Hypersonic Elastic Excitations in Soft Mesoscopic Structures. PhD Thesis, Johannes Gutenberg-Universität Mainz, 2007.

(108)   Sui, L.; Huang, L.; Podsiadlo, P.; Kotov, N. A.; Kieffer, J. Brillouin Light Scattering Investigation of the Mechanical Properties of Layer-by-Layer Assembled Cellulose

Nanocrystal Films. *Macromolecules* **2010**, *43* (22), 9541–9548. https://doi.org/10.1021/ma1016488.

(109) Soppimath, K. S.; Aminabhavi, T. M.; Kulkarni, A. R.; Rudzinski, W. E. Biodegradable Polymeric Nanoparticles as Drug Delivery Devices. *Journal of Controlled Release* **2001**, *70*, 1–20. https://doi.org/10.1016/S0168-3659(00)00339-4.

(110) Kumari, A.; Yadav, S. K.; Yadav, S. C. Biodegradable Polymeric Nanoparticles Based Drug Delivery Systems. *Colloids and Surfaces B: Biointerfaces* **2010**, *75* (1), 1–18. https://doi.org/10.1016/j.colsurfb.2009.09.001.

(111) Shipway, A. N.; Katz, E.; Willner, I. Nanoparticle Arrays on Surfaces for Electronic, Optical, and Sensor Applications. *ChemPhysChem* **2000**, *1*, 18–52. https://doi.org/10.1002/1439-7641.

(112) Hosein, I. D.; Lee, S. H.; Liddell, C. M. Dimer-Based Three-Dimensional Photonic Crystals. *Advanced Functional Materials* **2010**, *20* (18), 3085–3091. https://doi.org/10.1002/adfm.201000134.

(113) Ding, T.; Song, K.; Clays, K.; Tung, C. H. Fabrication of 3D Photonic Crystals of Ellipsoids: Convective Self-Assembly in Magnetic Field. *Advanced Materials* **2009**, *21* (19), 1936–1940. https://doi.org/10.1002/adma.200803564.

(114) Forster, J. D.; Park, J.-G.; Mittal, M.; Noh, H.; Schreck, C. F.; O'Hern, C. S.; Cao, H.; Furst, E. M.; Dufresne, E. R. Assembly of Optical Scale Dumbbells Into Dense Photonic Crystals. *ACS nano* **2011**, No. 8, 6695–6700. https://doi.org/10.1021/nn202227f.

(115) Beltramo, P. J.; Schneider, D.; Fytas, G.; Furst, E. M. Anisotropic Hypersonic Phonon Propagation in Films of Aligned Ellipsoids. *Physical Review Letters* **2014**, *113* (20), 1–5. https://doi.org/10.1103/PhysRevLett.113.205503.

(116) Cheng, W.; Wang, J.; Jonas, U.; Fytas, G.; Stefanou, N. Observation and Tuning of Hypersonic Bandgaps in Colloidal Crystals. *Nature materials* **2006**, *5* (10), 830–836. https://doi.org/10.1038/nmat1727.

(117) Kawana, S.; Jones, R. A. L. Character of the Glass Transition in Thin Supported Polymer Films. *Phys. Rev. E* **2001**, *63* (2), 021501. https://doi.org/10.1103/PhysRevE.63.021501.

(118) Keddie, J. L.; Jones, R. A. L.; Cory, R. A. Temperature in Thin Polymer Films. *Faraday Discussions* **1994**, *98*, 219–230.

(119) Ellison, C. J.; Torkelson, J. M. The Distribution of Glass-Transition Temperatures in Nanoscopically Confined Glass Formers. *Nature materials* **2003**, *2* (10), 695–700. https://doi.org/10.1038/nmat980.

(120) Priestley, R. D.; Broadbelt, L. J.; Torkelson, J. M.; Fukao, K. Glass Transition and ?-Relaxation Dynamics of Thin Films of Labeled Polystyrene. *Physical Review E* **2007**, *75* (6). https://doi.org/10.1103/PhysRevE.75.061806.

(121) Akabori, K.; Tanaka, K.; Nagamura, T.; Takahara, A.; Kajiyama, T. Molecular Motion in Ultrathin Polystyrene Films : Dynamic Mechanical Analysis of Surface and Interfacial Effects. *Macromolecules* **2005**, *38*, 9735–9741. https://doi.org/10.1021/ma051143e.

(122) Forrest, J. A.; DalnokiVeress, K.; Stevens, J. R.; Dutcher, J. R. Effect of Free Surfaces on the Glass Transition Temperature of Thin Polymer Films. *Physical Review Letters* **1996**, *77* (111), 2002–2005. https://doi.org/10.1103/PhysRevLett.77.2002.

(123) Forrest, J. A.; DalnokiVeress, K.; Dutcher, J. R. Interface and Chain Confinement Effects on the Glass Transition Temperature of Thin Polymer Films. *Physical Review E* **1997**, *56* (5), 5705–5716. https://doi.org/DOI 10.1103/PhysRevE.56.5705.

(124) Chai, Y.; Salez, T.; McGraw, J. D.; Benzaquen, M.; Dalnoki-Veress, K.; Raphaël, E.; Forrest, J. A. A Direct Quantitative Measure of Surface Mobility in a Glassy Polymer. *Science* **2014**, *343*, 994–999.

(125) Zhang, W.; Yu, L. Surface Diffusion of Polymer Glasses. *Macromolecules* **2016**, *49* (2), 731–735. https://doi.org/10.1021/acs.macromol.5b02294.

(126) Yang, Z.; Fujii, Y.; Lee, F. K.; Lam, C.; Tsui, O. K. C. Glass Transition Dynamics and Surface Layer Mobility in Unentangled Polystyrene Films. *Science* **2010**, *328*, 1676–1679. https://doi.org/10.1126/science.1184394.

(127) Fakhraai, Z.; Forrest, J. A. Measuring the Surface Dynamics of Glassy Polymers. *Science* **2008**, *319*, 600–604.

114

(128) Martínez-Tong, D. E.; Soccio, M.; Sanz, A.; García, C.; Ezquerra, T. A.; Nogales, A. Chain Arrangement and Glass Transition Temperature Variations in Polymer Nanoparticles under 3D-Confinement. *Macromolecules* **2013**, *46* (11), 4698–4705. https://doi.org/10.1021/ma400379a.

(129) Perez-de-Eulate, N. G.; Di Lisio, V.; Cangialosi, D. Glass Transition and Molecular Dynamics in Polystyrene Nanospheres by Fast Scanning Calorimetry. *ACS Macro Lett.* **2017**, *6* (8), 859–863. https://doi.org/10.1021/acsmacrolett.7b00484.

(130) Sasaki, T.; Shimizu, A.; Mourey, T. H.; Thurau, C. T.; Ediger, M. D. Glass Transition of Small Polystyrene Spheres in Aqueous Suspensions. *Journal of Chemical Physics* **2003**, *119* (16), 8730–8735. https://doi.org/10.1063/1.1613257.

(131) Penciu, R. S.; Fytas, G.; Economou, E. N.; Steffen, W.; Yannopoulos, S. N. Acoustic Excitations in Suspensions of Soft Colloids. *Physical Review Letters* **2000**, *85* (21), 4622–4625. https://doi.org/10.1103/PhysRevLett.85.4622.

(132) Kuok, M. H.; Lim, H. S.; Ng, S. C.; Liu, N. N.; Wang, Z. K. Brillouin Study of the Quantization of Acoustic Modes in Nanospheres. *Physical review letters* **2003**, *90*. https://doi.org/10.1103/PhysRevLett.90.255502.

(133) Pelton, M.; Sader, J. E.; Burgin, J.; Liu, M.; Guyot-Sionnest, P.; Gosztola, D. Damping of Acoustic Vibrations in Gold Nanoparticles. *Nature Nanotechnol.* **2009**, *4* (8), 492–495. https://doi.org/10.1038/nnano.2009.192.

(134) Crut, A.; Maioli, P.; Del Fatti, N.; Vall??e, F. Acoustic Vibrations of Metal Nano-Objects: Time-Domain Investigations. *Physics Reports* **2015**, *549*, 1–43. https://doi.org/10.1016/j.physrep.2014.09.004.

(135) Courty, A.; Mermet, A.; Albouy, P. A.; Duval, E.; Pileni, M. P. Vibrational Coherence of Self-Organized Silver Nanocrystals in f.c.c. Supra-Crystals. *Nature Materials* **2005**, *4* (5), 395–398. https://doi.org/10.1038/nmat1366.

(136) Ayouch, A.; Dieudonné, X.; Vaudel, G.; Piombini, H.; Vallé, K.; Gusev, V.; Belleville, P.; Ruello, P. Elasticity of an Assembly of Disordered Nanoparticles Interacting via Either Van Der Waals-Bonded or Covalent-Bonded Coating Layers. *ACS Nano* **2012**, *6* (12), 10614–10621. https://doi.org/10.1021/nn303631d.

(137) Poyser, C. L.; Czerniuk, T.; Akimov, A.; Diroll, B. T.; Gaulding, E. A.; Salasyuk, A. S.; Kent, A. J.; Yakovlev, D. R.; Bayer, M.; Murray, C. B. Coherent Acoustic Phonons in Colloidal Semiconductor Nanocrystal Superlattices. *ACS Nano* **2016**, *10* (1), 1163–1169. https://doi.org/10.1021/acsnano.5b06465.

(138) Still, T.; Sainidou, R.; Retsch, M.; Jonas, U.; Spahn, P.; Hellmann, G. P.; Fytas, G. The "Music" of Core-Shell Spheres and Hollow Capsules: Influence of the Architecture on the Mechanical Properties at the Nanoscale. *Nano Letters* **2008**, *8* (10), 3194–3199. https://doi.org/10.1021/nl801500n.

(139) Schneider, D.; Schmitt, M.; Hui, C. M.; Sainidou, R.; Rembert, P.; Matyjaszewski, K.; Bockstaller, M. R.; Fytas, G. Role of Polymer Graft Architecture on the Acoustic Eigenmode Formation in Densely Polymer-Tethered Colloidal Particles. *ACS Macro Letters* **2014**, *3* (10), 1059–1063. https://doi.org/10.1021/mz500433h.

(140) Still, T.; Mattarelli, M.; Kiefer, D.; Fytas, G.; Montagna, M. Eigenvibrations of Submicrometer Colloidal Spheres. *Journal of Physical Chemistry Letters* **2010**, *1* (16), 2440–2444. https://doi.org/10.1021/jz100774b.

(141) Montagna, M.; Dusi, R. Raman Scattering from Small Spherical Particles. *Physical Review B* **1995**, *52* (14), 10080–10089. https://doi.org/10.1103/PhysRevB.52.10080.

(142) Montagna, M. Brillouin and Raman Scattering from the Acoustic Vibrations of Spherical Particles with a Size Comparable to the Wavelength of the Light. *Physical Review B - Condensed Matter and Materials Physics* **2008**, *77* (4), 1–9. https://doi.org/10.1103/PhysRevB.77.045418.

(143) Mattarelli, M.; Montagna, M. Comment on "Selection Rules for Brillouin Light Scattering from Eigenvibrations of a Sphere" [Chem. Phys. Lett. 461 (2008) 111]. *Chemical Physics Letters* **2012**, *524*, 112–115. https://doi.org/10.1016/j.cplett.2011.12.027.

(144) Mattarelli, M.; Secchi, M.; Montagna, M. Phononic Crystals of Spherical Particles: A Tight Binding Approach. *Journal of Chemical Physics* **2013**, *139* (17). https://doi.org/10.1063/1.4828436.

(145) Mattarelli, M.; Montagna, M.; Still, T.; Schneider, D.; Fytas, G. Vibration Spectroscopy of Weakly Interacting Mesoscopic Colloids. *Soft Matter* **2012**, *8* (15), 4235–4243. https://doi.org/10.1039/C2SM07034K.

(146) Saviot, L.; Le Gallet, S.; Demoisson, F.; David, L.; Sudre, G.; Girard, A.; Margueritat, J.; Mermet, A. Inelastic Light Scattering Contribution to the Study of the Onset of Sintering of a Nanopowder. *The Journal of Physical Chemistry C* **2017**, *121* (4). https://doi.org/10.1021/acs.jpcc.6b12280.

(147) Girard, A.; Gehan, H.; Crut, A.; Mermet, A.; Saviot, L.; Margueritat, J. Mechanical Coupling in Gold Nanoparticles Supermolecules Revealed by Plasmon-Enhanced Ultralow Frequency Raman Spectroscopy. *Nano Letters* **2016**, *16* (6), 3843–3849. https://doi.org/10.1021/acs.nanolett.6b01314.

(148) Cheng, W.; Wang, J. J.; Jonas, U.; Steffen, W.; Fytas, G.; Penciu, R. S.; Economou, E. N. The Spectrum of Vibration Modes in Soft Opals. *The Journal of chemical physics* **2005**, *123* (12). https://doi.org/10.1063/1.2046607.

(149) Cheng, W.; Sainidou, R.; Burgardt, P.; Stefanou, N.; Kiyanova, A.; Efremov, M.; Fytas, G.; Nealey, P. F. Elastic Properties and Glass Transition of Supported Polymer Thin Films. *Macromolecules* **2007**, *40* (20), 7283–7290. https://doi.org/10.1021/ma071227i.

(150) Johnson, K. L.; Kendall, K.; Roberts, A. D. Surface Energy and the Contact of Elastic Solids. *Proceedings of the Royal Society A* **1971**, *324*. https://doi.org/10.1098/rspa.1971.0141.

(151) Saviot, L.; Murray, D. B. Vibrations of Weakly Coupled Nanoparticles. *Physical Review B - Condensed Matter and Materials Physics* **2010**, *81* (23), 1–7. https://doi.org/10.1103/PhysRevB.81.235432.

(152) Mark, J. E. *Physical Properties of Polymers Handbook*, Second.; Springer, 2007. https://doi.org/10.1007/978-0-387-69002-5.

(153) Mirigian, S.; Schweizer, K. S. Elastically Cooperative Activated Barrier Hopping Theory of Relaxation in Viscous Fluids. II. Thermal Liquids. *Journal of Chemical Physics* **2014**, *140*. https://doi.org/10.1063/1.4874842.

(154) Still, T.; D'Acunzi, M.; Vollmer, D.; Fytas, G. Mesospheres in Nano-Armor: Probing the Shape-Persistence of Molten Polymer Colloids. *Journal of Colloid and Interface Science* **2009**, *340* (1), 42–45. https://doi.org/10.1016/j.jcis.2009.08.022.

(155) Casalini, R.; Roland, C. M. Local and Global Dynamics in Polypropylene Glycol/Silica Composites. *Macromolecules* **2016**, *49* (10), 3919–3924. https://doi.org/10.1021/acs.macromol.6b00354.

(156) Holt, A. P.; Bocharova, V.; Cheng, S.; Kisliuk, A. M.; White, B. T.; Saito, T.; Uhrig, D.; Mahalik, J. P.; Kumar, R.; Imel, A. E.; et al. Controlling Interfacial Dynamics: Covalent Bonding versus Physical Adsorption in Polymer Nanocomposites. *ACS Nano* **2016**, *10* (7), 6843–6852. https://doi.org/10.1021/acsnano.6b02501.

(157) FernánDez-Barbero, A.; Fernández-Nieves, A.; Grillo, I.; López-Cabarcos, E. Structural Modifications in the Swelling of Inhomogeneous Microgels by Light and Neutron Scattering. *Physical Review E* **2002**, *66* (5). https://doi.org/10.1103/PhysRevE.66.051803.

(158) Stutz, H.; Illers, K.-H.; Mertes, J. A Generalized Theory for the Glass Transition Temperature of Crosslinked and Uncrosslinked Polymers. *Journal of Polymer Science Part B: Polymer Physics* **1990**, *28* (9), 1483–1498. https://doi.org/10.1002/polb.1990.090280906.

(159) Cang, Y.; Reuss, A. N.; Lee, J.; Yan, J.; Zhang, J.; Alonso-Redondo, E.; Sainidou, R.; Rembert, P.; Matyjaszewski, K.; Bockstaller, M. R.; et al. Thermomechanical Properties and Glass Dynamics of Polymer-Tethered Colloidal Particles and Films. *Macromolecules* **2017**, *50* (21), 8658–8669. https://doi.org/10.1021/acs.macromol.7b01752.

(160) Slawinski, M.; Schellekens, M. A. J.; Meuldijk, J.; Van Herk, A. M.; German, A. L. Seeded Emulsion Polymerization of Styrene: Influence of Acrylic Acid on the Particle Growth

Process. *J Appl Polym Sci* **2000**, *76*, 1186–1196. https://doi.org/10.1002/(SICI)1097-4628(20000516)76:7<1186::AID-APP22>3.0.CO;2-N.

(161) Fakhraai, Z.; Forrest, J. A. Probing Slow Dynamics in Supported Thin Polymer Films. *Phys. Rev. Lett.* **2005**, *95* (2), 025701. https://doi.org/10.1103/PhysRevLett.95.025701.

(162) Liu, Y.; Chen, Y.-C.; Hutchens, S.; Lawrence, J.; Emrick, T.; Crosby, A. J. Directly Measuring the Complete Stress–Strain Response of Ultrathin Polymer Films. *Macromolecules* **2015**, *48* (18), 6534–6540. https://doi.org/10.1021/acs.macromol.5b01473.

(163) Chonde, Y.; Krieger, I. M. Emulsion Polymerization of Styrene with Ionic Comonomer in the Presence of Methanol. *Journal of Applied Polymer Science* **1981**, *26* (6), 1819–1827. https://doi.org/10.1002/app.1981.070260607.

(164) Goodwin, J. W.; Hearn, J.; Ho, C. C.; Ottewill, R. H. Studies on the Preparation and Characterisation of Monodisperse Polystyrene Latices. *Colloid and Polymer Science* **1974**, *252* (6), 464–471. https://doi.org/10.1007/BF01554752.

(165) Ashcroft, N.; Mermin, N. *Solid State Physics*; Saunders College, 1976.

(166) Stein, A.; Schroden, R. C. Colloidal Crystal Templating of Three-Dimensionally Ordered Macroporous Solids: Materials for Photonics and Beyond. *Current Opinion in Solid State and Materials Science* **2001**, *5* (6), 553–564. https://doi.org/10.1016/S1359-0286(01)00022-5.

(167) Xu, X.; Asher, S. A. Synthesis and Utilization of Monodisperse Hollow Polymeric Particles in Photonic Crystals. *Journal of the American Chemical Society* **2004**, *126* (25), 7940–7945. https://doi.org/10.1021/ja049453k.

(168) Still, T.; Cheng, W.; Retsch, M.; Sainidou, R.; Wang, J.; Jonas, U.; Stefanou, N.; Fytas, G. Simultaneous Occurrence of Structure-Directed and Particle-Resonance- Induced Phononic Gaps in Colloidal Films. *Physical Review Letters* **2008**, *100* (19). https://doi.org/10.1103/PhysRevLett.100.194301.

(169) Cammas, S.; Suzuki, K.; Sone, C.; Sakurai, Y.; Kataoka, K.; Okano, T. Thermo-Responsive Polymer Nanoparticles with a Core-Shell Micelle Structure as Site-Specific Drug Carriers. *Journal of Controlled Release* **1997**, *48* (2), 157–164. https://doi.org/10.1016/S0168-3659(97)00040-0.

(170) Wackerlig, J.; Lieberzeit, P. A. Molecularly Imprinted Polymer Nanoparticles in Chemical Sensing – Synthesis, Characterisation and Application. *Sensors and Actuators B: Chemical* **2015**, *207*, 144–157. https://doi.org/10.1016/j.snb.2014.09.094.

(171) Canfarotta, F.; Whitcombe, M. J.; Piletsky, S. A. Polymeric Nanoparticles for Optical Sensing. *Biotechnology Advances* **2013**, *31* (8), 1585–1599. https://doi.org/10.1016/j.biotechadv.2013.08.010.

(172) Keurentjes, J. T. F.; Kemmere, M. F.; Bruinewoud, H.; Vertommen, M. A. M. E.; Rovers, S. A.; Hoogenboom, R.; Stemkens, L. F. S.; Péters, F. L. A. M. A.; Tielen, N. J. C.; van Asseldonk, D. T. A.; et al. Externally Triggered Glass Transition Switch for Localized On-Demand Drug Delivery. *Angewandte Chemie International Edition* **2009**, *48* (52), 9867–9870. https://doi.org/10.1002/anie.200904172.

(173) Bajpai, A. K.; Shukla, S. K.; Bhanu, S.; Kankane, S. Responsive Polymers in Controlled Drug Delivery. *Progress in Polymer Science* **2008**, *33* (11), 1088–1118. https://doi.org/10.1016/j.progpolymsci.2008.07.005.

(174) Zhang, J.; Sun, Z.; Yang, B. Self-Assembly of Photonic Crystals from Polymer Colloids. *Current Opinion in Colloid and Interface Science* **2009**, *14* (2), 103–114. https://doi.org/10.1016/j.cocis.2008.09.001.

(175) Voudouris, P.; Choi, J.; Gomopoulos, N.; Sainidou, R.; Dong, H.; Matyjaszewski, K.; Bockstaller, M. R.; Fytas, G. Anisotropic Elasticity of Quasi-One-Component Polymer Nanocomposites. *ACS Nano* **2011**, *5* (7), 5746–5754. https://doi.org/10.1021/nn201431w.

(176) Caruso, F.; Lichtenfeld, H.; Donath, E.; Möhwald, H. Investigation of Electrostatic Interactions in Polyelectrolyte Multilayer Films: Binding of Anionic Fluorescent Probes to Layers Assembled onto Colloids. *Macromolecules* **1999**, *32*, 2317–2328. https://doi.org/10.1021/ma980674i.

(177) Caruso, F.; Susha, A. S.; Giersig, M.; Möhwald, H. Magnetic Core–Shell Particles: Preparation of Magnetite Multilayers on Polymer Latex Microspheres. *Advanced Materials* **1999**, *11* (11), 950–953. https://doi.org/10.1002/(SICI)1521-4095(199908)11:11<950::AID-ADMA950>3.0.CO;2-T.

(178) Penciu, R. S.; Kriegs, H.; Petekidis, G.; Fytas, G.; Economou, E. N. Phonons in Colloidal Systems. *The Journal of Chemical Physics* **2003**, *118* (11), 5224–5240. https://doi.org/10.1063/1.1553763.

(179) Cheng, W.; Gorishnyy, T.; Krikorian, V.; Fytas, G.; Thomas, E. L. In-Plane Elastic Excitations in 1D Polymeric Photonic Structures. *Macromolecules* **2006**, *39* (26), 9614–9620. https://doi.org/10.1021/ma062109i.

(180) Cheng, W.; Gomopoulos, N.; Fytas, G.; Gorishnyy, T.; Walish, J.; Thomas, E. L.; Hiltner, A.; Baer, E. Phonon Dispersion and Nanomechanical Properties of Periodic 1D Multilayer Polymer Films. *Nano Lett.* **2008**, *8* (5), 1423–1428. https://doi.org/10.1021/nl080310w.

(181) Gorishnyy, T.; Ullal, C. K.; Maldovan, M.; Fytas, G.; Thomas, E. L. Hypersonic Phononic Crystals. *Physical Review Letters* **2005**, *94* (11). https://doi.org/10.1103/PhysRevLett.94.115501.

(182) Duval, E.; Boukenter, A.; Champagnon, B. Vibration Eigenmodes and Size of Microcrystallites in Glass: Observation by Very-Low-Frequency Raman Scattering. *Phys. Rev. Lett.* **1986**, *56* (19), 2052–2055. https://doi.org/10.1103/PhysRevLett.56.2052.

(183) Li, Y.; Lim, H. S.; Ng, S. C.; Wang, Z. K.; Kuok, M. H.; Vekris, E.; Kitaev, V.; Peiris, F. C.; Ozin, G. A. Micro-Brillouin Scattering from a Single Isolated Nanosphere. *Appl. Phys. Lett.* **2006**, *88* (2), 023112. https://doi.org/10.1063/1.2164924.

(184) Kang, E.; Kim, H.; Gray, L. A. G.; Christie, D.; Jonas, U.; Graczykowski, B.; Furst, E. M.; Priestley, R. D.; Fytas, G. Ultrathin Shell Layers Dramatically Influence Polymer Nanoparticle Surface Mobility. *Macromolecules* **2018**, *51* (21), 8522–8529. https://doi.org/10.1021/acs.macromol.8b01804.

(185) Guillet, Y.; Audoin, B.; Ferrié, M.; Ravaine, S. All-Optical Ultrafast Spectroscopy of a Single Nanoparticle-Substrate Contact. *Phys. Rev. B* **2012**, *86* (3), 035456. https://doi.org/10.1103/PhysRevB.86.035456.

(186) Vega-Flick, A.; Duncan, R. A.; Wallen, S. P.; Boechler, N.; Stelling, C.; Retsch, M.; Alvarado-Gil, J. J.; Nelson, K. A.; Maznev, A. A. Vibrational Dynamics of a Two-Dimensional Microgranular Crystal. *Physical Review B* **2017**, *96* (2), 1–7. https://doi.org/10.1103/PhysRevB.96.024303.

(187) Lyu, X.; Clark, B.; Peterson, A. M. Thermal Transitions in and Structures of Dried Polyelectrolytes and Polyelectrolyte Complexes. *Journal of Polymer Science, Part B: Polymer Physics* **2017**, *55* (8), 684–691. https://doi.org/10.1002/polb.24319.

(188) Imre, Á. W.; Schönhoff, M.; Cramer, C. A Conductivity Study and Calorimetric Analysis of Dried Poly(Sodium 4-Styrene Sulfonate)/Poly(Diallyldimethylammonium Chloride) Polyelectrolyte Complexes. *Journal of Chemical Physics* **2008**, *128* (13). https://doi.org/10.1063/1.2901048.

(189) Vidyasagar, A.; Sung, C.; Gamble, R.; Lutkenhaus, J. L. Thermal Transitions in Dry and Hydrated Layer-by-Layer Assemblies Exhibiting Linear and Exponential Growth. *ACS Nano* **2012**, *6* (7), 6174–6184. https://doi.org/10.1021/nn301526b.

(190) M'Bareck, C. O.; Nguyen, Q. T.; Metayer, M.; Saiter, J. M.; Garda, M. R. Poly (Acrylic Acid) and Poly (Sodium Styrenesulfonate) Compatibility by Fourier Transform Infrared and Differential Scanning Calorimetry. *Polymer* **2004**, *45* (12), 4181–4187. https://doi.org/10.1016/j.polymer.2004.03.044.

(191) Köhler, K.; Möhwald, H.; Sukhorukov, G. B. Thermal Behavior of Polyelectrolyte Multilayer Microcapsules: 2. Insight into Molecular Mechanisms for the PDADMAC/PSS System. *Journal of Physical Chemistry B* **2006**, *110* (47), 24002–24010. https://doi.org/10.1021/jp062907a.

(192) Feng, S.; Chen, Y.; Mai, B.; Wei, W.; Zheng, C.; Wu, Q.; Liang, G. D.; Gao, H. Y.; Zhu, F. M. Glass Transition of Poly(Methyl Methacrylate) Nanospheres in Aqueous Dispersion. *Physical Chemistry Chemical Physics* **2014**, *16* (30), 15941–15947. https://doi.org/10.1039/c4cp01849d.

(193) Sharp, J. S.; Forrest, J. A. Free Surfaces Cause Reductions in the Glass Transition Temperature of Thin Polystyrene Films. *Physical Review Letters* **2003**, *91* (23), 1–4. https://doi.org/10.1103/PhysRevLett.91.235701.

(194) Caruso, F.; Caruso, R. A.; Möhwald, H. Nanoengineering of Inorganic and Hybrid Hollow Spheres by Colloidal Templating. *Science* **1998**, *282* (5391), 1111–1114. https://doi.org/10.1126/science.282.5391.1111.

(195) Caruso, F. Nanoengineering of Particle Surfaces. *Advanced Materials* **2001**, *13* (1), 11–22. https://doi.org/10.1002/1521-4095(200101)13:1<11::AID-ADMA11>3.0.CO;2-N.

(196) Köhler, K.; Shchukin, D. G.; Möhwald, H.; Sukhorukov, G. B. Thermal Behavior of Polyelectrolyte Multilayer Microcapsules. 1. The Effect of Odd and Even Layer Number. *J. Phys. Chem. B* **2005**, *109* (39), 18250–18259. https://doi.org/10.1021/jp052208i.

(197) Lehaf, A. M.; Hariri, H. H.; Schlenoff, J. B. Homogeneity, Modulus, and Viscoelasticity of Polyelectrolyte Multilayers by Nanoindentation: Refining the Buildup Mechanism. *Langmuir* **2012**, *28* (15), 6348–6355. https://doi.org/10.1021/la300482x.

(198) Gao, C.; Leporatti, S.; Moya, S.; Donath, E.; Möhwald, H. Stability and Mechanical Properties of Polyelectrolyte Capsules Obtained by Stepwise Assembly of Poly(Styrenesulfonate Sodium Salt) and Poly(Diallyldimethyl Ammonium) Chloride onto Melamine Resin Particles. *Langmuir* **2001**, *17* (11), 3491–3495. https://doi.org/10.1021/la0015516.

(199) Zhang, L.; D'Acunzi, M.; Kappl, M.; Auernhammer, G. K.; Vollmer, D.; van Kats, C. M.; van Blaaderen, A. Hollow Silica Spheres: Synthesis and Mechanical Properties. *Langmuir* **2009**, *25* (5), 2711–2717. https://doi.org/10.1021/la803546r.

(200) Torres, J. M.; Stafford, C. M.; Vogt, B. D. Elastic Modulus of Amorphous Polymer Thin Films : Relationship to the Glass Transition Temperature. *ACS Nano* **2009**, *3* (9), 2677–2685.

(201) Mirigian, S.; Schweizer, K. S. Communication: Slow Relaxation, Spatial Mobility Gradients, and Vitrification in Confined Films. *Journal of Chemical Physics* **2014**, *141* (16). https://doi.org/10.1063/1.4900507.

(202) Roth, C. B.; Pound, A.; Kamp, S. W.; Murray, C. A.; Dutcher, J. R. Molecular-Weight Dependence of the Glass Transition Temperature of Freely-Standing Poly(Methyl Methacrylate) Films. *European Physical Journal E* **2006**, *20* (4), 441–448. https://doi.org/10.1140/epje/i2006-10034-0.

(203) Vogel, N.; Viguerie, L. de; Jonas, U.; Weiss, C. K.; Landfester, K. Wafer-Scale Fabrication of Ordered Binary Colloidal Monolayers with Adjustable Stoichiometries. *Advanced Functional Materials* **2011**, *21* (16), 3064–3073. https://doi.org/10.1002/adfm.201100414.

(204) Karan, S.; Jiang, Z.; Livingston, A. G. Sub-10 Nm Polyamide Nanofilms with Ultrafast Solvent Transport for Molecular Separation. *Science* **2015**, *348* (6241), 1347–1351. https://doi.org/10.1126/science.aaa5058.

(205) Jimenez-Solomon, M. F.; Song, Q.; Jelfs, K. E.; Munoz-Ibanez, M.; Livingston, A. G. Polymer Nanofilms with Enhanced Microporosity by Interfacial Polymerization. *Nature Materials* **2016**, *15* (7), 760–767. https://doi.org/10.1038/nmat4638.

(206) Moll, J. F.; Akcora, P.; Rungta, A.; Gong, S.; Colby, R. H.; Benicewicz, B. C.; Kumar, S. K. Mechanical Reinforcement in Polymer Melts Filled with Polymer Grafted Nanoparticles. *Macromolecules* **2011**, *44* (18), 7473–7477. https://doi.org/10.1021/ma201200m.

(207) Rogach, A.; Susha, A.; Caruso, F.; Sukhorukov, G.; Kornowski, A.; Kershaw, S.; Möhwald, H.; Eychmüller, A.; Weller, H. Nano- and Microengineering: 3-D Colloidal Photonic Crystals Prepared from Sub-Mm-Sized Polystyrene Latex Spheres Pre-Coated with Luminescent Polyelectrolyte/Nanocrystal Shells. *Advanced Materials* **2000**, *12* (5), 333–337. https://doi.org/10.1002/(SICI)1521-4095(200003)12:5<333::AID-ADMA333>3.0.CO;2-X.

(208) McKenna, G. B.; Simon, S. L. 50th Anniversary Perspective : Challenges in the Dynamics and Kinetics of Glass-Forming Polymers. *Macromolecules* **2017**, *50* (17), 6333–6361. https://doi.org/10.1021/acs.macromol.7b01014.

(209) Napolitano, S.; Glynos, E.; Tito, N. B. Glass Transition of Polymers in Bulk, Confined Geometries, and near Interfaces. *Reports on Progress in Physics* **2017**, *80* (3), 036602. https://doi.org/10.1088/1361-6633/aa5284.

(210) Bodiguel, H.; Fretigny, C. Reduced Viscosity in Thin Polymer Films. *Physical Review Letters* **2006**, *97* (26), 1–4. https://doi.org/10.1103/PhysRevLett.97.266105.

(211) Chowdhury, M.; Guo, Y.; Wang, Y.; Merling, W. L.; Mangalara, J. H.; Simmons, D. S.; Priestley, R. D. Spatially Distributed Rheological Properties in Confined Polymers by Noncontact Shear. *The Journal of Physical Chemistry Letters* **2017**, *8* (6), 1229–1234. https://doi.org/10.1021/acs.jpclett.7b00214.

(212) Chung, J. Y.; Nolte, A. J.; Stafford, C. M. Surface Wrinkling: A Versatile Platform for Measuring Thin-Film Properties. *Advanced Materials* **2011**, *23* (3), 349–368. https://doi.org/10.1002/adma.201001759.

(213) Zhai, M.; McKenna, G. B. Elastic Modulus and Surface Tension of a Polyurethane Rubber in Nanometer Thick Films. *Polymer* **2014**, *55* (11), 2725–2733. https://doi.org/10.1016/j.polymer.2014.04.010.

(214) Tress, M.; Erber, M.; Mapesa, E. U.; Huth, H.; Müller, J.; Serghei, A.; Schick, C.; Eichhorn, K.-J.; Voit, B.; Kremer, F. Glassy Dynamics and Glass Transition in Nanometric Thin Layers of Polystyrene. *Macromolecules* **2010**, *43* (23), 9937–9944. https://doi.org/10.1021/ma102031k.

(215) Glynos, E.; Frieberg, B.; Oh, H.; Liu, M.; Gidley, D. W.; Green, P. F. Role of Molecular Architecture on the Vitrification of Polymer Thin Films. *Phys. Rev. Lett.* **2011**, *106* (12), 128301. https://doi.org/10.1103/PhysRevLett.106.128301.

(216) Bäumchen, O.; McGraw, J. D.; Forrest, J. A.; Dalnoki-Veress, K. Reduced Glass Transition Temperatures in Thin Polymer Films: Surface Effect or Artifact? *Phys. Rev. Lett.* **2012**, *109* (5), 055701. https://doi.org/10.1103/PhysRevLett.109.055701.

(217) Lan, T.; Torkelson, J. M. Methacrylate-Based Polymer Films Useful in Lithographic Applications Exhibit Different Glass Transition Temperature-Confinement Effects at High and Low Molecular Weight. *Polymer* **2014**, *55* (5), 1249–1258. https://doi.org/10.1016/j.polymer.2014.01.031.

(218) Shamim, N.; Koh, Y. P.; Simon, S. L.; McKenna, G. B. Glass Transition Temperature of Thin Polycarbonate Films Measured by Flash Differential Scanning Calorimetry. *Journal of Polymer Science Part B: Polymer Physics* **2014**, *52* (22), 1462–1468. https://doi.org/10.1002/polb.23583.

(219) Zhang, M.; Askar, S.; Torkelson, J. M.; Brinson, L. C. Stiffness Gradients in Glassy Polymer Model Nanocomposites: Comparisons of Quantitative Characterization by Fluorescence Spectroscopy and Atomic Force Microscopy. *Macromolecules* **2017**, *50* (14), 5447–5458. https://doi.org/10.1021/acs.macromol.7b00917.

(220) Roth, C. B.; McNerny, K. L.; Jager, W. F.; Torkelson, J. M. Eliminating the Enhanced Mobility at the Free Surface of Polystyrene: Fluorescence Studies of the Glass Transition Temperature in Thin Bilayer Films of Immiscible Polymers. *Macromolecules* **2007**, *40* (7), 2568–2574. https://doi.org/10.1021/ma062864w.

(221) Roth, C. B.; Torkelson, J. M. Selectively Probing the Glass Transition Temperature in Multilayer Polymer Films: Equivalence of Block Copolymers and Multilayer Films of Different Homopolymers. *Macromolecules* **2007**, *40* (9), 3328–3336. https://doi.org/10.1021/ma070162g.

(222) Baglay, R. R.; Roth, C. B. Communication: Experimentally Determined Profile of Local Glass Transition Temperature across a Glassy-Rubbery Polymer Interface with a T g Difference of 80 K. *Journal of Chemical Physics* **2015**, *143*, 111101. https://doi.org/10.1063/1.4931403.

(223) Baglay, R. R.; Roth, C. B. Local Glass Transition Temperature Tg(z) of Polystyrene next to Different Polymers: Hard vs. Soft Confinement. *J. Chem. Phys.* **2017**, *146* (20), 203307. https://doi.org/10.1063/1.4975168.

(224) Chang, T.; Zhang, H.; Shen, X.; Hu, Z. Polymer–Polymer Interfacial Perturbation on the Glass Transition of Supported Low Molecular Weight Polystyrene Thin Films. *ACS Macro Lett.* **2019**, 435–441. https://doi.org/10.1021/acsmacrolett.9b00118.

(225) Christie, D.; Register, R. A.; Priestley, R. D. Direct Measurement of the Local Glass Transition in Self-Assembled Copolymers with Nanometer Resolution. *ACS Central Science* **2018**, *4* (4), 504–511. https://doi.org/10.1021/acscentsci.8b00043.

(226) Christie, D.; Register, R. A.; Priestley, R. D. Role of Chain Connectivity across an Interface on the Dynamics of a Nanostructured Block Copolymer. *Physical Review Letters* **2018**, *121* (24), 247801. https://doi.org/10.1103/PhysRevLett.121.247801.

(227) Tito, N. B.; Lipson, J. E. G.; Milner, S. T. Lattice Model of Mobility at Interfaces: Free Surfaces, Substrates, and Bilayers. *Soft Matter* **2013**, *9* (39), 9403. https://doi.org/10.1039/c3sm51287h.

(228) O'Connell, P. A.; McKenna, G. B. Rheological Measurements of the Thermoviscoelastic Response of Ultrathin Polymer Films. *Science* **2005**, *307* (5716), 1760–1763. https://doi.org/10.1126/science.1105658.

(229) Stafford, C. M.; Harrison, C.; Beers, K. L.; Karim, A.; Amis, E. J.; VanLandingham, M. R.; Kim, H.-C.; Volksen, W.; Miller, R. D.; Simonyi, E. E. A Buckling-Based Metrology for Measuring the Elastic Moduli of Polymeric Thin Films. *Nature Materials* **2004**, *3* (8), 545–550. https://doi.org/10.1038/nmat1175.

(230) Rowland, H. D.; King, W. P.; Pethica, J. B.; Cross, G. L. W. Molecular Confinement Accelerates Deformation of Entangled Polymers during Squeeze Flow. *Science (New York, N.Y.)* **2008**, *322* (5902), 720–724. https://doi.org/10.1126/science.1157945.

(231) Chung, J. Y.; Chastek, T. Q.; Fasolka, M. J.; Ro, H. W.; Stafford, C. M. Quantifying Residual Stress in Nanoscale Thin Polymer Films via Surface Wrinkling. *ACS Nano* **2009**, *3* (4), 844–852. https://doi.org/10.1021/nn800853y.

(232) Tweedie, C. A.; Constantinides, G.; Lehman, K. E.; Brill, D. J.; Blackman, G. S.; Van Vliet, K. J. Enhanced Stiffness of Amorphous Polymer Surfaces under Confinement of Localized Contact Loads. *Advanced Materials* **2007**, *19* (18), 2540–2546. https://doi.org/10.1002/adma.200602846.

(233) Zhang, C.; Boucher, V. M.; Cangialosi, D.; Priestley, R. D. Mobility and Glass Transition Temperature of Polymer Nanospheres. *Polymer* **2013**, *54* (1), 230–235. https://doi.org/10.1016/j.polymer.2012.11.036.

(234) Dimonie, V.; El-Aasser, M. S.; Klein, A.; Vanderhoff, J. W. Core-Shell Emulsion Copolymerization of Styrene and Acrylonitrile on Polystyrene Seed Particles. *Journal of Polymer Science: Polymer Chemistry Edition* **1984**, *22* (9), 2197–2215. https://doi.org/10.1002/pol.1984.170220921.

(235) Hergeth, W.-D.; Bittrich, H.-J.; Eichhorn, F.; Schlenker, S.; Schmutzler, K.; Steinau, U.-J. Polymerizations in the Presence of Seeds: 5. Core-Shell Structure of Two-Stage Emulsion Polymers. *Polymer* **1989**, *30* (10), 1913–1917. https://doi.org/10.1016/0032-3861(89)90366-2.

(236) Boechler, N.; Eliason, J. K.; Kumar, A.; Maznev, A. A.; Nelson, K. A.; Fang, N. Interaction of a Contact Resonance of Microspheres with Surface Acoustic Waves. *Phys. Rev. Lett.* **2013**, *111* (3), 036103. https://doi.org/10.1103/PhysRevLett.111.036103.

(237) Xu, F.; Guillet, Y.; Ravaine, S.; Audoin, B. All-Optical in-Depth Detection of the Acoustic Wave Emitted by a Single Gold Nanorod. *Phys. Rev. B* **2018**, *97* (16), 165412. https://doi.org/10.1103/PhysRevB.97.165412.

(238) Kang, E.; Graczykowski, B.; Jonas, U.; Christie, D.; Gray, L. A. G.; Cangialosi, D.; Priestley, R. D.; Fytas, G. Shell Architecture Strongly Influences the Glass Transition, Surface Mobility, and Elasticity of Polymer Core-Shell Nanoparticles. *Macromolecules* **2019**, *52* (14), 5399–5406. https://doi.org/10.1021/acs.macromol.9b00766.

(239) Torres, J. M.; Stafford, C. M.; Vogt, B. D. Manipulation of the Elastic Modulus of Polymers at the Nanoscale: Influence of UV−Ozone Cross-Linking and Plasticizer. *ACS Nano* **2010**, *4* (9), 5357–5365. https://doi.org/10.1021/nn100720z.

(240) Brune, P. F.; Blackman, G. S.; Diehl, T.; Meth, J. S.; Brill, D.; Tao, Y.; Thornton, J. Direct Measurement of Rubber Interphase Stiffness. *Macromolecules* **2016**, *49* (13), 4909–4922. https://doi.org/10.1021/acs.macromol.6b00689.

(241) Zhang, M.; Li, Y.; Kolluru, P. V.; Brinson, L. C. Determination of Mechanical Properties of Polymer Interphase Using Combined Atomic Force Microscope (AFM) Experiments

and Finite Element Simulations. *Macromolecules* **2018**, *51* (20), 8229–8240. https://doi.org/10.1021/acs.macromol.8b01427.

(242) Song, J.; Kahraman, R.; W. Collinson, D.; Xia, W.; Catherine Brinson, L.; Keten, S. Temperature Effects on the Nanoindentation Characterization of Stiffness Gradients in Confined Polymers. *Soft Matter* **2019**, *15* (3), 359–370. https://doi.org/10.1039/C8SM01539B.

(243) Wingert, M. C.; Jiang, Z.; Chen, R.; Cai, S. Strong Size-Dependent Stress Relaxation in Electrospun Polymer Nanofibers. *Journal of Applied Physics* **2017**, *121* (1), 015103. https://doi.org/10.1063/1.4973486.

(244) Richard-Lacroix, M.; Pellerin, C. Orientation and Partial Disentanglement in Individual Electrospun Fibers: Diameter Dependence and Correlation with Mechanical Properties. *Macromolecules* **2015**, *48* (13), 4511–4519. https://doi.org/10.1021/acs.macromol.5b00994.

(245) Midya, J.; Cang, Y.; Egorov, S. A.; Matyjaszewski, K.; Bockstaller, M. R.; Nikoubashman, A.; Fytas, G. Disentangling the Role of Chain Conformation on the Mechanics of Polymer Tethered Particle Materials. *Nano Lett.* **2019**, *19* (4), 2715–2722. https://doi.org/10.1021/acs.nanolett.9b00817.

(246) Milenko, K.; Pissadakis, S.; Gkantzounis, G.; Aluculesei, A.; Fytas, G. Probing Stress-Induced Optical Birefringence of Glassy Polymers by Whispering Gallery Modes Light Localization. *ACS Omega* **2017**, *2* (12), 9127–9135. https://doi.org/10.1021/acsomega.7b01409.

(247) Perez-de-Eulate, N. G.; Sferrazza, M.; Cangialosi, D.; Napolitano, S. Irreversible Adsorption Erases the Free Surface Effect on the Tg of Supported Films of Poly(4-Tert-Butylstyrene). *ACS Macro Lett.* **2017**, *6* (4), 354–358. https://doi.org/10.1021/acsmacrolett.7b00129.

(248) Burroughs, M. J.; Napolitano, S.; Cangialosi, D.; Priestley, R. D. Direct Measurement of Glass Transition Temperature in Exposed and Buried Adsorbed Polymer Nanolayers. *Macromolecules* **2016**, *49* (12), 4647–4655. https://doi.org/10.1021/acs.macromol.6b00400.

(249) Napolitano, S.; Wübbenhorst, M. The Lifetime of the Deviations from Bulk Behaviour in Polymers Confined at the Nanoscale. *Nature Communications* **2011**, *2*, 260. https://doi.org/10.1038/ncomms1259.

(250) Napolitano, S.; Capponi, S.; Vanroy, B. Glassy Dynamics of Soft Matter under 1D Confinement: How Irreversible Adsorption Affects Molecular Packing, Mobility Gradients and Orientational Polarization in Thin Films. *Eur. Phys. J. E* **2013**, *36* (6), 61. https://doi.org/10.1140/epje/i2013-13061-8.

(251) Siqueira, D. F.; Schubert, D. W.; Erb, V.; Stamm, M.; Amato, J. P. Interface Thickness of the Incompatible Polymer System PS/PnBMA as Measured by Neutron Reflectometry and Ellipsometry. *Colloid Polym Sci* **1995**, *273* (11), 1041–1048. https://doi.org/10.1007/BF00657671.

(252) Wang, J.; Mbah, C. F.; Przybilla, T.; Apeleo Zubiri, B.; Spiecker, E.; Engel, M.; Vogel, N. Magic Number Colloidal Clusters as Minimum Free Energy Structures. *Nature Communications* **2018**, *9* (1), 1–10. https://doi.org/10.1038/s41467-018-07600-4.

(253) Girard, A.; Gehan, H.; Mermet, A.; Bonnet, C.; Lermé, J.; Berthelot, A.; Cottancin, E.; Crut, A.; Margueritat, J. Acoustic Mode Hybridization in a Single Dimer of Gold Nanoparticles. *Nano Lett.* **2018**, *18* (6), 3800–3806. https://doi.org/10.1021/acs.nanolett.8b01072.

(254) Still, T. High Frequency Acoustics in Colloid-Based Meso- and Nanostructures by Spontaneous Brillouin Light Scattering. PhD Thesis, Johannes Gutenberg-Universität Mainz, 2009.

(255) İlhan, B.; Annink, C.; Nguyen, D. V.; Mugele, F.; Siretanu, I.; Duits, M. H. G. A Method for Reversible Control over Nano-Roughness of Colloidal Particles. *Colloids and Surfaces A: Physicochemical and Engineering Aspects* **2019**, *560*, 50–58. https://doi.org/10.1016/j.colsurfa.2018.09.071.

Acknowledgement

'Without any help, human beings cannot do anything.'

That's the sentence I always think. Without help, I couldn't do and finish my Ph.D. First of all, I really appreciate ████████████ and ████████████ for giving me the opportunity to start and do my Ph.D. at Max Planck Institute for Polymer Research in Germany. In 2016, when I was working at a company, I thought 2016 was the last year I could apply for Ph.D. in my life. However, around Christmas, I got the opportunity finally. With my Ph.D. study, my life changed a lot. I quitted my job. I married my lovely wife and moved to Germany. Everything was new and challenge and fun. If ██████ and ██████ didn't make a decision on me, I couldn't start my wonderous journey. Therefore, I would like to thank ██████ and ██████ first. During my Ph.D. I learn a lot of polymer physics and chemistry from them and they showed me a role model as a good educator and a researcher. In addition, I learned a great sentence 'I know that I know nothing by Socrates'. As a researcher, I will remember this and keep in mind.

I express deep thanks to ██████. Whenever I want to discuss my career and future, he always welcomes me and gave good advice. Also, he delightedly agreed as my supervisor for the department of chemistry at Uni Mainz. I gratefully acknowledge ████████████. He gladly accepted my suggestion of the examiner and helped me to finish my Ph.D. work. Thank you for his time and help.

I also express deep thanks to our group members ████████████, ██████, and ██████. During my Ph.D., ██ helped me to analyze the data that is related to the physical behavior of samples based on a physicist view. Without his help, I was not able to finish my work. When I started my Ph.D., ██ taught me a lot about how to use BLS, how to plot the BLS spectra, and how to analyze the data in detail. I think I annoyed her many times. But she always helped me without any complaints. ██████ always helped me when I had trouble with the BLS setup and German language. When I just started my German life, I didn't know German at all. Without ██████'s help, I was not able to do anything. Thank you so much, my group members.

Thank you, ████████████, ████████████, ████████████, ████████████, and ████████████ for all technical and analytical support. They were always kind to help me to measure and analyze samples. I would like to express thanks to all ██████ members. I felt a warm welcome and had good memories with them. Workshops and group seminars I could be inspired by them.

I want to express deep thanks to ████████████ and his team at Princeton University for collaboration work. He and his colleagues provided a wonderful view and advice on the glass transition. They also helped to measure the glass transition of nanoparticles by MDSC.

124

I also appreciate my friends, ████████ and ██████████. I learned a lot from them about Germany (language, culture, history, political system and so on). I love to learn Germany so that I asked many questions. They answered me delightedly all the time.

Finally, I really appreciate all the support from my wife and my family. Without my wife's support, I was not able to decide to do and complete my Ph.D. study. I am a really lucky guy. Because I met a totally wonderful woman who can always support me. While we stayed in Germany, I know it was so tough for her to study separately in Berlin. But she completed her master's program successfully and encouraged me all the time when I was in trouble. I also express deep thanks to my parents and mother in law. When I and my wife decided to quit the job (it was believed a good job position and nobody didn't understand why we quitted) and study, they supported us and our dream. Thank you.

Thank you all of you. Thank you, God.

Curriculum Vitae

Eunsoo Kang

WORK EXPERIENCE

Apr. 2017 - Present	**Max Planck Institute for Polymer Research** **- Ph.D. student** √ Polymer and inorganic nanoparticle synthesis √ Chemical and physical characterization of synthesized materials √ Brillouin light scattering spectroscopy	Mainz, Germany
Jan. 2012 - Mar. 2017	**LG Chem, Ltd.** **- Researcher, ASA(Acrylonitrile-Styrene-Acrylate) Team** √ Emulsion polymerization for ASA resin composite √ ASA production line optimization and stabilization √ Scale-up from lab to massive production of ASA products √ Product quality improvement √ Customer claim management (e.g. fisheye, surface, color, etc.)	Daejeon, South Korea
Mar.2010 - Feb. 2012	**Inha University** **- Master student, Polymer nanomaterial Lab.** √ Radical polymerization (emulsion, dispersion, suspension, solution) √ Polymer nanofiber fabrication and application for a sensor √ Dispersion stability research on carbon and inorganic materials	Incheon, South Korea
Jul. 2009 - Aug. 2009	**Daelim Industrial Ltd.** **- Intern, Chemical Plant Design Assistant** √ Understanding overall chemical plant design and operation √ Drawing and checking P&ID(Piping and Instrumentation Diagram)	Seoul, South Korea
Dec. 2008 - Jan. 2009	**Korea Institute of Ceramic Engineering & Technology (KICET)** **- Intern, Research Assistant on Polymer Composites** √ PET (polyethylene terephthalate), PA 6,6 polymerization √ Flame retardant synthesis	Seoul, South Korea

EDUCATION

Apr. 2017 - Present	**Johannes Gutenberg University Mainz** - Doctor of Philosophy (Ph.D.) Student, Chemistry	Mainz, Germany
Mar. 2010 - Feb. 2012	**Inha University** - Master of Engineering, Chemical Engineering,	Incheon, South Korea
Mar. 2003 - Feb. 2010	**Inha University** - Bachelor of Science, Chemical Engineering,	Incheon, South Korea

TECHNICAL SKILLS

•	Thermoplastic Processing:	Extrusion, Sheet & film extrusion, Injection moulding, Kneading, Hot Press
•	Morphological Analysis:	SEM, TEM, OM, and Scion image analyzer®
•	Chemical Analysis:	NMR, DOSY-NMR, FT-IR, UV-vis, EDX, XPS, GPC
•	Electrical Analysis:	Resistivity meter, Zeta potential analyzer
•	Thermal Analysis:	TGA, DSC
•	Mechanical Property Analysis:	Colorimeter(Ci7000A®, X-rite, USA), Melt indexer, HDT, VICAT, UTM, Izod impact testing machine, , Gloss meter, Haze meter
•	Thermal Conductivity Measurement:	Laser flash method, Hot wire method
•	Rheological Analysis:	Rheometer, viscometer
•	Chemical Process Simulation Program:	Aspen Plus®, PROII®, Smart Plant P&ID®
•	Weather Resistance Test Machine:	Weather-O-Meter® (Atlas, USA), q-UV 2000® (Atlas, USA)
•	Others:	DLS particle size analyzer, Dispersion stability analyzer (Turbiscan®)
•	Computer Skills	Microsoft Office, Coreldraw, Blender, Photoshop, Illustrator, SigmaPlot, Origin

LANGUAGE

•	Korean	Native
•	English	Fluent
•	German	Intermediate

PUBLICATIONS

1. **E. Kang** et al., *"Shell Architecture Strongly Influences Glass Transition, Surface Mobility and Elasticity of Polymer Core/Shell Nanoparticles"* — Macromolecules, 2019

2. **E. Kang** et al., *"Ultrathin Shell Layers Dramatically Influence Polymer Nanoparticle Surface Mobility"* — Macromolecules, 2018

3. H. Kim, Y. Cang, **E. Kang** et al., *"Direct Observation of Polymer Surface Mobility via Nanoparticle Vibrations"* — Nat. Commun., 2018

4. **E. Kang** et al., *"Electrospun BMIMPF6/nylon 6, 6 Nanofiber Chemiresistors as Organic Vapour Sensors"* — Macromol. Res., 2012

5. **E. Kang** et al., *"Aqueous Dispersion of Submicron-sized Diamond Particles for Thermally Conductive Polyurethane Coating"* — Colloids Surf A., 2012

6. M. Kim, **E. Kang** et al., *"Ionic liquid/styrene-acrylonitrile Copolymer Nanofibers as Chemiresistor for Alcohol Vapours"* — Bull. Korean. Chem. Soc., 2012

SELECTED PATENTS

1.	**E. Kang** et al., *"Thermoplastic resin composition having excellent weather resistance, method for preparing same, and molded product comprising same"*	European Patent EP3385327A1
2.	**E. Kang** et al., *"Thermoplastic graft copolymer resin, method of preparing the same, and thermoplastic resin composition including the same"*	U.S.Patent US10450453B2

** **Additional 8 patents as a co-inventor from USPTO** (United States Patent and Trademark Office) **and EPO** (European Patent Office)